HYDRATION-DEPENDENT STRUCTURING IN THE CORNEA: A MODEL FOR BOUND WATER IN COLLAGENOUS TISSUES

Eran Ittah

Department of Bioengineering – Faculty of Engineering

McGill University, Montreal

April 2023

A thesis submitted in partial fulfilment of the requirements for a Master of Engineering

Abstract

Most mechanically competent connective tissues share similarities in their constitution, form and function. Most notably, they are comprised of a dense, hydrated extracellular matrix containing collagens and proteoglycans. Both of these constitutive elements contribute to the structuring of connective tissues through macromolecular interactions mediated by interfacial forces in the aqueous medium that encompasses them. More specifically, these elements are arranged such that the swelling potential of proteoglycans is spatially confined by a relatively inextensible meshwork of collagen fibrils – leading to a system that exists in an equilibrium-like state of prestress. This prestress allows for the physiologic functioning and versatile viscoelastic properties that connective tissues exhibit. A consequence of this construction is that these elements bind large amounts of water at their interfaces, through the presentation of hydrophilic moieties, and are susceptible to physical or chemical conditions that may affect their water binding affinity. Although well-understood as the driving phenomenon in the interactions of soluble globular proteins, this principle of bound interfacial water and its effect on the physical and morphological properties of hydrated connective tissues has not been extensively investigated in extracellular matrix biology. The studies contained within this thesis employ the cornea as an exemplary connective tissue model to study the role that bound water plays in influencing the form and function of such collagenous tissues. To do so, a coarse-grained multiscale model of corneal hydration was first developed to elucidate various confinement niches containing bound water to characterise both the interactions and quantity of the bound water therein. Simultaneously, manipulation of factors influencing osmotic potential and osmolarity in corneas were employed to elucidate the relationship between bound water, hydration, and physicochemical properties of the bulk tissue. Finally, a multiscale microscopical analysis was performed to obtain a 3-dimensional contextualized overview of the corneal structure in high resolution. Ultimately, these studies have begun to elucidate some of the important morphological and physicochemical dependent properties that hydrated connective tissues exhibit and paves the way for the development of new analytical methods to quantify and characterise this bound interfacial water.

Résumé

Malgré la complexité et diversité des tissus conjonctifs dans le royaume animale, la plupart d'entre eux soutiennent des similarités en fonction de leur constitution, forme et fonction. En particulier, ils sont construits principalement d'un arrangement complexe et dans un milieu hydraté de collagènes fibreuses et de protéoglycanes - qu'on l'appelle la matrice tissulaire. Ces deux éléments constitutifs sont arrangés dans une manière précise dont laquelle la tuméfaction des protéoglycanes est resserré ou comprimé par la résistance élastique des fibres collagèneuses qui sont, partant, sous force de tension. Ce phénomène, surnommé la préstresse, ce facilite la performance mécanique physiologique des tissus conjonctifs dans un façon qui est nécessairement dépendent de leur état d'hydratation. En plus, cette dépendance est médiée par l'affinité de l'eau pour ces éléments par la présentation de groupes hydrophiles sur leurs surfaces. C'est donc cette propriété nanoscopique qui gouverne la multitude d'interactions entre les éléments constitutives de la matrice tissulaire afin de diriger les propriétés macroscopiques des tissues collagèneuses. Cette thèse se donne un aperçu des expériences conduites pour caractériser ces interactions complexes en utilisant la cornée comme une système de tissu collagèneuse simplifiée. En premier, une simulation numérique de façon 'multi-échelle' a été conçu pour décrire la localisation de différentes fractions de « l'eau lié » aux éléments ultrastructurels du tissu. En parallèle, d'autres expériences ont été conduits en manipulant l'environnement ionique ou osmotique de la cornée afin d'observer les relations entre l'hydratation, « l'eau lié », et les changements physicochimiques. Finalement, une analyse microscopique permet la visualisation de la cornée dans un façon richement contextualisé et en 3-dimensions. En tout, ces études préliminaires ont commencé la caractérisation des propriétés des tissus conjonctives en relation de leur état d'hydratation et ont dévoilé des nouveaux avenues pour la quantification et caractérisation de l'eau lié dans la contexte des assemblées macromoléculaires.

Author Contributions

I (EI) developed the topic of this dissertation and was responsible for the design, methodology, and execution of these studies under the close supervision, guidance and collaboration of my supervisor Dr. Natalie Reznikov (NR).

Other contributors include:

Dr. Marc McKee (McGill University, Montreal) who collaborated closely on this project and provided access to laboratory space and equipment to conduct electron microscopy protocols and use of the micromechanical tester.

Dr. Dirk Schumann (FIBICS incorporated, Ottawa) who I have been collaborating with over the past year and who was primarily responsible for optimising imaging and acquisition on the Zeiss Crossbeam 550 FIB-SEM.

Dan Buss (McGill University, Montreal) who worked with NR and EI to produce the final discussion figure relating to paleometabolomic niches and whose findings relating to bone ultrastructure have been instrumental for part of the discussion.

Dr. Showan Nazhat (McGIll University, Montreal - co-supervisor of EI) for productive discussions and insights over the course of this degree.

Acknowledgements

I would like to begin by thanking my supervisor, Dr. Natalie Reznikov, for the tremendous guidance, training and encouragement provided over the course of this degree. Her unwavering support and openness to new ideas has had an immensely positive impact on my approach to research and has bolstered my appreciation for the 'multiscale' view of living systems.

Thank you to the staff and scientists at the facility for Electron Microscopy Research (FEMR, McGill) who work tirelessly to ensure experiments and workflows are feasible and research objectives are met. In particular, I would like to thank Kelly Sears and Stephanie Bessette for their assistance and guidance.

I would like to thank Mychael Ittah for assisting in the design of STL files used in the finite element analyses studies as well as being a supportive brother. Additionally, I want to express my deepest appreciation to my mother and father for nurturing my creativity and scientific interests throughout my life.

Finally, I would like to thank my dearest Julia for all the patience and emotional support throughout the writing of this dissertation. Thank you for allowing me to take refuge at your apartment to continue writing this thesis during the power outages following the ice storm of April 2023.

Table of Contents

Table of Figures

List of Abbreviations

Abbreviation	*Definition*
3D	3-Dimensional
BSE	Backscatter Electron
BW	Bound Water
CT	Connective Tissue
DI	Deionized
DS	Dermatan Sulphate
DSC	Differential Scanning Calorimetry
DTG	Differential Thermogravimetry
DVLO	Derjagun-Landau-Verwey-Overbeek
ECM	Extracellular Matrix
EM	Electron Microscopy
EPON	Epoxy Resin
FEA	Finite Element Analysis
FFT	Fast Fourier Transform
FIB	Focused Ion Beam
FOV	Field of View
FW	Free Water
GAG	Glycosaminoglycan
H_2O	Water
HCO_3	Carbonate
HNMR	Proton Nuclear Magnetic Resonance Spectroscopy
IFM	Interfibrillar Matrix
IMS	Intermolecular Spacing
KS	Keratan Sulfate
LBHB	Low-Barrier Hydrogen Bonds
LCN	Lacuno-Canalicular Network
MFT	Mean-Field Theory
N_2	Molecular Nitrogen
NLVE	Non-linear Viscoelasticity
NMR	Nuclear Magnetic Resonance
NY	New York
OsO_4	Osmium Tetroxide
ORS	Object Research Systems
PBE	Poisson-Boltzmann Equation
PEG	Polyethylene Glycol
PG	Proteoglycan

QLV	Quasi-linear viscoelasticity
RH	Relative Humidity
RI	Refractive Index
SAS	Solvent Accessible Surface
SATP	Standard Ambient Temperature and Pressure
SAXS	Small Angle X-ray Scattering
SEM	Scanning Electron Microscopy
SFA	Surface Force Analysis
SHG	Single Harmonic Generation
SLRP	Small Leucine Repeat Proteoglycan
SR	Stress-Relaxation
STL	Standard Tessellation Language
TCH	Thiocarbohydrazide
TGA	Thermogravimetry
UVA	Ultraviolet-A
VIS	Visible Light

1 INTRODUCTION

Amongst the plethora of functions that connective tissues perform, their diversity in mechanical performance is by-far the most remarkable and is crucial for facilitating the structuring and support of most extant animals. Within the animal kingdom, there exists a high diversity of connective tissues that fulfill a variety of specialized functions. Consider, for example, the cornea which acts as a refractive lens to enhance visual acuity or the tendon which acts as a multiscale spring.

1.1 Hierarchical Structure

Although there exists a high degree of structural diversity amongst the many examples of connective tissues, there are certain fundamental characteristics that are almost always conserved. Most notably, all connective tissues are composed of a dense, supramolecular rich meshwork known as the extracellular matrix (ECM). Qualitatively, ECM is constitutionally similar amongst many groups of connective tissues but differs in the way it is organised in a hierarchical scale-dependent fashion. The difference becomes immediately apparent when contrasting the morphological differences between bone and cornea. Macroscopically, both tissues exhibit very distinct properties – the cornea being transparent and soft while bones are opaque and hard. However, these features begin to become blurred as the scale of observation is reduced. At the submicron level it is apparent that, save for the mineral in compact bone, both tissues contain ECM composed predominantly of type I collagen arranged in a plywood-like structure [1].

1.2 Generalizable Paradigm of Collagenous ECM Architecture

1.2.1 Collagens

Collagens are the most abundant constitutive element (by dry mass) in ECM and are the most abundant structural protein in animals – accounting for more than 30% by mass of the net proteinaceous content in most animals [2]. These proteins are, in themselves, quite diverse with at least 27 genes encoding different varieties of fibrillar and non-fibrillar forms shared amongst all chordates [2]. Generally, fibrillar collagens fulfill a predominantly structural role while non-fibrillar collagens play a minor structural role but are involved mainly in signalling and structure modulation [3]. Most collagens are composed of a repetitive Gly-Pro-Hyp peptide sequence that allows it to form a very tightly coiled triple helical super-secondary structure. Consequently, this

arrangement results in the presentation of hydrogen bonding groups at regular intervals along the surface of the tertiary structure – emanating both from the hydrogen bond donors along the peptide backbone as well as from polar side chain groups. The regularity of spacing of H-bonding groups on the surface of collagens coupled with their unique tertiary structure results in an unusually large and highly hydrated solvent accessible surface (SAS) compared to most globular proteins.

Collagen triple helices, under a broad range of conditions, exhibit the ability to self assemble into large macromolecular fibrillar structures that can span thousands of nanometres along their long axis. In cross-section, fibrils can be made up of dozens to thousands of individual tropocollagen triple helices whose assembly and aggregation can be modulated by some non-fibrillar collagens. For example, collagen type 5 is known to modulate fibrillar diameter in vivo [4]. Another important regulator of fibril diameter are proteoglycans (PGs).

1.2.2 Proteoglycans

Proteoglycans are the second most abundant structural element in the ECM [5]. PGs are composed of a protein linker which interacts directly with fibrillar collagens [6,7] and a glycosylated region containing glycosaminoglycans (GAG) – a typically non branching polysaccharide. In most non-cartilaginous ECM, the small leucine repeat proteoglycans (SLRPs) predominate whereas in articular cartilage it is usually hyaluronic acid. The GAG regions of the PGs are composed of repeating disaccharide units which can vary greatly in size depending on their location (from 1 – 10^3 kDa). During the biosynthesis pathway of PGs, a glycosylation reaction occurs extracellularly which covalently bonds the GAGs to their respective protein linkers. Sulfotransferases then chemically modify GAGs to produce sulfated moieties that allow the sugars to have both a strong anionic charge character and extensive hydrogen bonding capabilities. This feature allows for the immobilisation of water and other solutes in the ECM and is crucial for adequate osmoregulation of tissues to provide a hospitable environment for resident cells.

1.2.3 Miscellaneous non-collagenous elements

Cells and other non-collagenous (and non-PG) elements are a diverse constitutive fraction of ECM. However, on a mass basis, this fraction typically makes up between 1-10% of connective tissues depending on the type. Nonetheless, cells are crucial for the synthesis of

macromolecular building blocks that comprise the bulk of the ECM. Resident cells present an array of matrix binding proteins, such as integrins, which facilitate cell-mediated modifications to the pericellular matrix that surrounds them. Although, in many sparsely cell-populated tissues it is still unclear how much of the nanoscale morphological characteristics could be attributed to cells. Many of these non-collagenous proteins that make up the diversity of the extracellular proteome may also facilitate specialized functioning like regulation of ionic tissue homeostasis or exerting spatiotemporal control over mineralisation [8].

1.2.4 Mineralization of connective tissues

Some collagenous connective tissues such as bones and teeth mineralize – allowing for an additional structural interface to reinforce the soft tissue. Although inorganic, the predominant mineral in bone, known as hydroxyapatite, also displays a high density of hydrophilic groups on its surface enabling the retention of considerable quantities of water and organic non-collagenous proteins. This, in turn, results in a hydrated complex interpenetrating meshwork of mineral and collagen that confers toughness in bone.

1.3 Pre-Stress: A Convergently Evolved Strategy to Maximize Efficient Use of Building Materials

In most connective tissues, collagens and PGs are arranged hierarchically in such a way that facilitates a synergistic interaction between them. This enables collagenous tissues (CTs) to respond to mechanical stimuli in a resilient, tissue specific fashion that is mediated by water. In particular, in ECM, the strong water-sorptive qualities of PGs induce significant swelling sometimes retaining twenty times their dry mass in water [9]. The PGs are confined in a relatively inextensible meshwork of enzymatically crosslinked collagen fibrils that are consequently under tension. Accordingly, ECM in its normal physiological hydration state exploits this equilibrium between compression of PGs and tension of collagen fibrils to produce a tissue that is both compliant and responsive to its mechanical environment. This principle, known as prestress, manifests itself differently depending on the particular tissue being investigated. For example, the ECM in bone is decorated with SLRPs to enable water uptake and, as a result, confers a substantial increase in toughness from maximising water interfacing with its microstructure [10]. Despite having a similar constitutional profile to bone, prestress in the cornea is manifested

differently – the corneal ECM is in a constant state of deturgescence which results from careful control over its ionic environment throughout its hierarchical structure.

Although the exploitation of prestress in hydrated collagenous tissues (CTs) is variable, the 'end goal' of this phenomenon, which occurs as a consequence of hierarchical structuring is the same – it allows the organism to maximize the performance of CTs while minimizing the use of metabolically expensive synthesis pathways for collagens and proteoglycans. This is achieved by careful spatial control over water within the tissues to exploit both the dissipative qualities of water and the stiffness conferred by the turgor pressure associated with water sorption.

This principle of prestress is most pronounced within the cornea where even mild dysregulation in the way water is spatially arranged in the tissue architecture has a dramatic influence over the transparency and shape of the tissue.

1.4 Corneal Anatomy and Ultrastructure

The cornea is a uniquely transparent connective tissue and is the primary refractive element of the vertebrate camera eye. It is typically 540 – 560 μm thick in humans but can vary considerably between species [11]. Over 90% of this thickness is made of substantia propria or the stroma - a dense, sparsely cell-populated collagenous matrix. The stroma is composed of approximately 250 (1.5 – 2.5μm thick) collagenous lamellae with the fibrils being arranged in-plane to the tissue. Coaligned with these seemingly orthogonal arrays of fibrils are flattened, elongated, and transparent cell processes emanating from resident keratocytes that make up less than 10% of the stroma [12].

The transparency and biomechanical properties of the cornea are attributable to the unique ultrastructural arrangement of the tissue. Within a single stromal lamella, collagen forms densely packed fibrillar arrays with a high degree of coalignment and order [13,14]. Furthermore, between adjacent layers, the fibrillar arrangement has been posited to be nearly orthogonal [15]. The developmental and physiological processes underpinning the formation of this unique ultrastructure is currently unknown. One possibility is that the densely packed and seemingly orthogonally arranged arrays could be achieved through the exploitation of the nematic liquid crystal properties that collagen exhibits as it reaches a critical concentration in solution (> 100mg/mL) [16,17]. Other findings point towards cell-mediated processes being implicated in the arrangement of the lamellar structure [12,18] whereby filopodia of resident keratocytes exert contractile forces on fibrils thus tensioning them and promoting their densification.

When viewed edge on, the fibrils of the stroma appear to be arranged in quasi-hexagonal arrays [19], spaced apart by 50-57nm (from centre to centre), with a high degree of control exerted over their size and morphology. This unusually regular arrangement has been posited to regulate the refractive index of the bulk tissue [13,20] and minimize light scattering [21]. This highly anisotropic matrix is composed primarily of 27 nm fibrils of Type I collagen, with a small variability in diameter, which is in stark contrast to other connective tissues that exhibit a large diversity of fibril sizes [14]. Instead of further assembly into hierarchical fibre-like arrangements (characteristic of most other connective tissues), the functionalization of the fibril surface with proteoglycans (PGs), specifically SLRPs, within corneal type I collagen seems to be a major contributor to the lamellar arrangement of the stroma. Additionally, type V collagen molecules are abundant within the matrix and are likely responsible for regulating the fibrillar diameter by sterically hindering the radial addition of new molecules to the growing fibrils [4,22]. The fibrillar axial molecular stagger (D-period) of these supramolecular assemblies are atypical of what is observed in other collagenous connective tissues at 65nm and is likely the consequence of macromolecular crowding and an atypical hydration environment within the stroma. Moreover, electron tomography[23] and freeze fracture [14] studies of corneal collagen fibrils reveal that the individual tropocollagen molecules exhibit a 15 degree radial twist along the fibrillar axis. This twisting motif is also seen as a multiscale motif in other collagenous tissues like bone [24].

1.4.1 Evidence of chemiosmotic gradient in cornea

In vivo, under 'normal' physiological conditions, the cornea exists in a constant state of deturgescence or relative flaccidity where the active transport of anions from the stroma (particularly lactate, bicarbonate and Cl^-) allows for the regulation of hydration within the tissue through the action of osmotic efflux [25,26]. It is posited that modulating the level of hydration of the fibrils through this process enables a greater contiguity between the refractive index (RI) of the fibrils (which make up 40% by volume of the stroma) and the interfibrillar matrix (IFM) – the substance which surrounds them. Since, at the nanoscale, the stroma is composed of two elements which scatter light differently, by exercising careful control over the ionic environment it may be possible that this property may reduce the discrepancy between the refractive index (RI) of the two constituents making it less susceptible to optical aberrations. Other findings argue that there is in fact a significant mismatch between collagen and the IFM (1.37 vs 1.42) which should result in considerable light scattering [13]. Through this view, the absence of light scattering

is explained by the hypothesis that the corneal collagen behaves as a quasi-crystalline lattice that is adapted to only destructively interfere with incident light that is scattered laterally while allowing the bulk of the photons to pass through the tissue unhindered [27]. This constitutive model adequately explains the orientation and arrangement of the regularly offset collagenous arrays of the stroma and also explains the normal birefringence observed in the cornea [28]. As can be seen in this case, the careful control over ionic environment in the cornea allows prestress in the tissue to be tuned in such a way to favour the optical transparency of the tissue. In so doing, the tissue compromises its stiffness and mechanical robustness contributed by turgor pressure from PGs.

1.4.2 The role of the interfibrillar matrix in corneal structure and function

The interfibrillar matrix (IFM) of the cornea is primarily composed of highly hydrated proteoglycans (PGs) which are anchored to the surface of collagen and are purported to form duplexes between adjacent fibrils [29]. The IFM is composed primarily of keratan sulfate (KS) and dermatan sulfate (DS) chains that are covalently bonded to the fibril surfaces and seem to display an orderly twisted rosette arrangement around the fibril [30]. Proteoglycans are strongly osmotically active molecules which can be attributed to their highly sulfated GAG groups which are anionic at neutral pH. This strong ionic character has long been known to be a major contributor to the structure of the tissue by drawing water to maintain tissue turgor through the Donnan effect. Although most connective tissues seem to exert some regulation over this phenomenon through the precise spatial localisation of these moieties, this control is considerably more dramatic in the cornea which undergoes considerable swelling if the moieties are destabilized [31]. The lyophilic polyelectrolytic nature of PGs is in-fact critical to the normal physiological operation of the cornea in maintaining a domed hemispheroid structure while optimally refracting light.

Other conceivable modes of controlling the degree of hydration of PGs are also possible but are usually slow, irreversible chemical modifications that include enzymatic digestion or functionalization of free reducing ends. For example, water retention can be regulated in-vivo by the degree of sulphation of the polymer. This is evidently important for SLRPs which have much lower molecular weights (10^4 Da) compared with Hyaluronan (10^6 Da) [6] and thus require a higher anionic charge character to modulate the water activity in their vicinity. However, these strategies are not amenable to the responsiveness needed for maintaining osmotic homeostasis in the corneal stroma.

Many studies have described the stabilizing contribution that PGs play in the structure and transparency of the cornea [30]. In particular, they suggest that there exist GAG duplexes (held together through ionic or covalent interactions) that moderate repulsion between adjacent fibrils in the pseudohexagonal lattice of the corneal ECM by exploiting the osmotic pressure induced by the thermal motion of large interstitial GAG chains. However, there has been no successful attempt to unambiguously demonstrate that these moieties bridge interfibrillar spaces as pseudo-crosslinks. Furthermore, there has been insufficient evidence to suggest that these PGs act as a net-like lattice which stabilises the precise quasi-hexagonal arrangement of the collagen fibrils. Nonetheless, many studies refer to these bridge regions as integral elements in the constitutive models they used to describe the behaviour of the cornea at the macromolecular level [29,30] which further complicates the understanding of the role of this element in the behaviour of the cornea. Ultimately, these observations of conventionally prepared electron microscopy specimens may simply be the result of the sample preparation approach through the irreversible complexation of polyvalent phthalocyanine dyes [7].

1.4.3 Ion transport and regulation of osmolarity within the cornea

On the posterior surface of the cornea, the endothelium acts as an active ion pump carefully controlling the osmolarity and ionic strength within the cornea [32]. On the anterior surface of the cornea, the epithelium is much thicker and has tight gap junctions that help regulate the "leakiness" of the tissue. Although the precise mechanism by which the cornea engages in deturgescence is unclear, it is believed that the endothelial layer actively transports key anions (HCO_3^- and Cl^-) from the stromal space to the aqueous humour [25].

Post-mortem, these functions cease entirely within hours, resulting in a rapid swelling of the corneal stroma known as corneal edema. During corneal edema, the stomal layers delaminate from one another and swell to much larger thicknesses. At the ultrastructural level, corneal edema has not been studied but corneal dystrophies which affect the tissue structure (and possibly tissue osmolarity) have been reported to disrupt the short-range order and packing of the collagen fibrils within stromal lamellae [33].

1.4.4 Water distribution within the corneal ultrastructure

In the cornea, the highly anionic nature of proteoglycans, and the hydrophilic moieties on the surface of collagen fibrils, draw water into the tissue essentially acting as a passive osmotic

pump that can modulate turgor. The water in the tissue can be separated into at least two distinct fractions based on their physical properties [34]. These physical properties are entirely dependent on the local (sub-nanoscale) environment of a given water molecule or a clustering of them.

Firstly, water can be unhindered by its local environment - this water is considered to be free water (FW) or bulk water and does not experience short-range long-term interactions with fixed charged groups or hydrogen bonding groups and is free to perfuse through the bulk of the tissue. Alternatively, water molecules can be intimately associated with the surface of macromolecular assemblies like PGs and collagens. These macromolecular assemblies present an abundance of charged and hydrophilic moieties which allows them to interact strongly with water. The water molecules participating in this interaction exhibit drastically distinct physicochemical properties in comparison to FW. Most notably, the diffusion coefficient of bound water is always orders of magnitude lower than that of bulk water suggesting that there is only a slow exchange between the BW layer and FW molecules in the interstitial fluid of the tissue [35]. The high interfacial surface area of the stroma coupled with the presentation of an abundance of hydrophilic moieties means that bound water within the cornea may account for up to 20% of the total water mass within the tissue [36]. This is very significant considering that the cornea is ~80% water by mass [9]. As a regulator of turgor and macromolecular interactions at the submicron scale, this BW may thus play a pivotal role in modulating the structure of the cornea and is therefore sometimes referred to as structural water. Although not studied extensively within the context of animal tissues, bound water in lignocellulosic materials can be further subdivided into two categories: non-freezable bound water - which is in direct interaction with the hydrophilic structural elements of the plant tissue; and nanoconfined water which is entrapped within or between fibrillar structures [35]. We propose that a structurally homologous system could exists within the context of some hierarchically structured animal tissues as well.

1.4.5 The role of prestress in modulating corneal structure

In a basal tissue state, the confinement of structural water from the bulk tissue fluids induces an interstitial osmotic pressure thereafter resulting in a natural prestress [37]. The hierarchical organisation of collagen decorated with osmotically active proteoglycans enables the collagen fibrils to experience pretension whereas the IFM seems to exist naturally under pre-compression as it has a propensity to swell through electrostatic repulsion and Brownian motion. By existing in these conformationally preferred modes of prestress, the cornea can respond more

resiliently to mechanical stimuli by opposing and subsequently dissipating and resisting applied loads greater than 12kPa from eye rubbing, blinking, squinting, and intraocular pressure [38]. Furthermore, it is possible that this prestress is critical for maintaining optical transparency and that disruptions in this equilibrium may lead to edema.

In the cornea, mechanical loading induces the exudation and subsequent perfusion of extraneous water (from the vitreous humour) through hydrostatic forces into the interstitial space [39] — entraining with it nutrients and allowing it rebound quickly post deformation. These hydrostatic forces are also mediated by the pulling of osmotic pressure via the chemisorption of water to the surface of collagen and proteoglycans. This osmotic force, which depends on the ionic strength of a solution, is governed by the Gibbs-Donnan effect and electric double layer forces where the nanoporous ECM decorated with highly anionic residues from PGs hinder the diffusive exchange of solutes in and out of the tissue [10]. In so doing, the ECM effectively acts as a semi-permeable membrane drawing and subsequently binding water molecules (rendering it immobile structural water) leading to an increase in tissue turgor. Being retained through osmotic pressure, it has been proposed that this bound water is susceptible to variations in ionic strength and may be disrupted through the alteration of interstitial pH [40] — perhaps explaining some of the adverse mechanical performance observed in acidotic connective tissues [41].

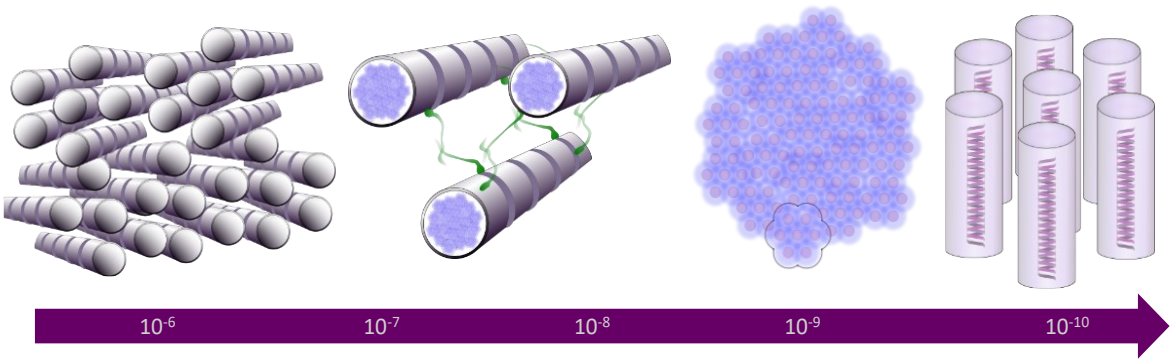

Figure 1.4-1: Multiscale representation of corneal hierarchical structure exhibiting self similarity in the arrangement of collagen fibrils and tropocollagen molecules. Scale reference at the bottom is in metres. At the lowest hierarchical level, individual tropocollagen molecules are arranged in a hexagonal lattice like packing with a spacing in between them of roughly 17Å. Hundreds of these molecular trimers are packed into a single fibrillar cross-section and are occasionally crosslinked to one another. Individual fibrils are also arranged in a pseudohexagonal lattice with a high degree of short-range order. Fibrillar surfaces are decorated with PGs that wrap around them creating a hydrated coat. Additionally, some PGs appear to form duplexes that span the entirety of the space in between adjacent fibrils.

2 PURPOSE AND OBJECTIVES

Considering that the role of hydration in the cornea seems to be inextricably linked to its function both as a protective sheath and as a refractive lens, this thesis will aim to generate a holistic view of how changes in hydration, brough about by alterations in exogenous osmotic pressure influence the corneal form and function. More broadly, this thesis will attempt to elucidate the link between interfacial bound structural water and structure in hydrated connective tissue systems by disrupting the water sorptive properties of a hydrated CT model.

To achieve this, the salmon cornea will be employed as a model tissue system to evaluate the relationship between its hydration state, its bound water content and its relevant structural properties that permit normal functioning. In so doing, this thesis will first aim to examine how water may be compartmentalized in various hydration environments in the cornea and how these

entrapped/interfacial water fractions govern scale-dependent interactions of constitutive elements. This will be done through the implementation of a multiscale biophysical model that relates hydration environment and water binding to the fundamental physical interactions between the primary building blocks of the cornea – collagen and PGs.

After establishing a robust first-principle molecular level to microscale level explanation of these interactions, this thesis will then aim to reveal how these posited multiscale hydration-dependent interactions influence physicochemical properties of the whole tissue. This may ultimately enable generalizing this understanding to other tissue systems to reveal a broader understanding of bound water mediated structuring in CTs. Ultimately, this will be achieved by utilising novel analytical methods to parse apart the contributions of free water and bound water to physicochemical properties within the cornea.

As with most connective tissues, the cornea is a complex self-similar hierarchically structured tissue (Figure 1.4-1). Accordingly, the final aim of these thesis studies will be to develop a multiscale contextualized understanding of the corneal structure and its posited bidirectional relationship to hydration. To achieve this, state-of-the-art 3D electron microscopy protocols and studies will be developed to provide a more comprehensive understanding of how fibrillar architecture and microstructure are related to hydration in the corneal stroma.

3 METHODS

3.1 Cornea Harvesting, Preparation and Storage

Fresh (unfrozen) salmon heads were obtained from a local fishmonger within hours of delivery from distributor. Whole eyes of the salmon were removed from orbit with a scalpel. The sclera was punctured to drain vitreous and aqueous humour. The cornea was excised by producing an incision along the corneoscleral junction along the perimeter of the eye. A 6mm biopsy punch was used to remove the center of the cornea, known as the corneal button which is purported to have the highest degree of ordering of collagens fibrils [15]. Finally, corneas were stored at 4°C in an osmotically balanced storage buffer (130 mM NaCl, 5% PEG in DI H_2O) to prevent swelling. Osmolarity of corneal storage solution was verified to have an osmolarity of 330 +/- 10 mOsm.

3.2 Mechanical Testing of Corneas Equilibrated at Varying Osmotic Pressure

Fresh excised 6mm corneal buttons were equilibrated for 36h at 4°C in equilibration buffering solutions containing various concentrations of PEG (1.5%, 2.5%, 5%, 7.5%, 15%, 20%) and 130mM NaCl in DI H_2O. Corneas were then placed in a MACH1 (Biomomentum, Quebec, Canada) mechanical tester retrofitted with an immersion apparatus filled with the corresponding equilibration buffer. Mechanical tester was fitted with a 1N load cell and a 4mm compression head. Cornea was placed convex side (epithelial) down in the centre of the tester and pre-compressed with a force of 1g with a strain rate of 10μm/s. At force measurement, the initial height (h_0) of the cornea was recorded. Immediately after, the cornea was subjected to a single stress relaxation test with a max deformation of $\sigma = 0.05h_0$ and a strain rate $\Delta\sigma = 0.1\sigma$ to ensure compression rate was 10 seconds in every case. Finally, a fixed relaxation time of 180 seconds was chosen as previous experimentation suggested that in most treatments, under these particular parameters, corneas are almost entirely relaxed.

After testing force (N) vs. time (seconds) data were compiled in a text file formatted by the *Biomomentum Mach1 analysis* software. An in-house script was written in MATLAB to process data from these scripts. In brief, the scripts read in the respective text files, separated and down sampled data to reduce computational demand and subsequently fitted a quasilinear viscoelastic (QLV) model to each stress relaxation curve. The QLV model was selected as it has previously shown promise in adequately accounting for the non-linear viscoelastic behaviour of highly hydrated collagenous systems [42,43]. The QLV theory models the viscoelastic response of a material based on a stress relaxation function (G) and the instantaneous stress (σ) resulting from a ramp strain (Eq 1).

$$\sigma(\epsilon, t) = \int_0^t G(t-\tau)\frac{d\sigma}{d\epsilon}\frac{d\epsilon(t)}{d\tau}dt \qquad \text{Eq 1}$$

Where σ(ε,t) is the stress relaxation response characterised by the convolutional integral of $\frac{d\sigma}{d\epsilon}$ which is the instantaneous elastic response and $\frac{d\epsilon(t)}{d\tau}$ which represents the strain history. In this equation τ represents the characteristic relaxation time of the system and t is time in seconds. In essence, the fitting procedure fits a combination of nonlinear exponential functions of the form of Eq1 but can be further simplified to the Prony expansion in Eq2 through the use of a non-

linear optimization solver. A demonstration of the goodness of fit for some sample tests are illustrated in Figure 3.2-1. Entire code can be found in 8.2.2 of Appendix B.

$$G(t) = G_\infty + \sum_i^N G_i \, e^{(-t/\tau_i)} \qquad \text{Eq 2}$$

Where G(t) is the relaxation response, G_{inf} is the force when the material has fully relaxed and G_i is the characteristic relaxation modulus parameter.

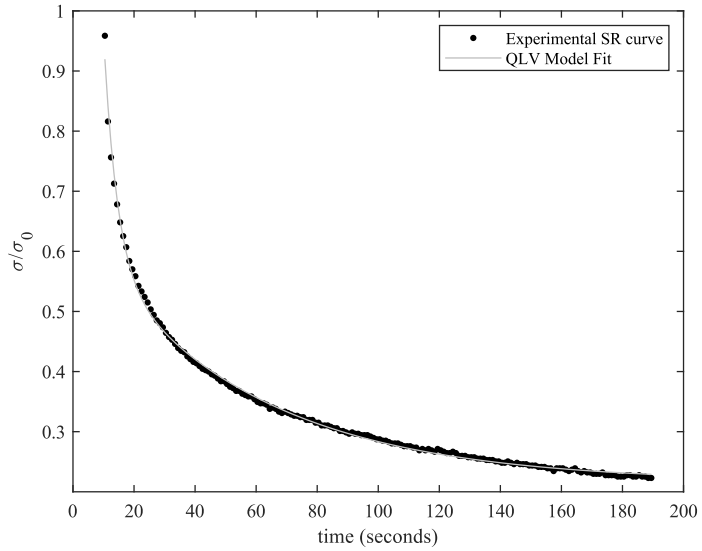

Figure 3.2-1: Example of fitted QLV models to downsampled cornea stress relaxation tests. All fits obtained a variance accounted for of > 0.98. Details of the model fitting approach and the processing of the raw data from the Mach1 software can be found in section 8.2.2 of Appendix B.

3.3 Cornea Light Scattering

Corneas were equilibrated as described in 3.1 with the addition of sodium cacodylate instead of NaCl. However, in this case, equilibration solutions were varied according to their pH and osmotic strength where two separate osmotic pressures and two separate pH values were examined (High = 10%, Low = 5%; at pH 6.4 or 7.4). Corneas were again equilibrated for 36h at 4°C. After equilibration, corneas we de-epithelized by gentle debridement and were placed epithelial side down in individual wells of a polystyrene 96-well plate and covered with 100µL of equilibration buffer. Corneas were incubated at room temperature for one hour and then subjected to a spectral scan on a Biotek™ (Winooski, VT) plate reader/spectrophotometer.

Scanning was done over entire design range (420 - 980nm). Blank subtraction was done using 180µL of respective equilibrating solution to account for volume occupancy of stroma.

3.4 Thermogravimetry

Thermogravimetric analysis (TGA) was performed using a TA instruments™ (New Castle, DE) TGA 5500. Fresh excised corneas were dehydrated in a desiccator at room temperature for two days. Corneas were analyzed using a standard 100µL platinum pan. Heating rate was kept constant at 4C/min in high resolution mode under N_2 atmosphere. The TA Trios Software automatically computes corresponding derivative and double derivative curves.

Model fitting was performed by fitting a two-parameter Arrhenius equation to the experimental data using a non-linear optimisation solver in MATLAB. The kinetics of mass loss in the system can be modelled as a system of coupled ordinary differential equations in which the desorption reaction of water occurs in multiple hydrated niches within the stroma. Where X_1 and X_2 represent the fractions of bound water contained in the intrafibrillar and extrafibrillar spaces respectively. k represents the temperature dependent reaction constant for each reaction. However, it is presumed that water does not desorb directly from the intrafibrillar space and, instead, must be first converted to extrafibrillar water before final loss. The mass balance for water within the system is thus:

$$\frac{dX}{dt} = \frac{dX_1}{dt} + \frac{dX_2}{dt} = k_1(T)[H_2O]^n + k_2(T)[H_2O]^m \qquad \text{Eq 3}$$

Where X represents the various mol fractions of water within the system. Where n and m are the orders of reactions associated with the desorption of water from the fibrils and the bulk respectively. One major assumption made is that there is no reversible redistribution of water during the desorption process.

$$k_i = A_i e^{-\frac{Ea_i}{RT}} \qquad \text{Eq 4}$$

Where activation energies (E_a) were constrained to either be lower than 100kcal/mol and an initial guess of E_a as a moderate hydrogen bond (2 kcal/mol) or larger than a strong hydrogen bond (14 kcal/mol) was provided. Ideally by constraining or providing a close estimate either one of the activation energies the other should converge to predictable values for desorption energy from IFM or desorption energy from collagen fibrils.

3.5 Multiscale Coarse-Grained Simulation of Corneal Hydration

3.5.1 Sub-fibrillar level

To model the water-mediated interactions between adjacent triple helical molecules within a fibril, a first principle model was devised according to Van Oss[44] for two parallel cylinders with hydrogen bond acceptors on their surface. In this model interfacial free energy contributions from polar forces and Van der Waals forces (VDW) were considered. The contribution of electrostatic interactions at this level were considered negligible because it has been posited that the sparse distribution of charged groups have little contribution to the fibrillar cohesion [45]. An energy balance was performed by combining these interactions to obtain interfacial free energy in mJ/m^2.

$$\Delta G_{tot} = \Delta G_{vdw} + \Delta G_{AB} = \Delta G_{vdw0}\left(\frac{l_o}{l}\right)^2 + \Delta G_{AB_o} e^{\frac{(l_o - l)}{\lambda}} \qquad \text{Eq 5}$$

Where ΔG_{tot} is the net interfacial energy of two interacting triple helices, ΔG_{vdw} is the contribution of van der waals interactions, ΔG_{AB} is the contribution of polar forces to the interfacial energy (mJ m^{-1}). Subscripts of interfacial energy contributions with a 'o' correspond to the interfacial energy at the surface. In this case, l corresponds to the distance from the molecular surface, l_o is the diameter of the fibril surface and λ is the correlation length of the solvent (typically 5.5E^{-10} m for water).

$$\Delta G_{vdw_o} = -2\sqrt{\gamma_c^{lw}} - \left(\sqrt{\gamma_w^{lw}}\right)^2 \qquad \text{Eq 6}$$

Where γ_c^{lw} = 38 mJ m^{-1} corresponds to the VDW interaction parameter of collagen with itself and γ_w^{lw} = 21.8 mJ m^{-1} corresponds to the VDW interaction parameter of water.

$$\Delta G_{AB_o} = -4\sqrt{\gamma_w^- \gamma_w^+} - \sqrt{\gamma_c^- \gamma_w^+} \qquad \text{Eq 7}$$

Where γ_w^+ and γ_w^- correspond to polar interaction parameters of water as a donor and acceptor respectively and both have values of 25.5 mJ m^{-1}. Furthermore, since collagen is assumed to have a monopolar surface in this case, the interaction parameter of collagen, γ_c^-, is negative and has a value of 27 mJ m^{-1}.

Additional expansion of these terms can be found in the simulation in section 8.2.1.1 of Appendix B.

3.5.2 Fibrillar level interactions

Collagen fibrils in the cornea are highly regular in terms of diameter and exhibit a regular periodic functionalization of polyanionic PGs on their surface. Consequently, it is assumed that the interactions that occur at the fibrillar level are predominated by electrostatic interactions – the longest-range interactions possible in aqueous solution. This assumption is further supported by calculations performed in section 3.5.1 which highlights the small distances at which polar forces and VDW forces decay rapidly. Simulation of fibrillar level electrostatic interactions were performed by first solving the Poisson Boltzmann equation (PBE) (**Error! Reference source not found.**) for a changed cylinder in a physiologically relevant solute. The PBE describes the electrostatic potential decay as a function of distance from the charged surface of a material in an aqueous medium and considers the ionic strength and charged species in the system.

$$\frac{d^2\phi}{dX^2} + \frac{X^{-1}d\phi}{dX} = \frac{eps^2}{2+a}[(1-\alpha)e^{\phi} + \alpha e^{2\phi} - e^{-\phi}]$$

$$\left(\frac{d\phi}{dX}\right)_{X=1} = -2\zeta \qquad \text{Eq 8}$$

$$\phi(\infty) = 0$$

Where the second order differential equation is subjected to the two initial value conditions listed above and is described by the two reduced parameters φ and X.

$$\phi = \frac{e\psi}{k_b T} \qquad \text{Eq 9}$$

Where e is the elementary charge, 1.602E^{-19} C. Ψ is the surface potential of the fibrillar surface in mV. K_b is the Boltzmann constant 1.38E^{-23} J K^{-1}.

$$X = 2r/R_c \qquad \text{Eq 10}$$

Where X is a reduced variable proportional to the radius of curvature R_c = 2a where a is the radius of the cylinder (30nm) and r is the radial distance from the surface.

$$\alpha = 2n_d/(2n_d + n_m) \qquad \text{Eq 11}$$

Where n_d and n_m correspond to the concentration of monovalent and divalent species within the system.

$$\zeta = \pi(\sigma/e)l_b R_c \qquad \text{Eq 12}$$

Where ζ corresponds to the linear charge density of the system and was assumed to be 2 based

on the charge density of PGs. The Bjerrum length is characterized by $l_b = e^2/4\pi\epsilon_0 D k_b T = 0.72nm$ for water and σ corresponds to the density of charged groups on the polyelectrolyte surface (C/m).

$$\lambda^2 = (4\pi l_b \Sigma_i n_i Z_i^2)^{-1} \quad \text{Eq 13}$$

Where λ is the Debye length and the summation term in the equation represents the summation of the number and valency of all ionic species in the system.

To solve the 1D PBE, an initial value problem using an RK45 numerical integration was performed coupled with a non-linear optimization protocol to simultaneously adjust the surface potential which met boundary constraints. This provided potential decay profiles depending on surface potential and ionic strength of collagen fibrils. The solver iteratively takes an initial guess for the surface potential of the structure and computes the exponential decay profile as a function of distance. After obtaining the potential decay curves it is possible to derive physisorption energy profiles through Eq 14. Where the charge density per mole can be obtained base on the degree of sulfation and concentration of PG polyelectrolytes within the ECM.

$$\epsilon = \psi\sigma_{poly} \quad \text{Eq 14}$$

Where σ_{poly} is the charge density of the polymer in C mol^{-1}. A compiled list of the various structural parameters [46–48] used in this protocol can be found in the appendix in section 8.2.1.2 , including relationships for interfibrillar spacing as a function of hydration derived from the literature.

After obtaining electrostatic potential profiles as a function of distance from a single fibril, the problem was converted to a boundary value problem with the optimized value for surface potential iteratively calculated in the previous portion. This gives a more realistic description of the electrostatic potential in between fibrils by taking into consideration the geometry of the IFM. With this information, coupled with structural and biochemical data about the proportion of GAGs on the surface of a fibril it was possible to estimate the water binding capacity as a function of distance. A detailed description of the analysis can be found in appendix under section 8.2.1.3.

3.5.3 Lamellar-level interactions

Finite element modelling was performed using the finite element analysis package in MATLAB. In brief, an STL model was generated of a simplified system of fibrils with

proportional spacing and fibrillar diameter to real system using Solidworks. The faces of the system were manually selected to assign the corresponding surface potential to the fibrils. The dielectric constant for water was used for the volume of the material. A uniform change density corresponding to 3PGs per fibril was assigned to each cylindrical facet in the model. The FEA analysis tool in MATLAB was used where there is a subpackage for solving elliptic functions like the PBE in 3D. Details about simulation approach can be found in the appendix under section 8.2.1.5.

3.6 Electron Microscopy Studies

3.6.1 Specimen preparation

3.6.1.1 Osmotically balanced specimen preparation

Fresh excised salmon corneas were placed in a solution of Alcian blue (to stabilize proteoglycans) equilibrated to standard osmotic pressure to hinder swelling of the specimen. Alcian blue solution was prepared by the addition of 0.5% Alcian blue, 100mM $mgCl_2$, 25mM Sodium acetate, 0.75% paraformaldehyde, and 5% PEG to DI-H_2O and subsequently acidified to pH 5.7. Corneas were stained in solution for 18h and then immediately subjected to osmium staining. Osmolarity was tested using a Precision Instruments 8000 freezing point depression osmometer. Other agents such as fixatives and solutes are also highly osmotically active and thus need to be accounted for during specimen preparation. Target osmolarity was 330 mOsm – this was based on data relating to interstitial tissue osmolarity in the ocular tissue of teleosts [49]. Interestingly, despite transitioning from marine to lacustrine settings, Salmonidae have remarkable osmoregulation capabilities which means their tissues are always maintained at 330 mOsm.

To make bulky specimens amenable to 3D electron microscopy, complex staining protocols may be needed to enhance both the electron density and conductivity of the bulk the specimens. A promising approach to conductive staining is known as OTOTO method. In this approach, sequential rounds of immersion in osmium and subsequently in thiocarbohydrazide are performed. This technique, which has been used on an array of specimen types [1], allows for the accumulation of osmium precipitates in the tissue nanostructure – greatly enhancing electron contrast. Osmium staining was performed by immersing rinsed specimen in 1% OsO_4 solution for 30 minutes. The corneas were then rinsed thoroughly in order to remove any residual OsO_4. Corneas were then immersed in a 0.5% solution of thiocarbohydrazide (TCH) for an additional

15 minutes. Thes rounds of OsO_4 and TCH staining were repeated, for 15minute intervals each, an additional two times to obtain the following sequence: OTOTO. After entire procedure was complete, specimens were again rinsed in DI H_2O and subsequently processed for dehydration using a laboratory microwave (PELCO).

3.6.1.2 Microwave Assisted Protocol

Specimens were dehydrated using a concentration gradient of acetone (30%, 50%, 70%, 90%, 2x100%). During each step, specimens were processed in microwave for 2-minutes at 150 watts under 20mmHg vacuum.

After dehydration, a microwave embedding protocol was also performed employing a gradient of concentrations between acetone and EPON812 resin. The specimens were processed in microwave at 2x- 1:1, 1:2, 1:4, 2x-100% EPON at 150 watts, under 20mmHg vacuum.

Specimens were then placed in silicone molds and polymerized by heating at 250W for 30 minutes and then left to rest for 5 minutes, then subjected to polymerization at 400W for 45 minutes ensuring temperature of resin does not exceed 55C.

3.6.2 FIB-SEM studies

Processed blocks were trimmed to reveal regions of interest using a block trimmer, mounted on a standard 10mm SEM stub and sputter coated with 5nm of platinum. Specimens were visualized for SEM and slice and view using a Zeiss Crossbeam 550 focused ion beam scanning electron microscope (FIB-SEM, Carl Zeiss, Oberkochen, Germany). Imaging was typically performed at 1.5kV with a dwell time of 5µs a probe current of 68.1 pA. The imaging conditions were such that the final pixel size of acquired images were 5nm. Considering the low noise and high contrast, this small size allowed for visualization of individual fibrils.

3.7 Image Processing and Analysis

3.7.1 Segmentation approach

To segment fibrillar ultrastructure from FIB-SEM image stacks, images were processed using the ORS Dragonfly software. Images were first smoothed with a gaussian filter and contrast enhanced. Images were destriped to remove artefacts caused by image shifting during autofocus correction in microscope. Subvolume of image stack was resliced to obtain in-plane view of fibrils (Z direction directly corresponded to an increase in stromal depth). Simple

thresholding segmentation was performed to better visualize fibrillar architecture. This was possible because of strong contrast between fibrils and IFM.

3.7.2 Directionality mapping script

Directionality was performed using an in-house MATLAB script (8.2.4). In brief, this script selects a region of interest in volume to create a 400x400 pixel subvolume. A fast Fourier transform (FFT) is taken for each slice and is subsequently azimuthally integrated to obtain a value for the average directionality of the fibrils as a function of stromal depth.

4 RESULTS

4.1 Coarse-Grained Multiscale Simulations and Hydration Packaging

As previously mentioned, the cornea is a hierarchically arranged tissue with scale dependent structural and morphological differences [50]. Therefore, any comprehensive attempt to model the hydration-dependent structural changes in the tissue should be done by accounting for these diverse hierarchical levels. Accordingly, for the coarse-grained simulations outlined here, modelling of water-mediated interactions was performed on three major hierarchical scales in the cornea that span intermolecular interactions until microscale interfacial surface phenomena.

4.1.1 Subfibrillar-level hydration dynamics

The smallest possible scale of interactions within the cornea occur between adjacent tropocollagen triple helices within a fibrillar core [21,51]. At this level of interaction, from a few angstroms to a few nanometres, weak force interactions predominate mainly in the form of polar forces, Van der Waals and Brownian motion (Figure 4.1-1) [44,52]. Although, in many tertiary structures of globular proteins "hydrophobic interactions", driven by water [53,54] are typical, the highly polar and exposed 3_{10} helix of the polypeptide of fibrillar collagens, including type 1 collagen, seems to counterintuitively exhibit little in terms of hydrophobically driven cohesion [55]. At this level it is believed that the intrafibrillar water is strongly confined and poorly labile between a hexagonal array of trimeric helices and that it is only susceptible to disruption under extreme conditions. For example, extreme changes in ionic strength [31], intense osmotic pressure [56] or desiccation [57]. Despite this, extreme values in pH seem to exhibit little effect on the intermolecular spacing as a function of hydration [31].

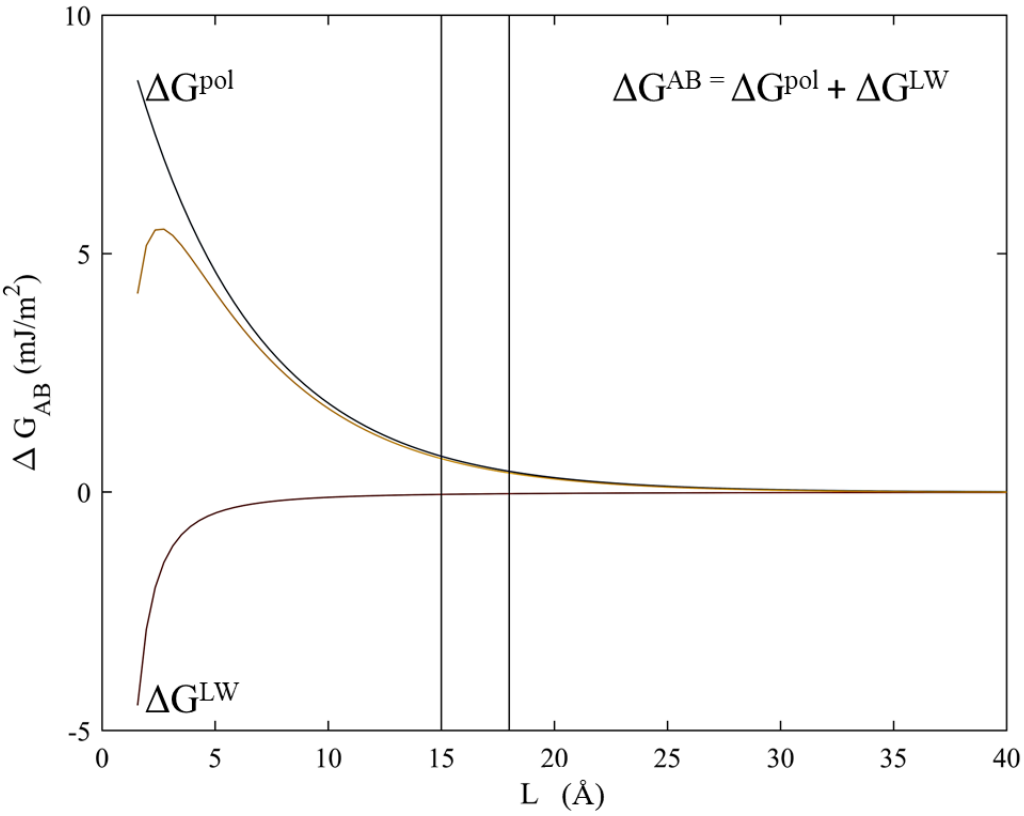

Figure 4.1-1 : Triple-helical level free energies of interaction (ΔG) between two adjacent collagen triple helices in an aqueous medium as a function of distance from surface This simulation utilizes the theory of combined hydrated interfacial phenomena [44]. Furthermore, this model accounts for rudimentary protein geometry by considering triple helices as rigid cylinders and predicts very short-range interactions between them. However, this model does not consider the expansion of the triple helices as a function of hydration, a phenomenon which has been observed experimentally [58]. Horizontal bars indicate range of experimental intermolecular distances that collagen triple helices exhibit at physiological hydration (0.15-0.175nm). Threshold for significance of intermolecular repulsion lies at roughly 5% of the initial value.

Experimental studies utilizing functionalized collagen triple helices in surface force apparatuses (SFA) observed similar interactions that were not dependent on the ionic environment but heavily dependent on osmotic pressure [45] (indicating a predomination of long-distance polar repulsive forces) and observe a similar 'equilibrium' interaxial distance of ~17Å. Moreover, this first principle model outlined here appears to be consistent with the mean-field theory (MFT) for hydration interactions [59].

This updated model accounts for energy changes relating to hydrophobic forces and London forces. From this molecular level simulation, it can be seen that the interaction energy is

evidently distance dependent from the surface of the protein. Although this simplified model greatly reduces the surface complexity yielded by modelling the tropocollagen molecular trimer as a cylinder, it nevertheless assumes a constant uniform distribution of hydrogen bonding moieties on the surface of the trimer which is, in fact, quite consistent with the repetitive nature of the tropocollagen tertiary structure. Furthermore, this simulation at this level does not consider the possible electrostatic interactions caused by occasional charged residue side chains in the collagen sequence (typically histidine) although some previous evidence suggests that borohydride reduction of the charged imidazole side chain on the His residue has little effect on the sub-nanometre scale water mediated interactions between adjacent molecular trimers [45].

Ultimately, from the intimacy of interaction between adjacent trimers, it is assumed that effectively all intrafibrillar water is considered bound or confined to some degree. Considering that the surface to surface spacing of fibrils only permits enough room for what is effectively a monolayer coverage of water (according to our simulations as well as others experiments [58]) it is possible simply through geometrical information about the collagen solvent accessible surface to obtain a preliminary estimate of the net bound intrafibrillar content (see 8.2.1.1 for detailed calculation). Ultimately this bound water content is estimated to account for roughly 10% of the water content of the cornea. Although mechanical deformation and dehydration have been demonstrated to influence the fibril morphology [60] and, by extension, its water binding capacity, this does not imply that water is not tightly bound. Contrarily, considering that tropocollagen trimers have an elastic modulus of 3 - 16GPa under tension [61–63], these changes in conformation and hydration are the consequence of comparatively large stresses at the molecular level. Finally, a posited change in hydration structure surrounding individual collagen molecules does not directly equate to a loss of bound water as this phenomenon may be coupled with the redistribution of water between the intrafibrillar space and fibril surface.

4.1.2 Fibril-level hydration

In the cornea, individual fibrils are arranged in a highly ordered pseudocrystalline hexagonal lattice with well defined spacing of 54nm in between them [19,64]. The fibrils are functionalized at regular intervals with SLRPs that exhibit a highly anionic charge character. Simplifying the fibrillar morphology by modelling the fibril as a cylinder with a uniform charge density emanating from the PGs on the fibril surface, it is possible to simulate the electrostatic interactions and water sorption capabilities of collagen fibrils (Figure 4.1-2).

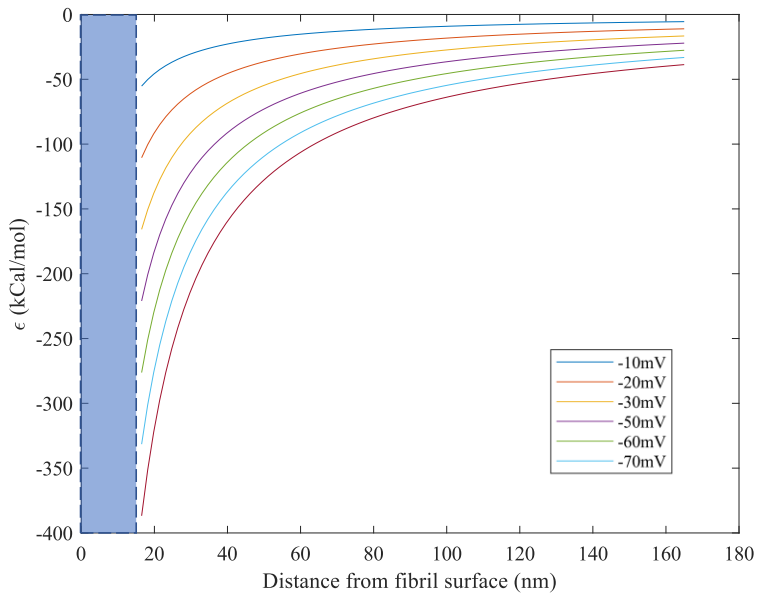

Figure 4.1-2: Simulated representation of sorption energy (kCal/mol) derived from electrostatic potential as a function of distance of an isolated dilute suspension of collagen fibrils with uniform surface charges emanating from GAGs. Calculated through the numerical integration of the PBE (Eq 8) as an initial value problem where the initial surface potential was varied to observe decay characteristics of potential. Range of surface potentials correspond to differences in the degree of sulfation of specimen. Blue bar indicates fibrillar surface.

In this case, a very large hydration coat exceeding dozens of nm is typically apparent in physiological salt solution. The influence of salts, other ionic species and other osmotically active substances will all have the effect of lowering the amount of hydrated water surrounding the fibrils by electrostatically shielding the potential on the surface of the fibril. This phenomenon known as Manning condensation [65] implies that a large coat of hydrated cationic centers likely surrounds most PGs in the cornea. This predicted cationic condensation on the surface of GAGs may be a mechanistic explanation for GAG duplexing discussed previously.

Although Figure 4.1-2 provides insight about the electrostatic surface potential and, by extension, the hydrodynamic radius of an individual collagen fibril in a dilute suspension, it is not generalizable to tissue systems with complex geometries and hierarchical morphological features. If each individual fibril had a 30nm hydration shell on its surface, at physiological hydration, the near entirety of water stored in the cornea would exist in a highly bound state - a state in which water prefers to interact with that interface rather than with itself. In a sense, the hierarchical arrangement in the cornea is of the simplest form of self-similarity found in

connective tissues – a hexagonal lattice of molecular trimers arranged into supramolecular aggregates of uniform diameter also existing as a pseudohexagonal array with a very high degree of fibrillar co-orientation. Accordingly, to adequately model the interfibrillar interactions occurring in the corneal ECM, the simulation simply needs to model the sorption affinity for water of two adjacent uniformly charged cylinders (Figure 4.1-3).

This simulation, which considers realistic geometrical constraints of the corneal ultrastructure, suggests that the electrostatic repulsion from the fibrillar surface has a strong influence over the water binding capacity of the system. Instead of drawing water radially in large shells dozens of nanometres thick (as seen in isolated fibril case), the confinement of GAGs within a small space drastically increases the endogenous osmotic pressure of the matrix surrounding the fibrils by minimizing the conformational entropy of the polymers thus significantly reducing their respective water binding capacity. Therefore, it appears that there is a PG concentration-dependent water sorption relationship with charged polymers where, after a certain level of confinement, the endogenous osmotic pressure of the polymer and interpolymer repulsive forces diminish water binding capacity of the entire macromolecular assembly of the fibril. This can be further exemplified by visualizing the water sorption dependency on interfibrillar distance of two adjacent fibrils (Figure 4.1-4) since experimentally there is a well-defined relationship between hydration and interfibrillar distance [31,48].

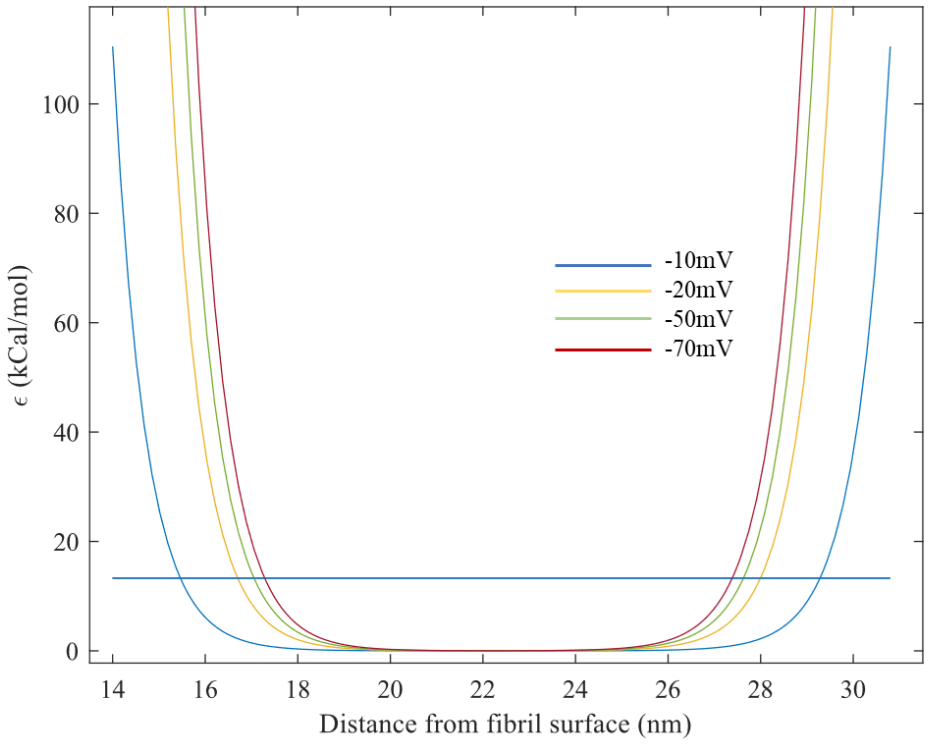

Figure 4.1-3: Dependency of the equilibrium interfibrillar distance on surface potential of fibrils.

PBE calculated energies from the surfaces of adjacent collagen fibrils. Line from left to right correspond to -10mV, -20mV, -50mV and -70mV respectively. Horizontal line indicates binding energy threshold for tightly bound water (13.3 kCal/mol). Blue bars on ends indicate boundaries of two fibrillar surfaces with a normal physiological interfibrillar spacing of 18nm (surface to surface).

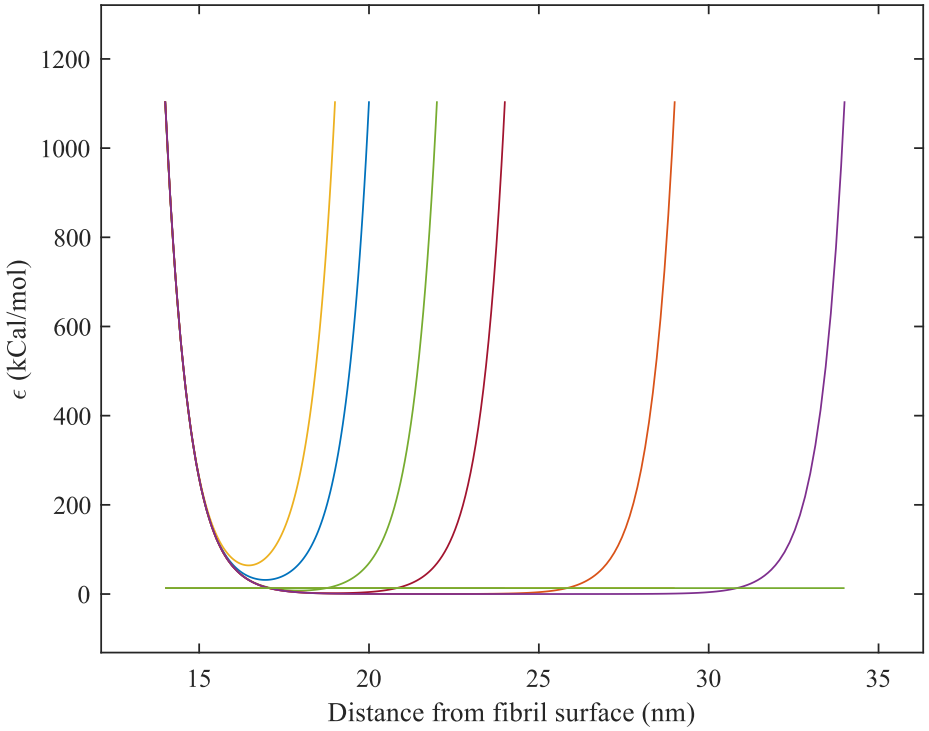

Figure 4.1-4: Comparison of varying interfibrillar distances on the hydration shell thickness surrounding fibrils. There seems to be only a nominal change in shell thickness, suggesting a nominal relationship between osmotic pressure and hydration.

When visualising water sorption in the context of the tissue nanostructure rather than just an isolated protein in solution, the interactions with surrounding solvent are much more intimate. From these calculations, there seems to be a 3-4 nm coat of water on the surface of the fibrils that is considered tightly bound water. This calculation was performed by assuming that the energy threshold for a strong H-bond needs to be at least 13.3kCal/mol - the binding energy for water to preferentially interact with the ligand or ion rather than interacting with itself [66]. For context, the latent heat of vaporisation of water (at 1atm) is only 9.7kCal/mol suggesting only very strong interactions. Knowing the geometry and relative volume fractions of the different constitutive elements that make up the corneal ECM, it is possible to calculate the thickness of the hydration shell surrounding the fibrils as a function of stromal hydration (Figure 4.1-5).

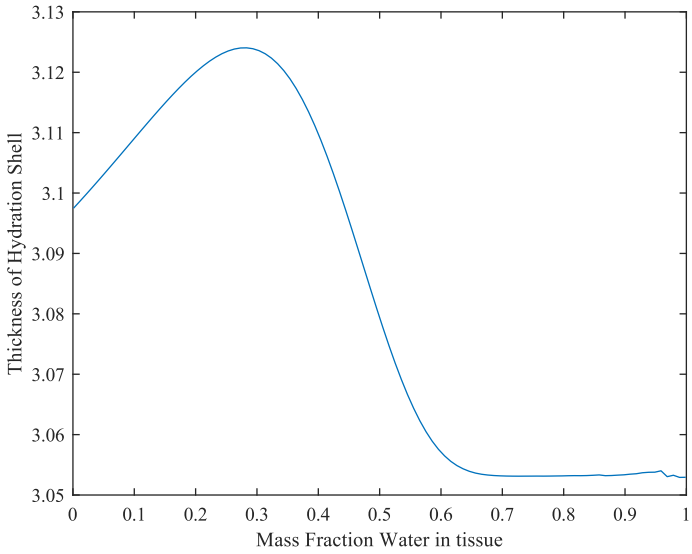

Figure 4.1-5: Reported Thickness of hydration shell as a function of corneal ECM hydration. See simulations 8.2.1.4 in appendix for details on the computational approach. In short, after obtaining thickness of physisorbed water shell to the surface of the fibril for each hydration condition. This value in combination with the interfibrillar spacing was used to calculate an approximate volume occupancy of the physiosorbed water. Assuming that this water fraction bears approximately the same density as bulk water, it is thus possible to calculate the mass fraction that the bound water occupies.

The hydration shell thickness variation as a function of bulk hydration suggests that there is a small difference in radial shell thickness along the possible hydrated range of the cornea. In particular, a change in hydration shell thickness between 3.125 and 3.054 nm corresponds to the loss of roughly one-half a molecular layer of H_2O in a shell roughly 10 molecular waters wide. However, this view of the slight variation in hydration does not consider the bulk hydration state of the tissue nor does it provide actual quantitative metrics for how much this water represents as a function of total mass in the system. By accounting for the volume fraction of the fibrils and IFM respectively (based on experimental measurements) and by considering changes in fibril diameter as a function of hydration, it is possible to calculate the relationship between bulk hydration and the fraction of that water (compared to total mass of tissue) that is in these tightly bound hydration shells (Figure 4.1-6).

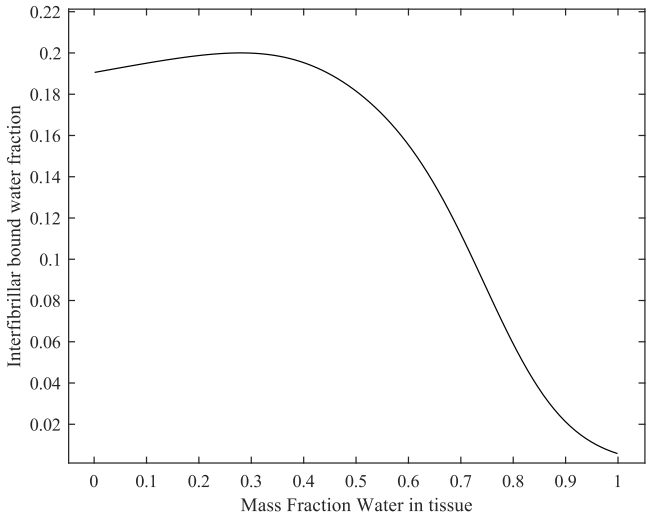

Figure 4.1-6: Fraction of bound water coating collagen fibrils as a function of bulk hydration. There appears to be a strong affinity for this water at the surface of these fibrils which are highly resistant to removal even at comparatively high osmotic pressures. Script in 8.2.1.4 outlines details of calculation.

At normal physiological hydration (80%) this coat accounts for roughly 8% by hydrated mass of the tissue and that, predictably, this mass is preferentially retained during dehydration considerably. The implications of this are that, despite there not being a substantial change in the thickness of the hydration shell surrounding the fibril, the large interfacial area, coupled with the strong electrostatic forces, strongly bind a roughly 3nm thick layer onto the surface of the fibril that can account for 8% of the bulk mass of the cornea at physiological hydration. Furthermore, this implies that, although there is a rigidly structured hydration shell that persists around the fibril, at physiological hydration, there is at least an additional 14nm of unstructured water in between them that remains open to the passive, albeit still hindered from possible bridging PGs, transport of nutrients. Interestingly this rigid 3nm shell predicted purely from first principle electrostatics has been observed experimentally and was estimated at roughly 4nm wide [57].

4.1.3 Lamellar hydration dependence and organisation

Within the corneal stroma, collagen fibrillar arrays are arranged into lamellar sheets in which their orientation is pitched by a consistent offset. The precise orientation of this offset is still up to debate and will be discussed further in another section of this thesis. However, the interlamellar boundary is another microscale hierarchical niche that can potentially bind water.

Accordingly, a finite element analysis (FEA) simulation was developed using the complex geometry of two perpendicular lamellae to explore the potential lability of water in the interlamellar boundary (Figure 4.1-7).

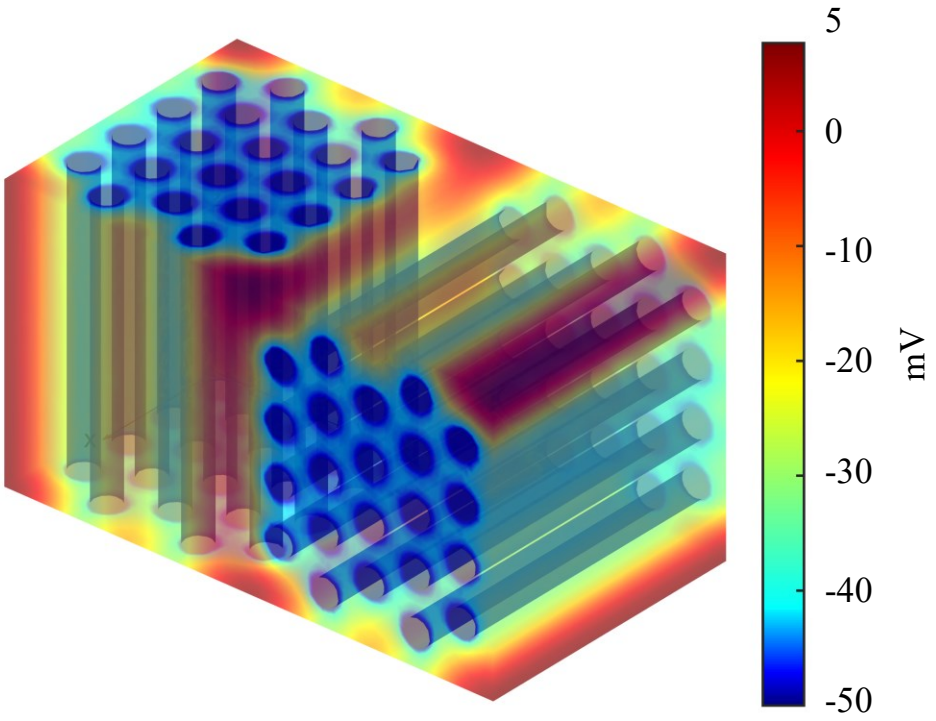

Figure 4.1-7: Potential maps of inter-lamellar boundary in the cornea demonstrating that this hierarchical niche facilitates nutrient traffic along interlamellar regions which may span the entire lateral distance of the stroma.

Ultimately, as predicted from the fibril level simulations, the electrostatic potential emanating from GAGs on the fibrillar surface appear not to pervade into the interlamellar space suggesting that this hierarchical niche does not contain a significant quantity of bound interfacial water.

4.1.4 Fractionation of various hydration niches in cornea

Ultimately, these simulations provide a preliminary biophysical basis to explain water mediated interactions by parsing apart various scale niches within the cornea. In so doing, these simulations allow for the estimation of water sorption affinity to the constitutive elements of the cornea and their implications on morphological features. These simulations also facilitate the

estimation of the respective fractions of posited BW (Table 4.1-1) in the cornea allowing the possibility to target and implicate these BW niches in whole tissue scale properties. Although insightful, to date the validation of this multi-niche hydration model for connective tissues has not been explored experimentally.

Table 4.1-1: Quantitative estimates for bound water fractions in various hydration niches in the cornea

Hydration Niche	Mass Fraction (80wt% water)	Type
Intrafibrillar	10.7%	Bound
IFM	8.2%	Bound
Cellular	5-10 %	Free
Bulk	70-75%	Free

4.2 Cornea Physicochemical Properties

Although the coarse-grained simulations explored in 4.1 provide insight into the water sorption affinity of the corneal ECM, it would be ideal to validate this prediction experimentally and, arguably more importantly, understand how these nuanced changes to hydration state affect the bulk physical properties of the tissue. In so doing it may be possible to develop a holistic understanding of how disrupting normal hydration within the cornea influences its form and function.

4.2.1 Thermogravimetric analysis sheds light on multi-compartment water sorption niches in cornea

Since, in section 4.1 it was possible to obtain estimates of the total bound water fraction within the corneal stroma at physiological hydration, an attempt to validate this prediction experimentally should be made. Previous studies which have attempted to elucidate the bound water content within the cornea have employed either Nuclear Magnetic Resonance Spectroscopy (NMR) [34,36] and/or differential scanning calorimetry (DSC) [36]. Although these methods are highly specific, they provided greatly confounding estimates of the total bound water content within the corneal ECM. The nuance lies in the definition of what is considered "bound water". In the case of NMR, bound water is defined based on the field strength and polarization of H-bonds between water and non-water moieties but may have difficulties resolving differences in these strengths or resolving nanoconfined water. Conversely, in DSC, measurement of the freezing point depression of water is made which typically can distinguish between confined and free fractions of water but does not provide much derivable information besides changes to this colligative property. Accordingly, although these two arbitrary physical characteristics are interrelated, these techniques inherently define structural water differently. Another relatively simple technique which has had success in characterising the bound water fractions of various hydrophilic polymers is thermogravimetry [35,67]. In this technique, a sample is heated incrementally at a constant rate and the corresponding weigh of the sample is continually measured. This, when optimized properly, could enable the distinction between different hierarchical water sorption niches which should preferentially desorb water at a different rate.

Accordingly, a preliminary TGA analysis was conducted to attempt to resolve differences in these niches.

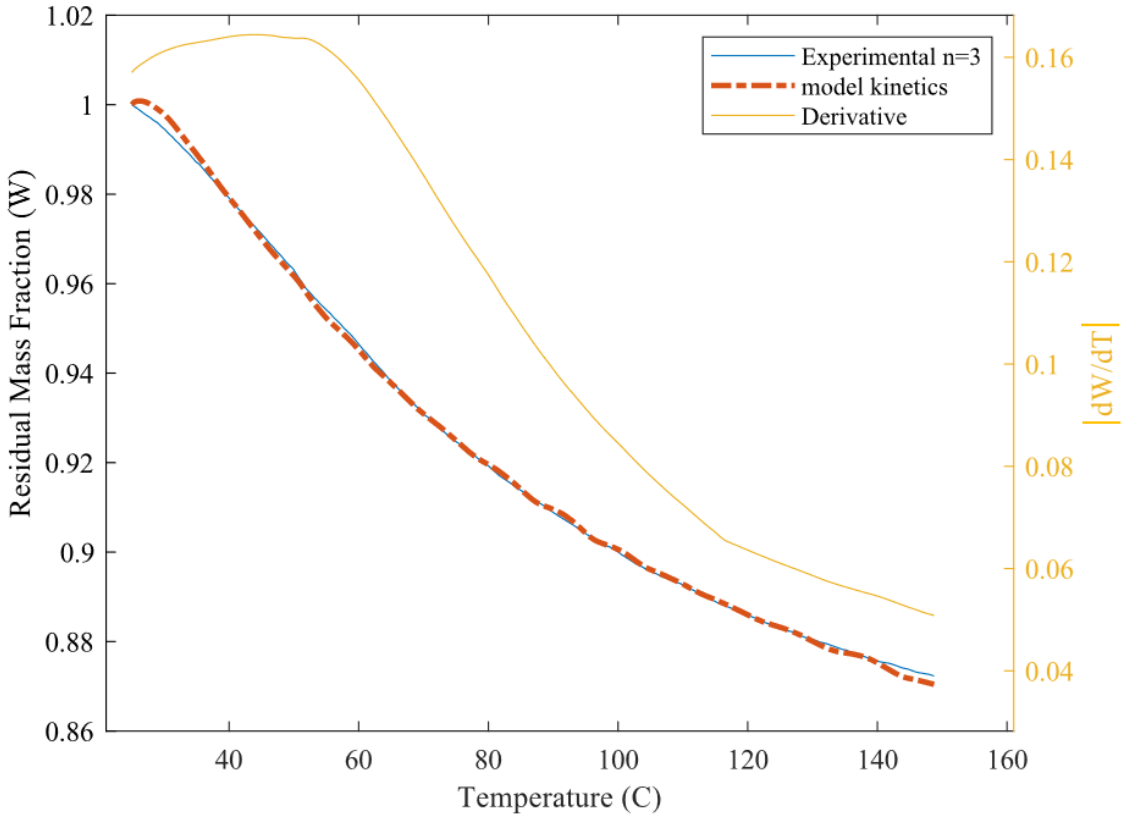

Figure 4.2-1: High resolution TGA analysis of bound water fractions in the corneal stroma of the salmon. Model fitting sorption kinetics to TGA curves suggests that there is a two-step process of water removal from the cornea. Single reaction rate models for how water is removed from cornea do not adequately explain variance in the model. Activation energies of model (See section 3.4) were found to be Ea1 = 17.65kCal mol-1 and Ea2 = 2.47kCal mol-1.

To perform these experiments, fresh corneas were excised from animal and de-epithelized through gentle debridement. Corneas were placed in desiccator for two days to air dry completely at RH $\leq$ 40%. Finally, Corneas were placed in a high-resolution TGA (TA TGA5500) and analyzed. Initially, corneas were kept fully hydrated for preliminary experiments but the large mass fraction of free water being released during measurements interfered with instrument sensitivity for resolving small bound water fraction this way. Preliminary findings suggest that even after desiccation of corneas at SATP and RH < 40%, there still remained at least 14 percent by mass water in the system (Figure 4.2-1). In fact, this value is likely higher,

and the premature stopping of the protocol can be seen by the steepness of the curve at the endpoint. Future experimentation will continue until 200°C. In any case, the inflection point in the DTG curve indicates that water desorption at around 116°C changes rates suggesting that there exist at least two resolvable bound water fractions in the cornea.

Additionally, analysis and deconvolution of second derivative curve suggests that there are at least two bound water fractions that exist in the dry cornea (Figure 4.2-2). These tightly bound fractions account for at least 13% of the total mass of the dry cornea which is roughly 3% of the fully hydrated cornea. This further attests to the variability in the definition of what constitutes bound and free water. Interestingly, this estimate is in closer agreement with estimates obtained for NMR experiments [34].

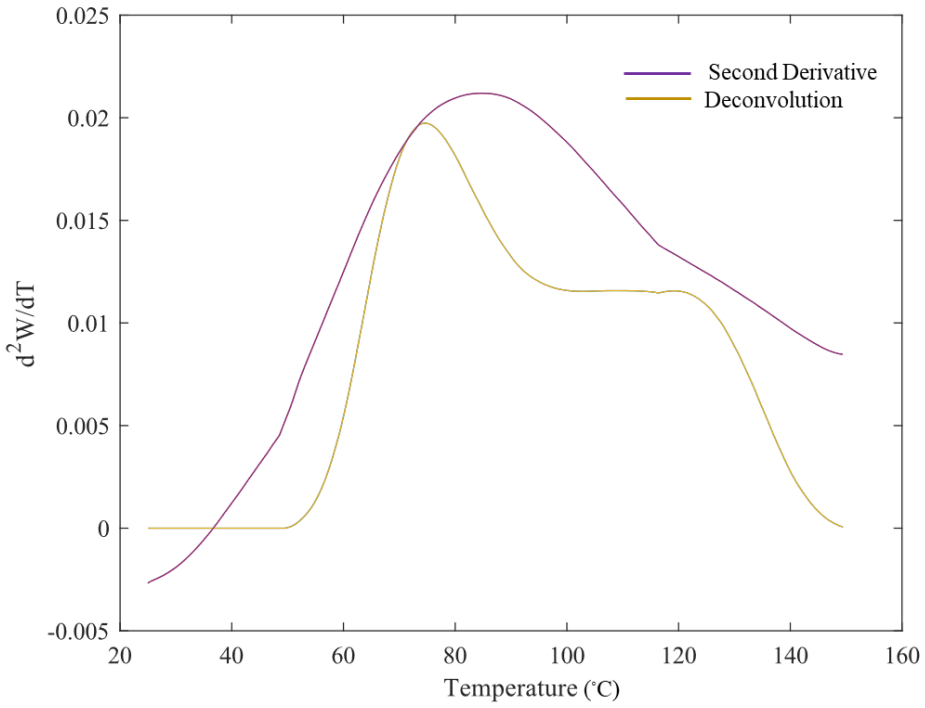

Figure 4.2-2: Blind deconvolution of second derivative of TGA curve indicating the probability of two distinct water confinement niches within the corneal extracellular matrix.

4.2.2 Corneal optical properties in relation to pH and osmolarity

The cornea serves a dual function as a protective layer for the vertebrate camera eye as well as being a strongly refractive lens. Inevitably, the unique hydration dependency on the corneal ultrastructural morphology also has larger ramifications for its function as an optical

lens. Accordingly preliminary experimentation was conducted to investigate the changes in transparency of the cornea as a function of osmotic pressure and pH. The pH range investigated was specifically chosen as it is the physiologically relevant pH range seen in vivo [68] for corneal acidosis. In these experiments, a spectrophotometer was employed to perform spectral scans on the corneas to reveal how they were affected by pH and osmotic strength (Figure 4.2-3). The full capable range of the spectrophotometer was scanned through to elucidate if there is preferential scattering of the light at different energies. Two osmolarity treatment combined with two distinct pH levels were ultimately employed for this experiment.

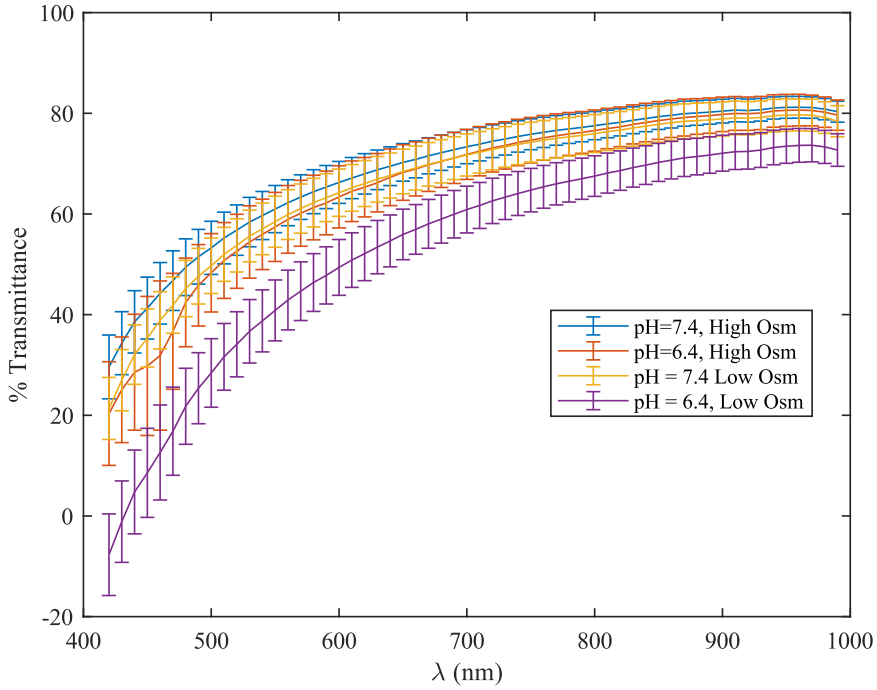

Figure 4.2-3: Influence of osmotic strength and pH on the transparency of the cornea. 5% and 10% PEG correspond to Low Osmolarity (330 mOsm) and High Osmolarity (610 mOsm) respectively as verified by a freezing point osmometer. 'High' and 'Low' osmolarities correspond to hyperosmolar and physiological osmolarity of the tear film respectively. n=8 , error bars are standard deviation.

The treatments seemed to yield the same transmittance behaviour except for the low pH low Osm treatment specimens which exhibited a significant decrease in light transmittance that appears to be dependent on both pH and osmolarity. Low osmolarity, Low pH equilibrated corneas exhibit a significant decrease in optical transparency (in UVA/VIS spectrum)

particularly in the blue-UVA range. Increase in scattering in this region typically suggests an uptake in water of the corneas resulting from swelling however thickness measurements made for specimens suggest no statistically significant difference between treatments (Figure 8.1-1).

4.2.3 Influence of osmotic pressure on corneal viscoelastic properties

In addition to it transparency, the cornea has a unique tissue scale structure that enables it to optimally refract and focus light. This domed transparent morphology is also critical for adequately resisting deformation from intraocular pressure. In this case the cornea, in addition to being under a constant state of deturgescence and pre-stress, experiences compressive forces as high as 1.45N (12kPa) from the vitreous humour and the eyelids during sleep as well as strong shearing from the eyelids during blinking and eye movements [38]. Seeing as the physiological state of the cornea necessitates both optical and mechanical competence, coupled with the high sensitivity the cornea displays in response to hydration state, it is logical to assess the corneal viscoelastic properties in relation to this parameter. Viscoelastic properties were assessed by employing a compressive stress relaxation (SR) dynamic mechanical analysis. In this experiment, corneas were equilibrated in their respective osmolarity treatment buffer and tested in their equilibration solution. In so doing, this allowed the corneas to remain in their respective hydration states during the entire duration of the experiment. Six distinct equilibration osmolarities were used between 1.5% - 20% PEG.

Stress relaxation tests reveal that there is a marked decrease in the relaxation as a function of PEG concentration and, by extension, hydration (Figure 4.2-4). Additionally, the shape of the relaxation curve seems to be changing in response to osmotic pressure. Furthermore, in terms of final relaxation force, there seems to be a statistically significant and progressive increase in the terminal relaxation force (Figure 4.2-5) indicating a stiffer, less responsive material.

To quantify differences in the progressive change in relaxation rate in response to changes in osmolarity, a non-linear viscoelastic exponential model was fitted to the data using an in-house MATLAB script (8.2.2). In so doing, parameters of the various models could be compared to elucidate differences between behaviours of treatments (Figure 4.2-6). Although non-linear viscoelastic models can be occasionally difficult to fit to experimental stress relaxation data, previous work has shown that hydrated tissues almost always exhibit non-linear viscoelastic (NLVE) behaviour – a characteristic and consequence of their highly hydrated hierarchically arranged structures.

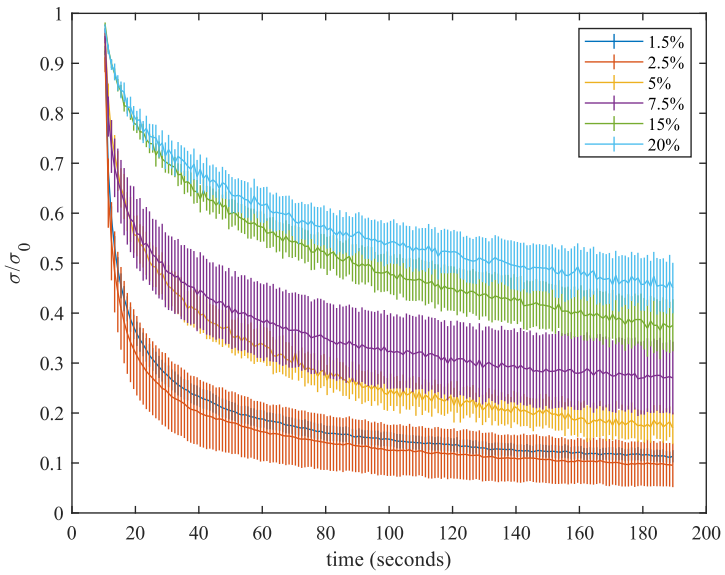

Figure 4.2-4: Stress relaxation behaviour of corneas as a function of PEG concentration. N=9 for each solution. Error bars are standard deviation. A clear distinction in NLVE behaviour can be seen between the low (1.5%, 2.5%), physiological range (5%, 7.5%), and high (15%, 20%) osmotic pressure range. Edematous corneas appear to exhibit very rapid relaxation rates

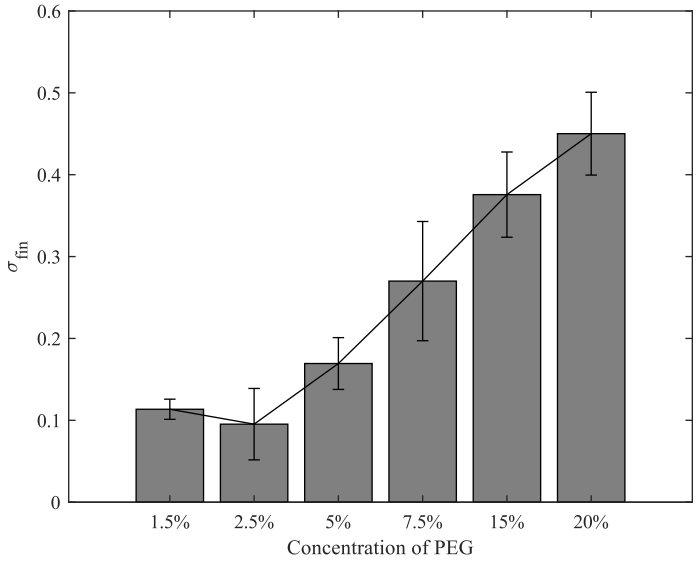

Figure 4.2-5: Final relaxation forces of the varying osmotic pressure of the cornea. N=9 for each treatment. Error bars are standard deviation. A progressive stiffening trend can be seen as the osmotic pressure of solution is increased which is indicated by a reduction in the final relaxation force of the tissue at the end of the experiment.

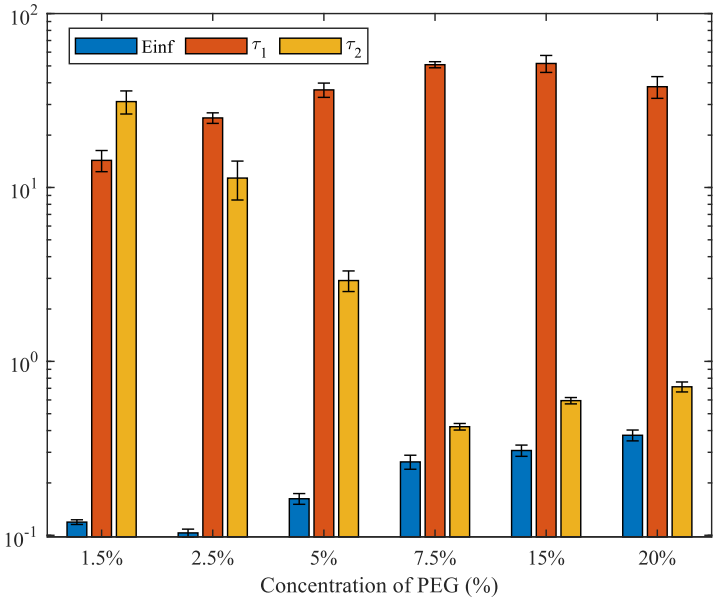

Figure 4.2-6: Influence of Corneal viscoelastic properties from changing osmotic pressure. Parameters of QLV model for relaxation response suggest a significant difference in the viscoelastic properties as a function of dehydration. A consistent decrease in relaxation parameter τ_1 was observed as the cornea progressively dehydrates from an edematous state to one that is below physiological hydration, indicating the importance of interstitial water in the responsiveness of the tissue.

From these analyses it is apparent that there is a significant difference in the decay parameters used in the exponential model to describe the NLVE behaviour of the cornea under SR. This NLVE behaviour is not limited to macroscale hierarchical structure, in fact, collagen fibrils themselves, being a hierarchical structure, seem to exhibit similar behaviour [69]. Physically, this indicates that the flexibility of fibrillar structures is decreased with an increase in osmolarity via the progressive dehydration of the IFM and progressive conformational changes in the collagen fibrillar and molecular structure [56,70]. It also indicates that the highly hydrated oedematous corneas relax very quickly because excess water is easily effused from the matrix. The ability for the physiologically equilibrated cornea to exhibit a considerably higher force also suggests that it is able to retain and compartmentalise water optimally.

Corneal thickness measurements as a function of osmolarity (Figure 4.2-7) demonstrate that reducing the osmolarity of the cornea results in a significant swelling of the cornea due to the retention of water by PGs. Additionally, we observe an increase in measured thickness as osmolarity increases to levels much higher than the osmotic pressure found in the cornea. This

phenomenon suggests that the fibrils are likely contracting and becoming wavy – inducing an increase in thickness as a function of dehydration increase.

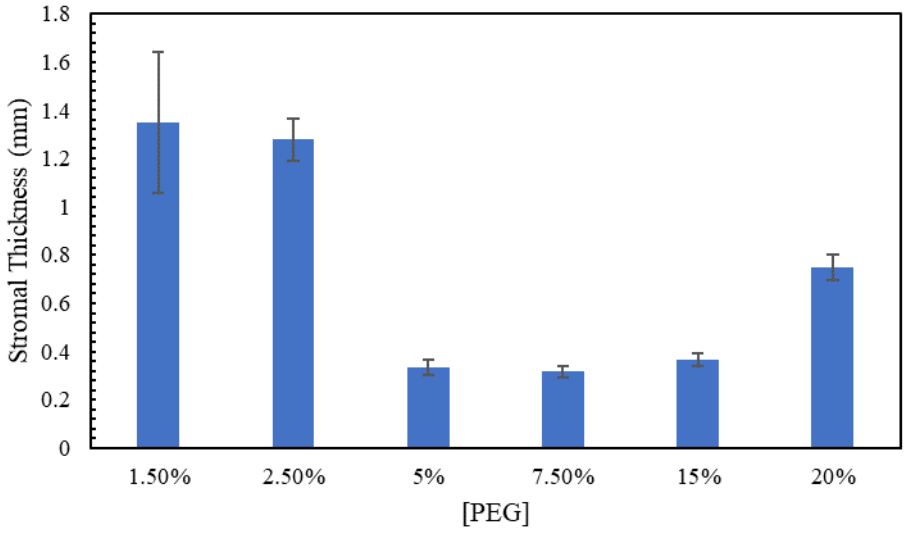

Figure 4.2-7: Corneal thickness measurements as a function of equilibration buffer osmolarity. n = 9 for each sample. Nonlinear behaviour of corneal thickness with respect to hydration likely stems from hierarchical complexity of tissue. The low osmotic pressure treatments (1.5%, 2.5%) exhibit an increase in thickness as a result of swelling. The high osmotic pressure treatments (15%, 20%) likely exhibit an increase in the measured thickness from an increase in folds and distortions cause by stresses induced upon drying.

Ultimately these findings illustrate the interdependence between hydration forces in the cornea and their relationship to osmolarity. Future work will expand on these finding to enhance the resolution and sensitivity of the preliminary techniques and findings highlighted in this section.

4.3 Investigation Of Corneal Ultrastructure

Coarse-grained simulations indicate clearly that there is a strong dependency of interactions between fibrils and larger structures that are heavily dependent on their geometry. In fact, in many cases, it is the geometry coupled with the presentation of hydrophilic groups that ultimately dictate the water sorption capabilities of the tissue. Furthermore, physicochemical properties of the cornea are predicted partially from the arrangement and interaction of macromolecular aggregates within the tissue. For example, being a heterogenous hydrated multiphase material allows collagen and the cornea to exhibit unique NLVE behaviour. It is thus

imperative that to further refine models to understand how hydration affects nanoscale, microscale and mesoscale structures, a thorough multiscale structural analysis of the corneal stroma should be conducted. By contextualizing nanoscale morphological features within a broader 3D tissue architecture, this study could enable the development of more comprehensive models for microscale and mesoscale interactions in the cornea. Accordingly, fresh salmon corneas were harvested and subjected to a rigorous electron microscopy protocol that made them amenable to 3D visualization using high-resolution focused ion beam scanning electron microscopy (FIB-SEM).

This tomographic technique enables the 3D visualisation of specimens at the submicron scale by intermittently ablating material from the surface of the specimen block face and then subsequently scanning the specimen with a rastering electron beam. These slices are then processed and compiled into 3D volumes which can be processed, subdivided, and segmented for further analysis.

Preliminary inspection of entire volumes reveals well defined lamellar structures running parallel to one another. The keratocyte cell population within the stroma is quite sparse and that is reflected in the represented full volume (Figure 4.3-1).

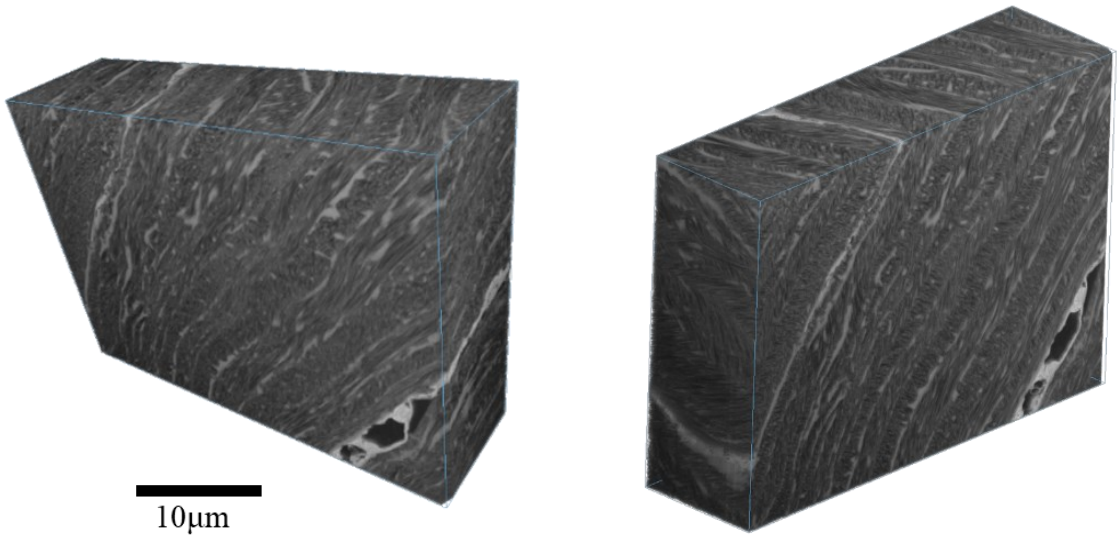

Figure 4.3-1: Tissue volume 1 of cornea displaying lamellar arrangement and a single keratocyte. Size of volume (18 x 10 x 7µm) with 5nm voxel size. The volume exhibits a large c view of the corneal stroma with visualizable fibrillar architecture that enables a contextualised understanding of how fibrils are arranged into larger lamellar structures.

During selection of regions of interest for slice and view, the entire cross section of the corneal stroma was exposed. Imaging with a pixel size of 5nm enabled a high resolution "google maps" like view of the corneal stroma cross section with adequate resolution to visualise individual fibrils. This allowed for the determination of key morphological changes in the stromal lamellae as a function of stromal depth (Figure 4.3-2).

This analysis reveals four distinct morphological regions that seem to exhibit a depth dependence. At the anterior portion of the stroma, the area responsible for the majority of the curvature of the cornea [71], there exists undulating lamellar layers which exhibit considerably higher thickness in comparison to the other probed regions. The central portion of the cornea exhibits a keratocyte-rich twisted ribbon-like fibrillar motif which seems to be a common morphological feature in most vertebrates [72]. The posterior portion of the stroma exhibits a thin and highly ordered lamellar motif in which the layers likely only consist of some dozen fibrils. Finally, like most other corneas, the salmon cornea has a disordered far posterior portion which is believed to primarily be structural in nature and play little role in light scattering.

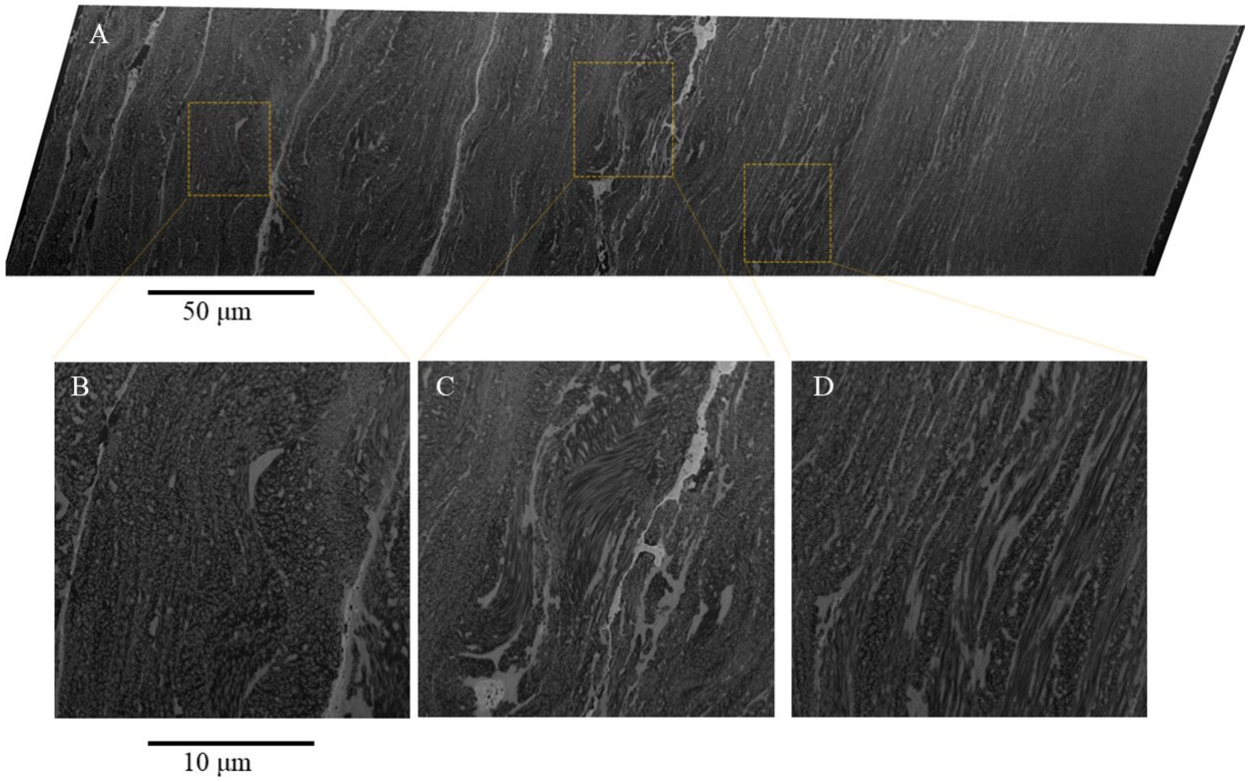

Figure 4.3-2: High-resolution (5nm) SEM overview of entire stromal cross-section (320 µm) showing fibrillar level and lamellar level architectural diversity (A). Three main morphologies

exist in a depth dependent manner: the undulating thick lamellar layers in the anterior stroma (B); the central keratocyte-rich twisted motif of the central stroma (C) and the well defined thin striated pattern of the anterior stroma (D).

4.3.1 Lamellar anastomosing in salmon cornea

Finding from these SEM analyses also reveal lamellar anastomosing also known as lamellar branching in the salmon cornea (Figure 4.3-3) – A structural feature thought only to exist in reptiles and birds [73]. It is posited here that these branching structures form a bicontinuous surface that allows the cornea to maintain toughness and resist extensive delamination during swelling despite being composed of ~80 wt.% water.

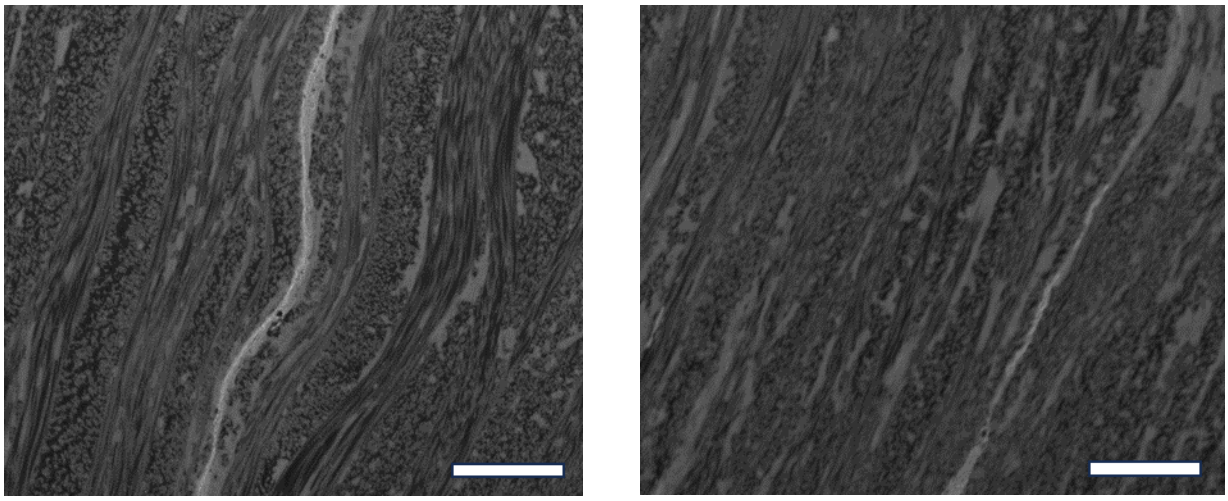

(A) (B)

Figure 4.3-3: Extensive lamellar anastomosing in central (A) and posterior (B) stroma. Scale bar corresponds to 2μm.

4.3.2 Fibrillar orientation and lamellar morphology in posterior stroma

After performing slice and view procedures on the selected regions of interest, a subvolume from the posterior portion of the stroma was selected to visualize the preferred fibrillar orientation in between adjacent lamellar layers. Qualitative inspection of fibrillar orientation between layers reveals that there exists a consistent angular offset in the preferred orientation of the fibrils (Figure 4.3-4). Furthermore, this orientation appears to be consistent for

dozens of microns in either direction only being interrupted by undulation or the radius of curvature of the tissue itself.

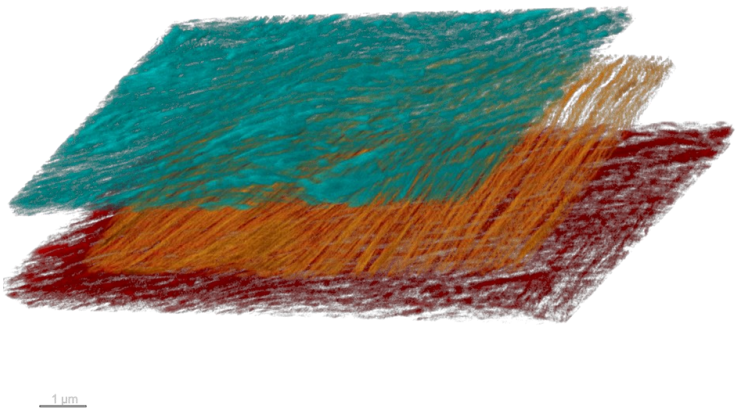

Figure 4.3-4: Segmented fibrils from three adjacent lamellae showing highly anisotropic arrangement of fibrils.

A conventional structural paradigm of the corneal stroma is that fibrils exist at nearly perfect orthogonal arrangements between adjacent lamellae [46]. Visual inspection of this arrangement immediately suggests that fibrils do not exhibit a perfect 90-degree lamellar arrangement but rather are offset by some acute angle. This is in contrast to observations made by Young et al. [18] which suggest a strong preference for orthogonality within the system. Similarly, Lee et al. employed SHG microscopy to quantify arrangement of fibrils and found a similar preference for fibrillar orientation within the stroma [74]. This discrepancy could be the result of interspecies variations between the angular offset of fibrils between salmon and the chicken.

To quantify changes in preferred fibrillar orientation between a small subvolume containing seemingly parallel lamellae. The stack was subdivided into multiple smaller stacks containing at least three lamellar layers. Volumes were resliced so that the longitudinal axis of fibrillar orientation was parallel to the slicing plane. An in-house code in MATLAB was then used to compute an FFT of every slice to obtain the change in preferred directionality of the fibrils along the depth of the stroma (Figure 4.3-5). Directionality was determined by

azimuthally integrating the FFT to obtain preferred fibrillar orientation as a function of stack depth.

4.3.3 Fibrillar orientation directionality analysis

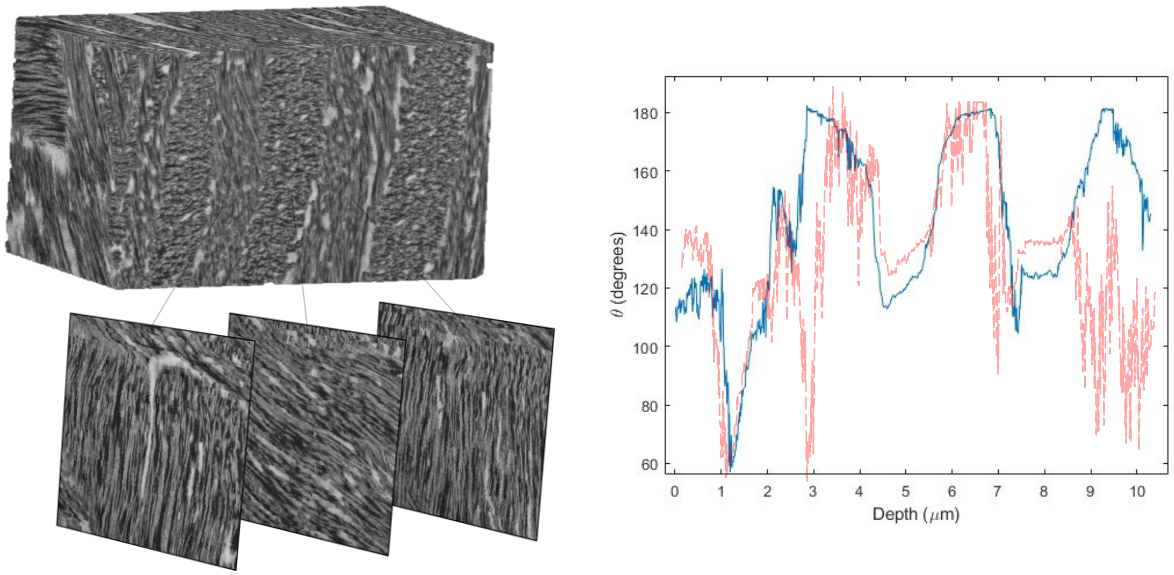

(A) (B)

Figure 4.3-5: Quantitative directionality analysis of fibril orientation as a function of stromal depth. (A) Example of 5 x 5 x 10µm subvolume used in directionality analysis showing representative slices with co-aligned fibrils in slicing plane. (B) FFT derived fibrillar orientation as a function of stromal depth for two laterally adjacent subvolumes.

Although these results indicate a deviation from what is typically observed in the stroma of other vertebrates. Most techniques do not obtain the same resolution as this study, nor do they account for curvature or undulations within the stroma. However, the study presented here is limited in that corneas are not in their natively hydrated state but instead were processed with conventional electron microscopy specimen preparation protocols which may have an affect on the morphological features in the stroma. Nevertheless, it is unlikely that dehydration can induce such a significant rotational change in a relatively large lamellar structure that can persist for hundreds of microns radially.

5 DISCUSSION OF RESULTS AND CONCLUSIONS

5.1 Compartmentalization of Water Niches in the Corneal Stroma

As exemplified in the beginning of this thesis, the cornea is a highly hydrated and hierarchically structured connective tissue that requires the maintenance of osmotic homeostasis and a hypertonic environment in order to perform adequately both as a refractive lens and a protective sheath for the vertebrate camera eye. As described in section 4.3, it is evident that there exists a high degree of diversity and complexity in the cornea that extends beyond the 2D structural paradigm of the tissue having straight, orthogonally arranged, and highly ordered lamellar sheets. Nevertheless, simplification of geometry is useful in many cases to elucidate underlying biophysical interactions in this system. These biophysical interactions should be major predictors for explaining whole tissue hydration properties as the collagenous macromolecular aggregates participating in these interactions make up over 90% by mass of the proteinaceous content in the cornea. Moreover, these biophysical interactions seem to play an integral role in how water is spatially arranged within the cornea and, by extension, the way the cornea responds to changes in factors that may affect the solvation or water interfacing of these constitutive elements.

Ultimately, there seems to exist some bi-directional relationship in between the hydration mediated forces in the cornea and the corresponding way in which water is compartmentalized in various “hydration niches”, a term we coin here. For a hydration niche to exist it must interface strongly with water by presenting a high density of hydrophilic groups on the solvent accessible surface or interfaces of the structure (whether it be 1nm or 1cm). Additionally, hierarchical complexity in biomaterials like collagenous tissues can enable the confinement of water in sealed or diffusion limited spaces. To achieve long term binding of water to these interfaces, the binding energy of water to a hydrophilic ligand (either through electrostatics or polar forces) must be greater than the binding energy that water has with itself. This wettability understanding is typically used in descriptions for water sorption to the surface of charged groups on mineral interfaces [75] or the binding of water to ions [76] but, to our knowledge, has never explicitly been employed for charged organic polymers.

It should be mentioned that, although binding of water is considered here as long-term, this does not mean that there is no diffusive exchange between the bound water and the free water fractions. In general, even bound and confined water systems participate in diffusive

processes (albeit with a lower diffusive flux) with the bulk solvent. This statistical thermodynamic perspective [77] is far more nuanced than the idea of a water molecule never interacting with the bulk solvent. However, the lability of water is still heavily limited compared to the bulk, likely exhibiting different properties such as: density , dielectric constant [78] and hydrogen bond structure [79] as revealed predominantly through HNMR analyses.

The coarse-grained multiscale simulations proposed here (4.1) suggests that there exist at least two distinct fractions of highly structured bound water within the corneal stroma. Additionally, even more highly hydrated hierarchically structured niches exist in the stroma that also have large interfaces with weak interactions with the interstitial solvent and solutes that likely need further exploration.

5.1.1 Intrafibrillar water

At the sub-fibrillar level, tropocollagen triple helices exhibit a hydrated coating around them that can be 2-3 molecular waters wide. Although this has been validated experimentally with a combination of x-ray scattering and spectroscopy [31,58], this is the first time a fundamental physical model was used to explain this phenomenon by combining various short-range interfacial forces. It is also the first time the binding energy of these intimate interactions has been quantified. Simulations and experimental findings reveal that before a threshold of 17Å, repulsive forces predominate between adjacent triple helices, however, after that distance, attractive forces begin to predominate. This observation is in good agreement with dehydration transitions observed in other highly hydrated interfacing structures such as lipid bilayers [59]. This suggests that as collagen fibrils dehydrate (whether through changes in osmotic pressure or physical dehydration), the morphology of the intrafibrillar surface begins to change as the triple helices begin to exert repulsive forces on one another. This topological change can be directly inferred by changes to measurable parameters such as helical pitch [56]. This is in contrast to molecular dynamics simulations that predict a reduction in intermolecular sliding between the helices as the spacing between them decreases [80].

Crystallographic studies of collagen fibrils suggest that there exists a complex relationship between the structure of tropocollagen in relation to the hydration state of its supramolecular assembly [81]. The intermolecular spacing (IMS - the spacing between tropocollagen triple helices in a fibril) in collagen is small enough that the topology of the solvent accessible surface of the protein is extremely relevant. In reality, the “hydration shell”

surrounding the tropocollagen helix should not be considered as a uniform cylindrical shell but rather a complex, interconnected hydration network that facilitates solvation of the molecular assembly. This network-like view of tropocollagen hydration is more amenable to the actual experimental behaviour of the protein at the sub-nanometre scale. Particularly the non-discreteness of the linear relationship between the IMS and the hydration state of the bulk tissue [55,82] (in contrast to a step-wise desorption of discrete hydration layers from the surface of the triple helix). Additionally, due to the 64nm molecular stagger [83] of the macromolecular assembly and the highly hydrated interfaces that encompass them, the water bridging that occurs between these interfaces are likely to be very diverse in nature [79,84] (Figure 1.4-1). Since water presents two hydrogen bond donors and two acceptors it is amenable to form 3D-branched water networks [52]. The implications of this, as well as evidence for this in the context of collagen subfibrillar structures has still been yet to be explored. However, experimentally, it is known that removal of intrafibrillar water can affect the nanomechanical properties of the whole fibril [61,69,85]. The implications of this are that when fibrils are under tension, the state of prestress changes allowing tropocollagen molecules to exhibit attractive cohesive forces between them rather than disaggregating from each other. Ultimately, according to our simulations, this water accounts for roughly 10% of the total mass of water found in the cornea. Finally, since electrostatics was not considered but result still yielded predictable values, it is assumed here that electrostatic interactions play a negligible role in intrafibrillar cohesion at this level.

5.1.2 PG-Bound interfibrillar water

The highly non-linear behaviour of tropocollagen helical arrays in relation to their hydration environment also has greater implications on the properties of the entire fibril – being involved in the prestresses within the fibrils that mediate their responsiveness to the tensile stresses [85]. Ultimately, by retaining water, the cohesive properties of fibrils actually increase allowing for a more mechanically competent fibril under tension [85].

The interactions between fibrils occur on a length scale that is one to two orders of magnitude larger than the intimate interactions that occur between individual tropocollagen helices. At this scale, the collagen fibrils are separated by a spacing (from surface to surface) that is roughly equal to their diameter (24nm). At this length, only electrostatic interactions between adjacent fibrils can extend far enough to exert any appreciable forces on fibrillar surfaces. Additionally, the endogenous osmotic pressure exerted by interstitial proteoglycans (ie. those

which are not covalently linked to fibril surface) can itself aid in the repulsion of the fibrils by affecting the "osmotically available water" [82]. Finally, although not considered in the simulations described here, steric repulsion and thermal fluctuations of these large polymeric chains may also contribute to optimal spacing. The water that is tightly bound in this niche appears to entrap a relatively large (3nm) hydration shell on the surface of the fibrils which accounts for roughly 8% of the total mass of the water in the cornea at physiological hydration. These first principle calculations are, in fact, consistent with experimental observations which deduced that corneal fibrils have a 3.5nm coating of PGs on their surface [57]. This relatively large quantity of hard to remove bound water plays a crucial role in maintaining the immediate hydrated interface surrounding the fibrils. We speculate that the PGs existing as a wrapped hydrated polyelectrolytic coating that encompasses the fibrils could be a hydration reserve or an osmolarity controller to maintain optimal water scaffolding within the fibril. In vivo, the corneal ECM is in a constant state of deturgescence through the active ion transport from the epithelium and thus may be exerting osmotic control on this fibrillar coat by this means. The maintenance of a constant anion surplus in the corneal ECM [86] allows for the enhancement of repulsive forces between adjacent fibrils – maintaining optimal turgor pressure and inhibiting swelling.

By adding exogenous osmotically active agents in the cornea, the ECM is effectively dehydrated by competing with the water sorption of endogenous osmotic agents. This shifts the equilibrium between the free water and bound water fractions that, as can be seen from the simulations, reduces the magnitude of water sorption on the fibrillar surface.

It should be noted that the interfibrillar interactions in reality cannot be considered just as two distinct well-defined boundaries but rather a system of diffuse boundaries that are subjected to variations in thermal motion. Additionally, because the calculations for water binding are based on empirical relationships of the corneal ultrastructure as a function of dehydration, the simulations become increasingly more inaccurate as the hydration state of the cornea approaches anhydrous conditions. However, simulations employing first-principle physical phenomena to describe bound water seem, for all intents and purposes, accurate enough to predict bound water fractions and their dependency on primarily electrostatic mediated sorption within the near physiological range of hydration.

5.1.3 Interlamellar boundary and cellular water fractions

The preliminary FEA of the cornea reveals that the interlamellar boundary is often a common region for the diffusive exchange for nutrients and solutes. In preliminary FIB-SEM visualisation, a similar occurrence of stratified voids occurs along the length of these interlamellar boundaries. It is not yet apparent what causes these dramatic shifts in fibrillar orientation or what is moderating it. Future high-resolution studies employing electron tomography will attempt to explain this behaviour mechanistically and attempt to elucidate constitutional differences and putative proteins involved in regulating this microstructure. The cell water fraction is extremely labile and likely contributes little to the bound fraction of the total tissue considering that cells make up only 5-10% by volume of the total tissue. This is because, in addition to the cell fractions being relatively small, their water binding contribution from glycocalyx and cytosolic proteins contribute little to the morphology of the stroma. Although mostly qualitative in nature, the FEA does open doors to future studies to model mass transport processes within the complex nanochanneled architecture of the corneal stroma.

5.2 Experimental Evidence of Two Discrete Bound-Water Fractions

Seeing as the cornea is essentially a structured polyelectrolytic gel, it effectively undergoes a form of syneresis when removed from an equilibrating solution. This phenomenon likely stems from the GAGs contained in the tissue [87]. This rapid loss of bulk interstitial water demonstrates that a large fraction of the cornea is amenable to diffusive exchange of nutrients and metabolic by-products. However, this fraction, accounting for roughly 80% of the water in the system [36], is desorbed quickly even with gentle convection at room temperature and thus accounts for most of the total mass change measured by the cornea. This makes the measurement of the smaller fractions of bound water in the cornea inherently difficult to measure and may compromise the measurement sensitivity of the apparatus. To circumvent this, the cornea was allowed to desiccate at room temperature until its weight stabilized.

Considering that almost 70% of the mass of the cornea was desorbed at this point, this was considered an effectively bulk water-free tissue. Doing this greatly enhanced the sensitivity of the system and revealed that the cornea has at least two distinct fractions of bound water associated with it. However, in the small sample size tested, the total mass only accounted for roughly 12 ± 3% by mass of the dried cornea (Figure 4.2-1) which would amount to roughly only 3% of the physiologically hydrated cornea. This suggests that the simulations may be

overestimating the amount of water fractions or that the model for water sorption used was incomplete. One consistent observation made for all three tests were the initial increase in mass at the beginning of the experiment, suggesting that the cornea was absorbing some entrained humidity from the N_2 line that passes over the specimens. It is thus possible that desiccation may not be the ideal way to prepare the specimen and that future high-resolution tests should instead allow preliminary desiccation of corneas in the actual TGA furnace. In any case, results support the possible existence of a two-component bound water fraction in the system in addition to the labile FW.

Considering that every amino acid residue within the collagen secondary structure is solvated, there are likely crucial water bridges that are structurally integral to maintaining normal triple helical conformation [81]. Furthermore, there is, in reality, likely a spectrum of sorption affinity based on the relative electrostatic potential and polar forces within the fibrils and on the hydrated coat surrounding the fibril. The idea of monolayer-like coverage of water molecules surrounding individual tropocollagen molecules[58] is thus likely to be more nuanced. TGA has not been used explicitly to estimate BW fractions in the cornea but other techniques such as DSC and ssNMR have been used successfully. The measurement made with DSC suggest a nearly 20% bound water fraction within corneal specimens [36] which is more consistent with theoretical simulations made in this thesis (Table 4.1-1). Conversely, another group found that the total bound water content in the cornea amounts to just ~2.6% of the total water in the system and thus claims that most of the corneal water is amenable to nutrient exchange [34] and traffic. This finding is more consistent with the TGA measurements made in this study which estimated a 3% bound water fraction and highlights the nuanced definition of what can be considered bound water. Ultimately, in these cases, two separate techniques are used to quantify the amount of bound water in the corneal ECM and thus two very distinct explanations for what constitutes bound water are implemented.

Based on quantitative values for binding energy derived from multiscale simulations of the corneal ECM, it is thus possible to speculate on which fraction of the corneal ECM would dehydrate first. Counterintuitively, the retention of water by PGs in the IFM and coating the fibril surface would retain water with a higher affinity than the hydrated tropocollagen helices within the fibril. This is a consequence of the water having a higher affinity for the high potential of the charged groups on the PGs and the increasing concentration of cationic species that are

localizing to the PG surface from the interstitial solvent during dehydration. This is quite counterintuitive because it implies that the collagen-PG fibrillar aggregate must dry from the inside out. This is atypical of most homogeneous materials but has been observed in concentrated polymeric droplets [88]. This phenomenon, known colloquially as the "coffee ring effect" [89] occurs when the heating of a small volumetric particles causes mass transport and capillary action to preferentially draw solvent and solutes to the surface of the particle drawing water away from the centre. Provided this mechanism holds it is thus possible that the PGs and tropocollagen dehydrate simultaneously which contributes to the first portion of the curve where the majority of the water is being desorbed. As the dehydration progresses, the IFM continues to become enriched with solvent and solutes that strongly retain water until the centre of the fibril is nearly anhydrous. Then, the remaining water sorbed to the PGs on the fibrillar surface would be removed from the tissue – effectively removing the remainder of the BW in the system.

5.3 Hydration in the Role of Physicochemical Properties

Analysis of fibrillar level interactions from other studies [90] note that the interfibrillar long-range interactions are predominantly mediated by the bridging of proteoglycans instead of the ones that coat the surface. The ones that coat the surface are likely larger contributors to water sorption though and are likely to mediate fibril nanomechanics (because they are more populous). It appears that, from simulations, there is little effect on the electrostatic interactions from the fibrillar surface until they are within 10nm of one another. Nevertheless, there does seem to be some predictable trend in the stress relaxation response of the cornea in relation to osmotic pressure of the equilibrating buffer. As the cornea dehydrates through an exogenous osmotic pressure from a PEG solution, the interfibrillar distance between the fibrils decreases by removing some of the weakly interacting water. This, in turn allows for stronger confinement of the interstitial and surface PGs and reduces their water holding capability.

The cornea is a biphasic system that exudes water under compression, therefore, the more bulk water the cornea has in proportion to its overall mass, the more quickly it appears to relax. During exposure to an exogenous osmotic pressure, the bulk water content is changed. Considering that there is a below saturation level of free water in the system, this implies that water in the fibril will be redistributed to the PG sheath that surrounds the fibrils possibly making them stiffer. Future endeavours should attempt to relate compositional differences between the IFM and fibrils in a biphasic model to describe the viscoelastic behaviour of the whole stroma.

More holistically, it is apparent that changing the osmotic pressure of the cornea directly influences prestress within the stroma. Furthermore, this change in prestress seems to have a significant influence over the mechanical properties of the cornea in compression. In particular, the viscous contribution of water to the system seems to be reduced – further attesting to the importance of maintaining an optimal hydration environment in the stroma. Since, theoretically, there appears to be a relationship between the bound water content in the stroma and the hydration of the tissue, it is conceivable that bound water in the cornea could mediate the relationship between viscoelastic properties and hydration state of the tissue.

Although corneal viscoelasticity has been analysed previously[43,91–93], this is the first time the viscoelastic properties of the tissue were related to their hydration state. Furthermore, this is the first time a QLV model was applied to describe corneal viscoelasticity under compression. Considering that the cornea experiences an array of mechanical stimuli from blinking, eye-rubbing, and intraocular pressure changes; the elucidation of the corneal non-linear viscoelastic behaviour under compression is highly relevant.

The electrostatic restoring forces in the cornea are quite weak suggesting that they play more of a structural role in reducing light scattering (by regulating fibril morphology) than they contribute to mechanical compliance. Nevertheless, the exertion of a high osmotic pressure on the corneal stroma will alter fibril nanomechanics and in turn influence the bulk tissue properties of the fibril [85]. In fact, we speculate that most of the minor hydration dependent changes occurring here might be a combination of both a reduction in swelling of interstitial PGs and the increase in intrafibrillar cohesion resulting from alteration to the SAS of tropocollagen.

The light scattering differences in these experiments likely emanate from a combination of lakes which are small water-filled voids that populate the corneal stroma (Figure 4.3-2) and changes to the water distribution between the fibril and the IFM. Additionally, keratocytes which typically match the refractive index of the corneal ECM may also swell to reduce transparency and increase light scattering [15]. Light scattering of the cornea reported here at physiological pH and hydration exhibited similar transmittance to observations others have made for rabbit corneas [27]. However, in that study pH and hydration state were not explored. The influence of pH within the physiologically relevant range has been explored with little derivable conclusions except that the slight increase in pH may affect the swelling rate of the cornea but not the final swollen height [68].

Despite posited changes in water retention induced by pH and osmotic pressure, stromal thickness seems not to vary between the four treatment regimes (Figure 8.1-1). This suggests that either the measurement for stromal thickness was not sensitive enough or that water is simply being redistributed in the stroma rather than causing an increase in water retention. This could be a consequence of Histidine residues in collagen which are relatively sparse but contribute substantially to surface charge and are important in crosslinking [45]. Histidine has a pKa of side chain of pH 6 and thus could be deprotonated at the low pH treatment – contributing to this phenomenon by drawing more water to the fibril surface or promoting electrostatic interactions between PGs and these residues. Another possibility is that the overall water sorption capabilities of polyanionic PGs decreases during a decrease in pH which may affect the fibril morphology. Ultimately, there are some findings that indicate some nominal change of corneal light scattering and morphology in relation to physiologically relevant pH changes [31,94]. However, it is unclear whether this phenomenon is a consequence of pH or whether the morphological changes are associated with pH changes from dysregulation of normal corneal epithelial cell function [68]. This phenomenon, if not a consequence of water redistribution at the nanoscale, could be a consequence of microscale morphological changes such as lamellar folding or waviness as a consequence of dehydration or pH change.

These properties in relation to the bound water fractions of the cornea need to be explored in greater detail. In particular, the simulations and literature sources suggest that the bound water fraction within the tissue may only be moderately susceptible to variations in osmotic pressure. In contrast, it is posited from the PBE that changes in ionic strength will more strongly influence the endogenous osmotic forces in the cornea, by condensing GAGs, while retaining the bulk water content of the tissue almost unchanged. More specifically, from the DVLO theory of electrostatics, it is predicted that divalent cations (Ca^{2+} , Mg^{2+}) should have a pronounced effect on the water sorption properties of GAGs [65,87,95] .

5.4 Contextualized Fibrillar Architecture in The Corneal Stroma and its Relationship to Hydration

Despite the generally accepted structural paradigm that the cornea exhibits a highly ordered orthogonal arrangement of collagen fibrils, the reality is that the tissue displays much more hierarchical complexity than conventionally thought. In particular, the arrangement of the lamellar layers does not seem to abide by this highly orthogonal structural paradigm but rather

has a variable offset depending on the stromal depth [96]. Furthermore, previous observations employing cryogenically prepared specimens suggest that the stroma may in fact exhibit super lamellar structures with bundle-like morphologies [12] but that these bundle-like structures are flattened in comparison to what is observed in other tissues. Instead of having annular cross-sections, it appears that the corneal stroma exhibits ellipsoid-like bundle arrangements, in which the fibrillar anisotropy is very high [97]. This structural complexity provides a distinction to the conventional view of the highly ordered hand-picked representations of uniform crystalline-like arrangements of fibrils in orthogonal lamellae.

Previous evidence suggests a significant constitutional difference within the corneal stroma as a function of depth [33,98]. Visualizing these lamellar layers and potentially larger bundle like features, with the understanding of how PGs vary with depth may enable explanations for how the cornea maintains a domed shape despite being rather uniform in thickness [71]. In particular, others have noted the resistance of the anterior wavy portion of the stroma to variations in non-physiological hydration states [71]. In the cross section obtained, fibrillar bundles seemed to occur around where larger keratocyte processes were found and preferentially in the anterior-mid depth regions of the corneal stroma. Additionally, other studies have suggested that the lamellae of fish and shark exhibit little anastomosing. In contrast we see very well-defined branching structures that bridge layers indicating lamellar anastomosing (Figure 4.3-3) – a structural feature though to exist mostly in birds [72] and non-mammalian terrestrial vertebrates. The minimal lamellar branching observed by others could be a consequence of poor resolution considering that these branching patterns are sometimes only half a dozen fibrils wide (150 nm) and are thus unresolvable with light microscopy techniques.

The directionality analysis conducted on the high-resolution sub-volume of lamellar layers in the cornea suggest that the orientation of fibrils does not exhibit this conventionally assumed orthogonal lamellar architecture despite care being taken to visualize the central portion of the corneal button. A conventional structural paradigm of the corneal stroma is that fibrils exist at nearly perfect orthogonal arrangements between adjacent lamellae [46]. Quantitative directionality analysis of this arrangement (Figure 4.3-5) immediately suggests that fibrils do not exhibit a perfect 90-degree lamellar arrangement but rather are offset by 60 degrees. Furthermore, this arrangement seems to be consistent between lamellae exhibiting the same fibrillar orientation (between n and n+2 layers). This is in contrast to observations made by

others [18] which suggest a strong preference for orthogonality within the system when using second harmonic generation (SHG) light microscopy [74].

Limitations in this case compared to SHG is that this method can only probe a smaller area of interest relative to SHG which can probe the entire thickness of the corneal stroma. However, the spatial resolution (lateral: 0.5μm depth: 2μm) is much lower and errors associated with these measurements are much higher than those obtained from 3D FFT analyses of FIB-SEM volumes. Lastly the direction of analysis could also make a difference as most other studies conducted their analyses by adjusting the focal plane parallel to the axis of the stromal lamellar layers. However, in this case, in order to minimize possible variations associated with curvature in a larger field of view (FOV) the area of interest was reduced drastically until nearly abrupt transitions were perceivable between layers. By re-slicing along the fibrillar plane, a more precise view of the interlamellar angular offset was obtained that mitigates in-plane distortions caused by undulations or curvature.

Ultimately, more efforts will need to be made to relate these nano-microscale structural features to their respective role in maintaining optimal corneal hydration and structure. Although little evidence exists for the importance of this precise hierarchical complexity in water sorption, chromatographic separation of corneal constituents indicates that there is minimal hysteresis in water sorption for isolated cornea fractions in comparison to whole undigested tissues [9]. This suggests that there is a direct link for an interplay between the hierarchical complexity of the stroma and hydrophilic groups on the surface of proteoglycans and collagen involved in water binding. Additionally, there seems to be some fundamental biological process involved in ECM deposition and remodelling that facilitates the formation of these well-defined angular offsets in the corneal stroma that are, as of yet, still inadequately explained. These phenomena are in fact consistent with other connective tissue systems that exhibit similar plywood-like periodic arrangement of fibrils [99,100].

5.5 Generalizability to Mineralized Collagenous Tissues

As alluded to in 1.3, the cornea and bone share many morphological and constitutional similarities. Most notably, both are composed of Type 1 collagen functionalized with SLRPs arranged in a hierarchical fashion that favours the compartmentalisation of water. Furthermore, although existing at different length scales, both the cornea and compact bone have anisotropic lamellar layering of these collagen fibrils [1]. In contrast to these similarities, lamellae in the

cornea exist as flattened undulating structures but in bone fibrillar aggregates can form larger bundle like structures that have a more cylindrical cross-section. Moreover, the presence of mineral in bone likely increases the diversity of hydrated interfaces within this tissue. It is thus conceivable that the hierarchical arrangement of bone permits a similar compartmentalisation of water into structured hydration niches. In this case, the sorption of water can also be attributable to the macromolecular assemblies in the ECM but must also consider the water interfacing between these elements and mineral. In bone, an abundance of interstitial fluid is constantly perfusing through it – enabling the exchange and possible entrapment of metabolites within these interstices. This has become a relevant problem for a collaborator, Dr. Timothy Bromage (New York University College of Dentistry), who studies the ancient paleometabolome of rodent bones from the Olduvai Gorge in Namibia (Submitted to Nature Paleobiology). Using the multiscale framework for water sorption of CTs developed in this thesis, the concept of water (and solute) compartmentalisation was employed to explain the mechanism behind entrapment of ancient metabolites in these hierarchical niches of bone. Furthermore, this approach is also used to distinguish between hierarchical niches that are amenable to entrapment based on both their affinity and size exclusion characteristics.

The predominant mineral phase of bone – carbonated hydroxyapatite – possesses an ion-exchangeable surface in aqueous environments [101,102] that can readily bind and exchange ions and molecules [103]. It is now apparent that, *in vivo*, this adsorption is not limited to bone-specific and locally produced ions and molecules but also pertains to circulating metabolites that enter bone through its interstitial fluid. The adsorption is mediated predominantly by electrostatic interactions and the formation of coordination complexes with surface ions of the mineral phase [103]. The adsorption of metabolites to the surface of the crystallites, coupled with retention of water into bone's hierarchical structure, results in the entrapment of metabolites within a continuum of structural "niches" spanning the size scales from micrometers to nanometers. For a niche to be suitable for long-term metabolite entrapment and preservation in bone, on the paleology timescale, it must be accessible to the interstitial fluid (to allow metabolites in), and also shielded from taphonomic processes (to prevent metabolite loss). The broader and larger the scale of structural organization in bone, the more permeable the organic-inorganic interface is for metabolites, yet at the same time also for subsequent metabolite degradation and diagenetic events. Conversely, at the finer scale of bone mineral structure where there is generally less

permeability, metabolites may be sequestered and then shielded from degradation/loss – and thus remain detectable – as we have noted in this study. Therefore, we have considered the continuum of 3D sub-micrometer niches which can possibly harbor the paleometabolome, according to their permeability and scale (Figure 5.5-1).

5.5.1 Lacuno-canalicular network (10^{-6} m)

Based on (paleo)histological studies, the lacuno-canalicular network (LCN) is easily accessible to both metabolites and taphonomic agents like microbes and humic substances[104,105]. Numerous studies have demonstrated that the LCN is easily infiltrated by microorganisms like the hyphae of filamentous fungi[106] and by bacteria[107], and can serve as conduit for diagenetic processes. Enzymatic degradation and modification of the local microenvironment along the microbial ingress degrades collagen and noncollagenous proteins, resulting in reprecipitation of mineral phases and the loss of the pristine organic-inorganic interface[107,108]. Although the preservation of collagen in parts of the sample (Appendix) suggests that the diagenetic degradation was incomplete allowing for the preservation of some sub-micron structures, we view this niche as being of limited reliability for paleometabolome preservation, dependent on the burial conditions.

5.5.2 Interfaces between mineral tesselles (10^{-7} m)

In living bone, mineralization begins from quasi-regularly spaced mineralization foci[109,110] dispersed within a fibrous collagenous extracellular matrix. Mineral foci grow within the organic matrix to eventually pack into a 3D, space-filling array of similarly structured morphologies geometrically approximating prolate ellipsoids (with irregular jagged surfaces) about 1 micrometer in size, in a process termed crossfibrillar mineral tessellation[109]. Even mature mineral ellipsoids, called tesselles, have persistent discrete organic boundaries (as observed by electron microscopy) that do not exceed 100-200 nm. Such boundaries likely contain residual mineralization-inhibiting noncollagenous proteins/peptides and inhibitory small biomolecules that presumably impede complete fusion of the tesselles, thus providing a 3D tessellation pattern that imparts unique mechanical properties to bone [8,110]. This hundred-nanometer-scale compartment is thus a probable niche for paleometabolome preservation.

5.5.3 Interfaces between hydroxyapatite crystallite aggregates (10^{-8} m)

Gently twisted aggregates of stacked hydroxyapatite crystallites splay and merge throughout the continuous collagenous matrix[24,40]. Neighbouring aggregates envelope spaces that are, on average, about 20 nm wide and linear in the in-plane view, or 30-40 nm wide and lacy in the out-of-plane view [40]. Continuous with the collagen fibrils is an extended network of small proteoglycans (Small Leucine-Rich Proteoglycans, SLRPs) with chains of dermatan and chondroitin sulfate [10]. These charged proteoglycan chains can be up to 30 nm in length[5] and their networks can bridge this inter-crystallite aggregate niche, being on the order of magnitude of several thousands of cubic nanometres. Experimental evidence demonstrates an ionic dependence on cohesive forces between nanointerfaces of native bone suggesting that there are electrostatically mediated interactions between the charged proteoglycans and mineral surfaces in a hydrated environment[111]. Furthermore, *in situ* measurements of bone zeta potential suggest that the long-range (>10 nm) electrostatic effects on the surface are predominantly from charged protein groups [112]. Such a crowded molecular environment with an abundance of charged and polar residues can sequester metabolites, making this compartment a likely protected paleometabolome preservation niche.

5.5.4 Interface between adjacent crystallites (10^{-9} m)

This finest niche is uniformly sandwiched between congruent surfaces of adjacent hydroxyapatite crystallites and does not exceed a few nanometers in width. These uniform confined spaces are typically visible in thin sections of bone viewed by transmission electron microscopy[58,113,114]. Hydrated bone mineral bears a surface charge (-50 mV) and a corresponding surface potential gradient. The extent of the surface potential gradient is defined by complexation (through chemisorption) of water dipoles with under-coordinated surface ions. From simulations of hydroxyapatite electrostatics at physiological conditions, it is predicted that bone mineral crystallites have a relatively thick (2.7 nm) and strongly bound hydrated layer on their surfaces [115]. This layer thickness, known collectively as the Debye length, is composed of the Stern-Helmholtz and electric double layer – a dense ionic halo that acts as the interface in between the charged crystallite surface and the labile interstitial fluid. An effect of the surface charge is the condensation[116] of counter-ion species in nonstoichiometric quantities at this hydrated interfacial layer with the concentration of counter-ions being stabilized at orders of magnitude higher concentrations than what is seen in bulk solution[117]. It is postulated that the

electron-dense amorphous layer on the surface of hydrated hydroxyapatite could likely be highly structured electrostatically [113,114]. The electron-lucent 2 nm width between adjacent crystallite surfaces can accommodate as few as 5 water molecules spanning the gap [118]. Ionic crowding from the hydrated nonstoichiometric calcium phosphate layer, when coupled with confinement, would result in very poor permeability for circulating metabolites into these regions. Investigation of these hydrated mineral interfaces *in vitro* suggest that only very small metabolic products such as citrate [119], lactate and carbonates [120] might exist as inclusions in between these mineral facets [114], potentially responsible for the spacing of stacked plate-like nanocrystalline morphology often observed [114,121], perhaps occurring through chelation effects. This niche is thus unlikely to harbor the paleometabolome, attributable to a size exclusion limit that is far smaller than most metabolites detected in this study.

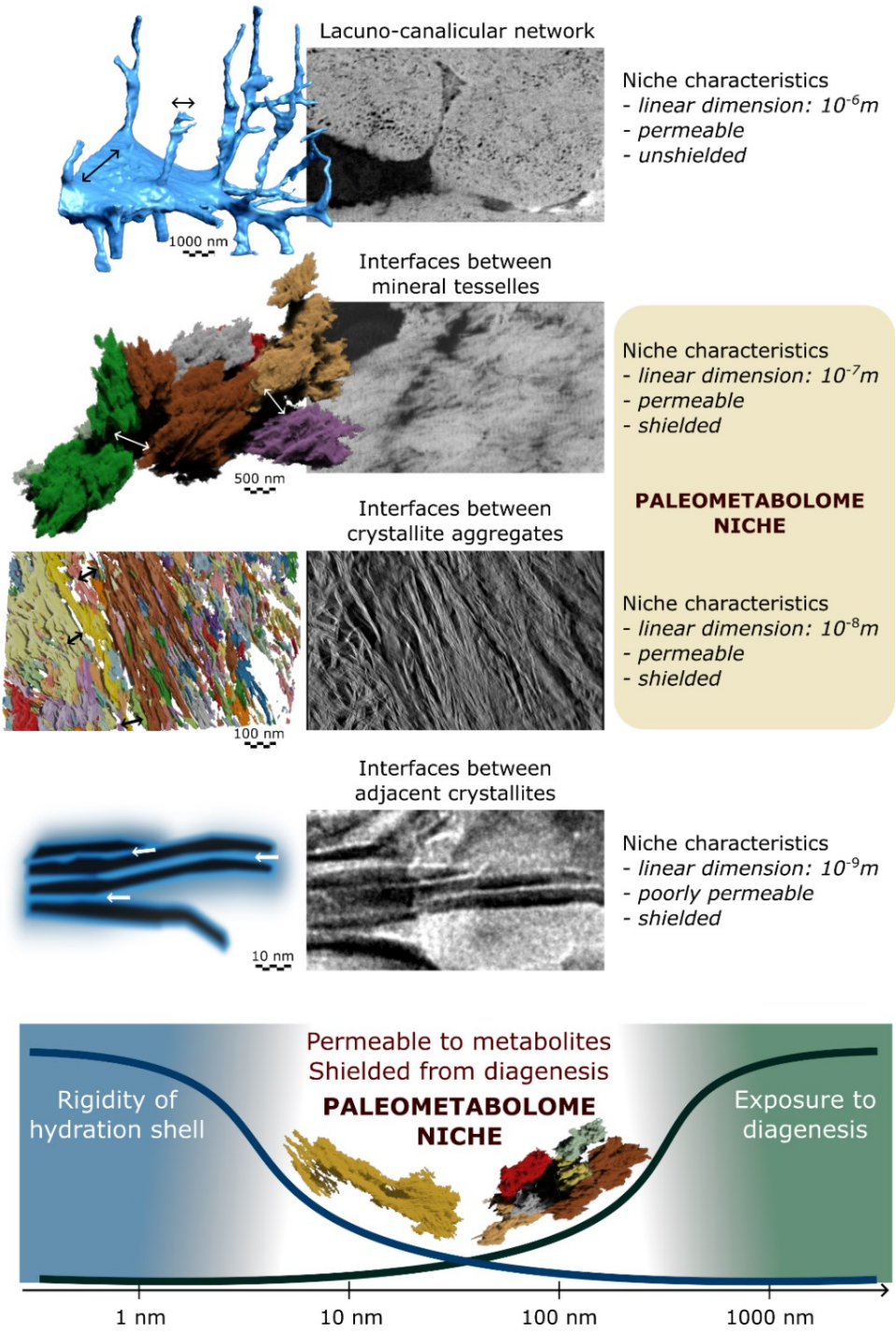

Adapted from Bromage et al., In preparation.

Figure 5.5-1: Overview of paleometabolome niches and their relationship to bound water in fossilized bone.

6 CONCLUDING REMARKS

6.1 Limitations of Current Studies and Outlook

The current studies were mainly limited in their ability to produce large sample sizes. Within time constraints of this master's thesis, the time-consuming nature of optimizing an EM processing protocol and analytical techniques for characterising bound water in corneal stroma limited the statistical robustness of many experiments. Accordingly, many of the experiments in this thesis will need to be replicated or will require more thorough investigation. Nevertheless, these preliminary findings establish a possible foundation for simulations and experimental techniques that may provide a holistic view of the hydration dependent structuring in the corneal stroma as well as other hierarchically structured and highly hydrated collagenous tissue systems.

In the future, some of these existing experiments will be coupled with spectroscopic techniques to unambiguously obtain metrics for the protein hydration in the corneal stroma. In particular, solid-state NMR spectroscopy can easily distinguish between diffusion limited and labile free water [35,51,114,122] and even provide information on strength of hydrogen bonding between solute and moieties on macromolecular aggregates. Furthermore, considering that no spectral evidence yet exists for the interactions of PGs in the intrafibrillar space, future experiments may make use of Raman spectroscopy [55,123] or other vibrational spectroscopies to elucidate the interactions between interfibrillar PGs and may reveal their dependency on their hydration environment.

6.2 Concluding Remarks on the Definition of Bound Water

Ultimately, most research agrees that there exists, in the very least, a distinct portion of water interacting with macromolecular assemblies in connective tissues known as bound water. Operationally, the definition of bound water depends on the experiments being performed or the theoretical basis used and is currently highly variable.

From a theoretical physical chemistry perspective, bound water should be any water which is hydrogen bonded to at least one non-water functional group with an affinity that is comparable to the affinity that water has for itself. Although a seemingly easy definition because the H-bond energy between waters is well characterised (roughly 4.2kj/mol) and thus any H-bond energy above this should preferentially bind water. It is not clear, however, whether having a nominal affinity difference between binding energies of bound and bulk water makes a significant difference [124,125] or if its removal has any structural influence. Higher energy

hydrogen bonding, known as low barrier hydrogen bonds (LBHB), typically have a much higher binding energy than interactions with polar functional groups and usually only occur around solvated ionic compounds like proteoglycans or charged mineral surfaces. In this case, surrounding ionic species, the LBHB binding energy may increase to 20-fold or higher than the energy of a typical H-bond [126]. These much higher energy H-bonds between water and a substrate are typically critical structural features that stabilize key catalytic or functional centers. Ultimately despite these possible theoretical thresholds for what constitutes strongly bound or weakly bound water, this binding affinity, even with comprehensive models for water sorption, may not translate directly to predictable measurements in experimental settings.

Consider for example the TGA experiment (Figure 4.2-1) where there appeared to exist a two-phase desorption of water from the pre-dried corneas as a function of hydration. These findings suggest that there are two distinct bound fractions in the cornea – one that corresponds to LBHB (17.266 kCal/mol – suggesting a delocalized proton [127]) and one that corresponds to a moderate strength H-bond (1.801kCal/mol). However, there is currently no experimental protocol that we know of that is capable of simultaneously inferring both the bonding energy and localisation of these bonding species within the tissue architecture.

Ultimately, as this field matures, it would be advisable to develop a nomenclature for various strength water interactions within living systems. In so doing, in the future, it will be easier to parse apart their contributions to the form and functions of connective tissues and hydrated biological structures more broadly.

7 BIBLIOGRAPHY

(1) Reznikov, N.; Shahar, R.; Weiner, S. Bone Hierarchical Structure in Three Dimensions. *Acta Biomaterialia* **2014**, *10* (9), 3815–3826. https://doi.org/10.1016/j.actbio.2014.05.024.

(2) Haq, F.; Ahmed, N.; Qasim, M. Comparative Genomic Analysis of Collagen Gene Diversity. *3 Biotech* **2019**, *9* (3), 83. https://doi.org/10.1007/s13205-019-1616-9.

(3) Bella, J.; Hulmes, D. J. S. Fibrillar Collagens. In *Fibrous Proteins: Structures and Mechanisms*; Parry, D. A. D., Squire, J. M., Eds.; Subcellular Biochemistry; Springer International Publishing: Cham, 2017; pp 457–490. https://doi.org/10.1007/978-3-319-49674-0_14.

(4) Birk, D. E. Type V Collagen: Heterotypic Type I/V Collagen Interactions in the Regulation of Fibril Assembly. *Micron* **2001**, *32* (3), 223–237. https://doi.org/10.1016/S0968-4328(00)00043-3.

(5) Scott, J. E. Proteoglycan-Fibrillar Collagen Interactions. *Biochem J* **1988**, *252* (2), 313–323.

(6) Scott, J. E.; Bosworth, T. R. A Comparative Biochemical and Ultrastructural Study of Proteoglycan–Collagen Interactions in Corneal Stroma. Functional and Metabolic Implications. *Biochemical Journal* **1990**, *270* (2), 491–497. https://doi.org/10.1042/bj2700491.

(7) Scott, J. E.; Haigh, M. 'Small'-Proteoglycan: Collagen Interactions: Keratan Sulphate Proteoglycan Associates with Rabbit Corneal Collagen Fibrils at the 'a' and 'c' Bands. *Biosci Rep* **1985**, *5* (9), 765–774. https://doi.org/10.1007/BF01119875.

(8) Reznikov, N.; Hoac, B.; Buss, D. J.; Addison, W. N.; Barros, N. M. T.; McKee, M. D. Biological Stenciling of Mineralization in the Skeleton: Local Enzymatic Removal of Inhibitors in the Extracellular Matrix. *Bone* **2020**, *138*, 115447. https://doi.org/10.1016/j.bone.2020.115447.

(9) Bettelheim, F. A.; Plessy, B. The Hydration of Proteoglycans of Bovine Cornea. *Biochimica et Biophysica Acta (BBA) - General Subjects* **1975**, *381* (1), 203–214. https://doi.org/10.1016/0304-4165(75)90202-0.

(10) Bertassoni, L. E.; Swain, M. V. The Contribution of Proteoglycans to the Mechanical Behavior of Mineralized Tissues. *Journal of the Mechanical Behavior of Biomedical Materials* **2014**, *38*, 91–104. https://doi.org/10.1016/j.jmbbm.2014.06.008.

(11) Edelhauser, H. F. The Balance between Corneal Transparency and Edema The Proctor Lecture. *Investigative Ophthalmology & Visual Science* **2006**, *47* (5), 1755–1767. https://doi.org/10.1167/iovs.05-1139.

(12) Young, R. D.; Knupp, C.; Pinali, C.; Png, K. M. Y.; Ralphs, J. R.; Bushby, A. J.; Starborg, T.; Kadler, K. E.; Quantock, A. J. Three-Dimensional Aspects of Matrix Assembly by Cells in the Developing Cornea. *Proceedings of the National Academy of Sciences* **2014**, *111* (2), 687–692. https://doi.org/10.1073/pnas.1313561110.

(13) Meek, K. M. Corneal Collagen—Its Role in Maintaining Corneal Shape and Transparency. *Biophys Rev* **2009**, *1* (2), 83–93. https://doi.org/10.1007/s12551-009-0011-x.

(14) Ottani, V.; Martini, D.; Franchi, M.; Ruggeri, A.; Raspanti, M. Hierarchical Structures in Fibrillar Collagens. *Micron* **2002**, *33* (7), 587–596. https://doi.org/10.1016/S0968-4328(02)00033-1.

(15) Meek, K. M.; Knupp, C. Corneal Structure and Transparency. *Prog Retin Eye Res* **2015**, *49*, 1–16. https://doi.org/10.1016/j.preteyeres.2015.07.001.

(16) Peixoto, P. D. S.; Deniset-Besseau, A.; Schanne-Klein, M.-C.; Mosser, G. Quantitative Assessment of Collagen I Liquid Crystal Organizations: Role of Ionic Force and Acidic

Solvent, and Evidence of New Phases. *Soft Matter* **2011**, *7* (23), 11203–11210. https://doi.org/10.1039/C1SM06076G.
(17) De Sa Peixoto, P.; Deniset-Besseau, A.; Schmutz, M.; Anglo, A.; Illoul, C.; Schanne-Klein, M.-C.; Mosser, G. Achievement of Cornea-like Organizations in Dense Collagen I Solutions: Clues to the Physico-Chemistry of Cornea Morphogenesis. *Soft Matter* **2013**, *9* (47), 11241. https://doi.org/10.1039/c3sm52097h.
(18) Young, R. D.; Knupp, C.; Koudouna, E.; Ralphs, J. R.; Ma, Y.; Lwigale, P. Y.; Jester, J. V.; Quantock, A. J. Cell-Independent Matrix Configuration in Early Corneal Development. *Experimental Eye Research* **2019**, *187*, 107772. https://doi.org/10.1016/j.exer.2019.107772.
(19) Sibillano, T.; De Caro, L.; Scattarella, F.; Scarcelli, G.; Siliqi, D.; Altamura, D.; Liebi, M.; Ladisa, M.; Bunk, O.; Giannini, C. Interfibrillar Packing of Bovine Cornea by Table-Top and Synchrotron Scanning SAXS Microscopy. *Journal of Applied Crystallography* **2016**, *49* (4), 1231–1239. https://doi.org/10.1107/S1600576716010396.
(20) Meek, K. M.; Fullwood, N. J.; Cooke, P. H.; Elliott, G. F.; Maurice, D. M.; Quantock, A. J.; Wall, R. S.; Worthington, C. R. Synchrotron X-Ray Diffraction Studies of the Cornea, with Implications for Stromal Hydration. *Biophysical Journal* **1991**, *60* (2), 467–474. https://doi.org/10.1016/S0006-3495(91)82073-2.
(21) Meek, K. M.; Quantock, A. J.; Hayes, S.; Bell, J. X-Ray Diffraction Imaging of Corneal Ultrastructure. In *Corneal Regeneration: Methods and Protocols*; Ahearne, M., Ed.; Methods in Molecular Biology; Springer US: New York, NY, 2020; pp 231–247. https://doi.org/10.1007/978-1-0716-0599-8_16.
(22) Mak, K. M.; Png, C. Y. M.; Lee, D. J. Type V Collagen in Health, Disease, and Fibrosis. *The Anatomical Record* **2016**, *299* (5), 613–629. https://doi.org/10.1002/ar.23330.
(23) Holmes, D. F.; Gilpin, C. J.; Baldock, C.; Ziese, U.; Koster, A. J.; Kadler, K. E. Corneal Collagen Fibril Structure in Three Dimensions: Structural Insights into Fibril Assembly, Mechanical Properties, and Tissue Organization. *Proceedings of the National Academy of Sciences* **2001**, *98* (13), 7307–7312. https://doi.org/10.1073/pnas.111150598.
(24) Buss, D. J.; Kröger, R.; McKee, M. D.; Reznikov, N. Hierarchical Organization of Bone in Three Dimensions: A Twist of Twists. *Journal of Structural Biology: X* **2022**, *6*, 100057. https://doi.org/10.1016/j.yjsbx.2021.100057.
(25) Bonanno, J. A. "Molecular Mechanisms Underlying the Corneal Endothelial Pump." *Exp Eye Res* **2012**, *95* (1), 2–7. https://doi.org/10.1016/j.exer.2011.06.004.
(26) Fischbarg, J.; Lim, J. J. Role of Cations, Anions and Carbonic Anhydrase in Fluid Transport across Rabbit Corneal Endothelium. *The Journal of Physiology* **1974**, *241* (3), 647–675. https://doi.org/10.1113/jphysiol.1974.sp010676.
(27) Meek, K. M.; Leonard, D. W.; Connon, C. J.; Dennis, S.; Khan, S. Transparency, Swelling and Scarring in the Corneal Stroma. *Eye* **2003**, *17* (8), 927–936. https://doi.org/10.1038/sj.eye.6700574.
(28) Misson, G. P.; Stevens, J. D. Stress Birefringence in the Human Cornea. *Eye* **1990**, *4* (6), 830–834. https://doi.org/10.1038/eye.1990.131.
(29) Scott, J. E.; Thomlinson, A. M. The Structure of Interfibrillar Proteoglycan Bridges ('Shape Modules') in Extracellular Matrix of Fibrous Connective Tissues and Their Stability in Various Chemical Environments. *The Journal of Anatomy* **1998**, *192* (3), 391–405. https://doi.org/10.1046/j.1469-7580.1998.19230391.x.
(30) Lewis, P. N.; Pinali, C.; Young, R. D.; Meek, K. M.; Quantock, A. J.; Knupp, C. Structural Interactions between Collagen and Proteoglycans Are Elucidated by Three-

Dimensional Electron Tomography of Bovine Cornea. *Structure* **2010**, *18* (2), 239–245. https://doi.org/10.1016/j.str.2009.11.013.
(31) Huang, Y.; Meek, K. M. Swelling Studies on the Cornea and Sclera: The Effects of PH and Ionic Strength. *Biophysical Journal* **1999**, *77* (3), 1655–1665. https://doi.org/10.1016/S0006-3495(99)77013-X.
(32) Maurice, D. M. The Location of the Fluid Pump in the Cornea. *The Journal of Physiology* **1972**, *221* (1), 43–54. https://doi.org/10.1113/jphysiol.1972.sp009737.
(33) Alkanaan, A.; Barsotti, R.; Kirat, O.; Khan, A.; Almubrad, T.; Akhtar, S. Collagen Fibrils and Proteoglycans of Peripheral and Central Stroma of the Keratoconus Cornea - Ultrastructure and 3D Transmission Electron Tomography. *Sci Rep* **2019**, *9* (1), 19963. https://doi.org/10.1038/s41598-019-56529-1.
(34) Seiler, T.; Trahms, L.; Wollensak, J. The Distinction of Corneal Water in Free and Bound Fractions. 3.
(35) O'Neill, H.; Pingali, S. V.; Petridis, L.; He, J.; Mamontov, E.; Hong, L.; Urban, V.; Evans, B.; Langan, P.; Smith, J. C.; Davison, B. H. Dynamics of Water Bound to Crystalline Cellulose. *Sci Rep* **2017**, *7* (1), 11840. https://doi.org/10.1038/s41598-017-12035-w.
(36) DeMali, K. A.; Williams, T. R. Determination of the Content of Water in Bovine Corneas by Differential Scanning Calorimetry and Thermogravimetric Analysis. *ORE* **1994**, *26* (2), 105–109. https://doi.org/10.1159/000267399.
(37) Inamdar, S. R.; Prévost, S.; Terrill, N. J.; Knight, M. M.; Gupta, H. S. Reversible Changes in the 3D Collagen Fibril Architecture during Cyclic Loading of Healthy and Degraded Cartilage. *Acta Biomaterialia* **2021**, *136*, 314–326. https://doi.org/10.1016/j.actbio.2021.09.037.
(38) Coleman, D. J.; Trokel, S. Direct-Recorded Intraocular Pressure Variations in a Human Subject. *Archives of Ophthalmology* **1969**, *82* (5), 637–640. https://doi.org/10.1001/archopht.1969.00990020633011.
(39) Henstock, J. R.; Rotherham, M.; Rose, J. B.; El Haj, A. J. Cyclic Hydrostatic Pressure Stimulates Enhanced Bone Development in the Foetal Chick Femur in Vitro. *Bone* **2013**, *53* (2), 468–477. https://doi.org/10.1016/j.bone.2013.01.010.
(40) Reznikov, N.; Bilton, M.; Lari, L.; Stevens, M. M.; Kröger, R. Fractal-like Hierarchical Organization of Bone Begins at the Nanoscale. *Science* **2018**, *360* (6388). https://doi.org/10.1126/science.aao2189.
(41) Brock, G. R.; Chen, J. T.; Ingraffea, A. R.; MacLeay, J.; Pluhar, G. E.; Boskey, A. L.; van der Meulen, M. C. H. The Effect of Osteoporosis Treatments on Fatigue Properties of Cortical Bone Tissue. *Bone Reports* **2015**, *2*, 8–13. https://doi.org/10.1016/j.bonr.2014.10.004.
(42) Kohandel, M.; Sivaloganathan, S.; Tenti, G. Estimation of the Quasi-Linear Viscoelastic Parameters Using a Genetic Algorithm. *Mathematical and Computer Modelling* **2008**, *47* (3), 266–270. https://doi.org/10.1016/j.mcm.2007.04.006.
(43) Abramowitch, S. D.; Woo, S. L.-Y. An Improved Method to Analyze the Stress Relaxation of Ligaments Following a Finite Ramp Time Based on the Quasi-Linear Viscoelastic Theory. *Journal of Biomechanical Engineering* **2004**, *126* (1), 92–97. https://doi.org/10.1115/1.1645528.
(44) Van Oss, C. J. *Interfacial Forces in Aqueous Media*, 2nd ed.; Taylor & Francis: Boca Raton, Fla., 2006.

(45) Leikin, S.; Rau, D. C.; Parsegian, V. A. Temperature-Favoured Assembly of Collagen Is Driven by Hydrophilic Not Hydrophobic Interactions. *Nat Struct Mol Biol* **1995**, *2* (3), 205–210. https://doi.org/10.1038/nsb0395-205.
(46) Meek, K. M.; Leonard, D. W. Ultrastructure of the Corneal Stroma: A Comparative Study. *Biophysical Journal* **1993**, *64* (1), 273–280. https://doi.org/10.1016/S0006-3495(93)81364-X.
(47) Quantock, A. J.; Meek, K. M.; Ridgway, A. E. A.; Bron, A. J.; Thonar, E. J.-M. A. Macular Corneal Dystrophy: Reduction in Both Corneal Thickness and Collagen Interfibrillar Spacing. *Current Eye Research* **1990**, *9* (4), 393–398. https://doi.org/10.3109/02713689008999628.
(48) Hayes, S.; White, T.; Boote, C.; Kamma-Lorger, C. S.; Bell, J.; Sorenson, T.; Terrill, N.; Shebanova, O.; Meek, K. M. The Structural Response of the Cornea to Changes in Stromal Hydration. *Journal of The Royal Society Interface* **2017**, *14* (131), 20170062. https://doi.org/10.1098/rsif.2017.0062.
(49) Gendron, R. L.; Armstrong, E.; Paradis, H.; Haines, L.; Desjardins, M.; Short, C. E.; Clow, K. A.; Driedzic, W. R. Osmotic Pressure-Adaptive Responses in the Eye Tissues of Rainbow Smelt (Osmerus Mordax). *Mol Vis* **2011**, *17*, 2596–2604.
(50) Knupp, C.; Pinali, C.; Lewis, P. N.; Parfitt, G. J.; Young, R. D.; Meek, K. M.; Quantock, A. J. The Architecture of the Cornea and Structural Basis of Its Transparency. In *Advances in Protein Chemistry and Structural Biology*; McPherson, A., Ed.; Advances in Protein Chemistry and Structural Biology; Academic Press, 2009; Vol. 78, pp 25–49. https://doi.org/10.1016/S1876-1623(08)78002-7.
(51) Aliev, A. E.; Courtier-Murias, D. Water Scaffolding in Collagen: Implications on Protein Dynamics as Revealed by Solid-State NMR. *Biopolymers* **2014**, *101* (3), 246–256. https://doi.org/10.1002/bip.22330.
(52) Ben-Naim, A. *Molecular Theory of Water and Aqueous Solutions: Part II: The Role of Water in Protein Folding, Self-Assembly and Molecular Recognition*; World Scientific Publishing Company, 2011. https://doi.org/10.1142/8154.
(53) Nakasako, M. Water–Protein Interactions from High–Resolution Protein Crystallography. *Phil. Trans. R. Soc. Lond. B* **2004**, *359* (1448), 1191–1206. https://doi.org/10.1098/rstb.2004.1498.
(54) Smith, J. C.; Merzel, F.; Bondar, A.-N.; Tournier, A.; Fischer, S. Structure, Dynamics and Reactions of Protein Hydration Water. *Philos Trans R Soc Lond B Biol Sci* **2004**, *359* (1448), 1181–1190. https://doi.org/10.1098/rstb.2004.1497.
(55) Leikin, S.; Parsegian, V. A.; Yang, W.-H.; Walrafen, G. E. Raman Spectral Evidence for Hydration Forces between Collagen Triple Helices. *Proceedings of the National Academy of Sciences* **1997**, *94* (21), 11312–11317. https://doi.org/10.1073/pnas.94.21.11312.
(56) Masic, A.; Bertinetti, L.; Schuetz, R.; Chang, S.-W.; Metzger, T. H.; Buehler, M. J.; Fratzl, P. Osmotic Pressure Induced Tensile Forces in Tendon Collagen. *Nat Commun* **2015**, *6* (1), 5942. https://doi.org/10.1038/ncomms6942.
(57) Fratzl, P.; Daxer, A. Structural Transformation of Collagen Fibrils in Corneal Stroma during Drying. An x-Ray Scattering Study. *Biophysical Journal* **1993**, *64* (4), 1210–1214. https://doi.org/10.1016/S0006-3495(93)81487-5.
(58) Fullerton, G. D.; Amurao, M. R. Evidence That Collagen and Tendon Have Monolayer Water Coverage in the Native State. *Cell Biology International* **2006**, *30* (1), 56–65. https://doi.org/10.1016/j.cellbi.2005.09.008.

(59) Leikin, S.; Kornyshev, A. A. Mean-Field Theory of Dehydration Transitions. *Phys. Rev. A* **1991**, *44* (2), 1156–1168. https://doi.org/10.1103/PhysRevA.44.1156.
(60) Masic, A.; Bertinetti, L.; Schuetz, R.; Galvis, L.; Timofeeva, N.; Dunlop, J. W. C.; Seto, J.; Hartmann, M. A.; Fratzl, P. Observations of Multiscale, Stress-Induced Changes of Collagen Orientation in Tendon by Polarized Raman Spectroscopy. *Biomacromolecules* **2011**, *12* (11), 3989–3996. https://doi.org/10.1021/bm201008b.
(61) Vesentini, S.; Redaelli, A.; Gautieri, A. Nanomechanics of Collagen Microfibrils. *Muscles Ligaments Tendons J* **2013**, *3* (1), 23–34. https://doi.org/10.11138/mltj/2013.3.1.023.
(62) Harley, R.; James, D.; Miller, A.; White, J. W. Phonons and the Elastic Moduli of Collagen and Muscle. *Nature* **1977**, *267* (5608), 285–287. https://doi.org/10.1038/267285a0.
(63) Sasaki, N.; Odajima, S. Stress-Strain Curve and Young's Modulus of a Collagen Molecule as Determined by the X-Ray Diffraction Technique. *Journal of Biomechanics* **1996**, *29* (5), 655–658. https://doi.org/10.1016/0021-9290(95)00110-7.
(64) Sibillano, T.; De Caro, L.; Altamura, D.; Siliqi, D.; Ramella, M.; Boccafoschi, F.; Ciasca, G.; Campi, G.; Tirinato, L.; Di Fabrizio, E.; Giannini, C. An Optimized Table-Top Small-Angle X-Ray Scattering Set-up for the Nanoscale Structural Analysis of Soft Matter. *Sci Rep* **2014**, *4* (1), 6985. https://doi.org/10.1038/srep06985.
(65) Stigter, D. A Comparison of Manning's Polyelectrolyte Theory with the Cylindrical Gouy Model. *J. Phys. Chem.* **1978**, *82* (14), 1603–1606. https://doi.org/10.1021/j100503a006.
(66) Zavitsas, A. A. Some Opinions of an Innocent Bystander Regarding the Hofmeister Series. *Current Opinion in Colloid & Interface Science* **2016**, *23*, 72–81. https://doi.org/10.1016/j.cocis.2016.06.012.
(67) Vyas, S.; Pradhan, S. D.; Pavaskar, N. R.; Lachke, A. Differential Thermal and Thermogravimetric Analyses of Bound Water Content in Cellulosic Substrates and Its Significance During Cellulose Hydrolysis by Alkaline Active Fungal Cellulases. *ABAB* **2004**, *118* (1–3), 177–188. https://doi.org/10.1385/ABAB:118:1-3:177.
(68) Cohen, S. R.; Polse, K. A.; Brand, R. J.; Bonanno, J. A. Stromal Acidosis Affects Corneal Hydration Control. *Investigative Ophthalmology & Visual Science* **1992**, *33* (1), 134–142.
(69) Milazzo, M.; David, A.; Jung, G. S.; Danti, S.; Buehler, M. J. Molecular Origin of Viscoelasticity in Mineralized Collagen Fibrils. *Biomater Sci 9* (9), 3390–3400. https://doi.org/10.1039/d0bm02003f.
(70) Bertinetti, L.; Masic, A.; Schuetz, R.; Barbetta, A.; Seidt, B.; Wagermaier, W.; Fratzl, P. Osmotically Driven Tensile Stress in Collagen-Based Mineralized Tissues. *Journal of the Mechanical Behavior of Biomedical Materials* **2015**, *52*, 14–21. https://doi.org/10.1016/j.jmbbm.2015.03.010.
(71) Muller, L.; Pels, E.; Vrensen, G. The Specific Architecture of the Anterior Stroma Accounts for Maintenance of Corneal Curvature. *Br J Ophthalmol* **2001**, *85* (4), 437–443. https://doi.org/10.1136/bjo.85.4.437.
(72) Koudouna, E.; Winkler, M.; Mikula, E.; Juhasz, T.; Brown, D. J.; Jester, J. V. Evolution of the Vertebrate Corneal Stroma. *Prog Retin Eye Res* **2018**, *64*, 65–76. https://doi.org/10.1016/j.preteyeres.2018.01.002.
(73) Winkler, M.; Shoa, G.; Tran, S. T.; Xie, Y.; Thomasy, S.; Raghunathan, V. K.; Murphy, C.; Brown, D. J.; Jester, J. V. A Comparative Study of Vertebrate Corneal Structure: The

Evolution of a Refractive Lens. *Investigative Ophthalmology & Visual Science* **2015**, *56* (4), 2764–2772. https://doi.org/10.1167/iovs.15-16584.
(74) Lee, S.-L.; He, M.-Y.; Chen, Y.-F.; Dong, C.-Y. Quantification of Collagen Structural Changes during Chick Corneal Development. *Journal of Biophotonics* **2020**, *13* (1), e201900144. https://doi.org/10.1002/jbio.201900144.
(75) Leroy, P.; Maineult, A. Exploring the Electrical Potential inside Cylinders beyond the Debye-Hückel Approximation: A Computer Code to Solve the Poisson-Boltzmann Equation for Multivalent Electrolytes. *Geophysical Journal International* **2018**. https://doi.org/10.1093/gji/ggy124.
(76) Dorvee, J. R.; Veis, A. Water in the Formation of Biogenic Minerals: Peeling Away the Hydration Layers. *Journal of Structural Biology* **2013**, *183* (2), 278–303. https://doi.org/10.1016/j.jsb.2013.06.007.
(77) Ben-Naim, A. *Statistical Thermodynamics for Chemists and Biochemists*; Springer US: Boston, MA, 1992. https://doi.org/10.1007/978-1-4757-1598-9.
(78) Corti, H. R.; Appignanesi, G. A.; Barbosa, M. C.; Bordin, J. R.; Calero, C.; Camisasca, G.; Elola, M. D.; Franzese, G.; Gallo, P.; Hassanali, A.; Huang, K.; Laria, D.; Menéndez, C. A.; de Oca, J. M. M.; Longinotti, M. P.; Rodriguez, J.; Rovere, M.; Scherlis, D.; Szleifer, I. Structure and Dynamics of Nanoconfined Water and Aqueous Solutions. *Eur. Phys. J. E* **2021**, *44* (11), 136. https://doi.org/10.1140/epje/s10189-021-00136-4.
(79) Ben-Naim, A. Strong Forces between Hydrophilic Macromolecules: Implications in Biological Systems. *The Journal of Chemical Physics* **1990**, *93* (11), 8196–8210. https://doi.org/10.1063/1.459298.
(80) Gautieri, A.; Pate, M. I.; Vesentini, S.; Redaelli, A.; Buehler, M. J. Hydration and Distance Dependence of Intermolecular Shearing between Collagen Molecules in a Model Microfibril. *Journal of Biomechanics* **2012**, *45* (12), 2079–2083. https://doi.org/10.1016/j.jbiomech.2012.05.047.
(81) Bella, J.; Eaton, M.; Brodsky, B.; Berman, H. M. Crystal and Molecular Structure of a Collagen-Like Peptide at 1.9 Å Resolution. *Science* **1994**, *266* (5182), 75–81. https://doi.org/10.1126/science.7695699.
(82) Fullerton, G. D.; Kanal, K. M.; Cameron, I. L. Osmotically Unresponsive Water Fraction on Proteins: Non-Ideal Osmotic Pressure of Bovine Serum Albumin as a Function of PH and Salt Concentration. *Cell Biology International* **2006**, *30* (1), 86–92. https://doi.org/10.1016/j.cellbi.2005.11.001.
(83) Wess, T. J.; Orgel, J. P. Changes in Collagen Structure: Drying, Dehydrothermal Treatment and Relation to Long Term Deterioration. *Thermochimica Acta* **2000**, *365* (1), 119–128. https://doi.org/10.1016/S0040-6031(00)00619-5.
(84) van Oss, C. J.; Chaudhury, M. K.; Good, R. J. Monopolar Surfaces. *Advances in Colloid and Interface Science* **1987**, *28*, 35–64. https://doi.org/10.1016/0001-8686(87)80008-8.
(85) Yang, F.; Das, D.; Karunakaran, K.; Genin, G. M.; Thomopoulos, S.; Chasiotis, I. Nonlinear Time-Dependent Mechanical Behavior of Mammalian Collagen Fibrils. *Acta Biomaterialia* **2022**, S1742706122001362. https://doi.org/10.1016/j.actbio.2022.03.005.
(86) Kostyuk, O.; Nalovina, O.; Mubard, T. M.; Regini, J. W.; Meek, K. M.; Quantock, A. J.; Elliott, G. F.; Hodson, S. A. Transparency of the Bovine Corneal Stroma at Physiological Hydration and Its Dependence on Concentration of the Ambient Anion. *The Journal of Physiology* **2002**, *543* (2), 633–642. https://doi.org/10.1113/jphysiol.2002.021527.

(87) Bettelheim, F. A.; Popdimitrova, N. Hyaluronic Acid–a Syneretic Glycosaminoglycan. *Current Eye Research* **1992**, *11* (5), 411–419. https://doi.org/10.3109/02713689209001794.
(88) van der Kooij, H. M.; Fokkink, R.; van der Gucht, J.; Sprakel, J. Quantitative Imaging of Heterogeneous Dynamics in Drying and Aging Paints. *Sci Rep* **2016**, *6* (1), 34383. https://doi.org/10.1038/srep34383.
(89) Kooij, H. M. van der; Kerkhof, G. T. van de; Sprakel, J. A Mechanistic View of Drying Suspension Droplets. *Soft Matter* **2016**, *12* (11), 2858–2867. https://doi.org/10.1039/C5SM02406D.
(90) Cheng, X.; Pinsky, P. M. Mechanisms of Self-Organization for the Collagen Fibril Lattice in the Human Cornea. *Journal of The Royal Society Interface* **2013**, *10* (87), 20130512. https://doi.org/10.1098/rsif.2013.0512.
(91) Ashofteh Yazdi, A.; Melchor, J.; Torres, J.; Faris, I.; Callejas, A.; Gonzalez-Andrades, M.; Rus, G. Characterization of Non-Linear Mechanical Behavior of the Cornea. *Sci Rep* **2020**, *10* (1), 11549. https://doi.org/10.1038/s41598-020-68391-7.
(92) Hatami-Marbini, H.; Etebu, E. Rate Dependent Biomechanical Properties of Corneal Stroma in Unconfined Compression. *Biorheology* **2013**, *50* (3–4), 133–147. https://doi.org/10.3233/BIR-130634.
(93) Hatami-Marbini, H.; Etebu, E. An Experimental and Theoretical Analysis of Unconfined Compression of Corneal Stroma. *Journal of Biomechanics* **2013**, *46* (10), 1752–1758. https://doi.org/10.1016/j.jbiomech.2013.03.013.
(94) Doughty, M. J. Re-Assessment of the Potential Impact of Physiologically Relevant PH Changes on the Hydration Properties of the Isolated Mammalian Corneal Stroma. *Biochimica et Biophysica Acta (BBA) - General Subjects* **1999**, *1472* (1), 99–106. https://doi.org/10.1016/S0304-4165(99)00109-9.
(95) Guéron, M.; Weisbuch, G. Polyelectrolyte Theory. I. Counterion Accumulation, Site-Binding, and Their Insensitivity to Polyelectrolyte Shape in Solutions Containing Finite Salt Concentrations. *Biopolymers* **1980**, *19* (2), 353–382. https://doi.org/10.1002/bip.1980.360190212.
(96) Quantock, A. J.; Winkler, M.; Parfitt, G. J.; Young, R. D.; Brown, D. J.; Boote, C.; Jester, J. V. From Nano to Macro: Studying the Hierarchical Structure of the Corneal Extracellular Matrix. *Experimental Eye Research* **2015**, *133*, 81–99. https://doi.org/10.1016/j.exer.2014.07.018.
(97) Komai, Y.; Ushiki, T. The Three-Dimensional Organization of Collagen Fibrils in the Human Cornea and Sclera. *Investigative Ophthalmology & Visual Science* **1991**, *32* (8), 2244–2258.
(98) Akhtar, S.; Petrovski, G.; Albert, R.; Alkanaan, A.; Kirat, O.; Khan, A. D.; Almubrad, T. Ultrastructure and 3D Transmission Electron Tomography of Collagen Fibrils and Proteoglycans of Swollen Human Corneal Stroma. *Histol Histopathol* **2019**, *34* (1), 91–102. https://doi.org/10.14670/HH-18-029.
(99) Reznikov, N.; Almany-Magal, R.; Shahar, R.; Weiner, S. Three-Dimensional Imaging of Collagen Fibril Organization in Rat Circumferential Lamellar Bone Using a Dual Beam Electron Microscope Reveals Ordered and Disordered Sub-Lamellar Structures. *Bone* **2013**, *52* (2), 676–683. https://doi.org/10.1016/j.bone.2012.10.034.
(100) Reznikov, N.; Shahar, R.; Weiner, S. Three-Dimensional Structure of Human Lamellar Bone: The Presence of Two Different Materials and New Insights into the Hierarchical Organization. *Bone* **2014**, *59*, 93–104. https://doi.org/10.1016/j.bone.2013.10.023.

(101) Bell, L. C.; Mika, H. THE PH DEPENDENCE OF THE SURFACE CONCENTRATIONS OF CALCIUM AND PHOSPHORUS ON HYDROXYAPATITE IN AQUEOUS SolUTIONS. *Journal of Soil Science* **1979**, *30* (2), 247–258. https://doi.org/10.1111/j.1365-2389.1979.tb00982.x.
(102) Bell, L. C.; Posner, A. M.; Quirk, J. P. Surface Charge Characteristics of Hydroxyapatite and Fluorapatite. *Nature* **1972**, *239* (5374), 515–517. https://doi.org/10.1038/239515a0.
(103) Itoh, D.; Yoshimoto, N.; Yamamoto, S. Retention Mechanism of Proteins in Hydroxyapatite Chromatography – Multimodal Interaction Based Protein Separations: A Model Study. *Curr Protein Pept Sci* **2018**, *20* (1), 75–81. https://doi.org/10.2174/1389203718666171024122106.
(104) Kendall, C.; Eriksen, A. M. H.; Kontopoulos, I.; Collins, M. J.; Turner-Walker, G. Diagenesis of Archaeological Bone and Tooth. *Palaeogeography, Palaeoclimatology, Palaeoecology* **2018**, *491*, 21–37. https://doi.org/10.1016/j.palaeo.2017.11.041.
(105) Buffrénil, V. de. *Vertebrate Skeletal Histology and Paleohistology*, First editon.; CRC Press, Taylor & Francis Group: Boca Raton, FL, 2021.
(106) Jans, M. M. E. Microbial Bioerosion of Bone – a Review. In *Current Developments in Bioerosion*; Wisshak, M., Tapanila, L., Eds.; Erlangen Earth Conference Series; Springer: Berlin, Heidelberg, 2008; pp 397–413. https://doi.org/10.1007/978-3-540-77598-0_20.
(107) Jackes, M.; Sherburne, R.; Lubell, D.; Barker, C.; Wayman, M. Destruction of Microstructure in Archaeological Bone: A Case Study from Portugal. *International Journal of Osteoarchaeology* **2001**, *11* (6), 415–432. https://doi.org/10.1002/oa.583.
(108) Turner–Walker, G.; Syversen, U. Quantifying Histological Changes in Archaeological Bones Using BSE–SEM Image Analysis. *Archaeometry* **2002**, *44* (3), 461–468. https://doi.org/10.1111/1475-4754.t01-1-00078.
(109) Buss, D. J.; Reznikov, N.; McKee, M. D. Crossfibrillar Mineral Tessellation in Normal and Hyp Mouse Bone as Revealed by 3D FIB-SEM Microscopy. *Journal of Structural Biology* **2020**, *212* (2), 107603. https://doi.org/10.1016/j.jsb.2020.107603.
(110) McKee, M. D.; Buss, D. J.; Reznikov, N. Mineral Tessellation in Bone and the Stenciling Principle for Extracellular Matrix Mineralization. *Journal of Structural Biology* **2022**, *214* (1), 107823. https://doi.org/10.1016/j.jsb.2021.107823.
(111) Fantner, G. E.; Hassenkam, T.; Kindt, J. H.; Weaver, J. C.; Birkedal, H.; Pechenik, L.; Cutroni, J. A.; Cidade, G. A. G.; Stucky, G. D.; Morse, D. E.; Hansma, P. K. Sacrificial Bonds and Hidden Length Dissipate Energy as Mineralized Fibrils Separate during Bone Fracture. *Nature Mater* **2005**, *4* (8), 612–616. https://doi.org/10.1038/nmat1428.
(112) Walsh, W. R.; Guzelsu, N. Ion Concentration Effects on Bone Streaming Potentials and Zeta Potentials. *Biomaterials* **1993**, *14* (5), 331–336. https://doi.org/10.1016/0142-9612(93)90050-C.
(113) Wang, Y.; Von Euw, S.; Fernandes, F. M.; Cassaignon, S.; Selmane, M.; Laurent, G.; Pehau-Arnaudet, G.; Coelho, C.; Bonhomme-Coury, L.; Giraud-Guille, M.-M.; Babonneau, F.; Azaïs, T.; Nassif, N. Water-Mediated Structuring of Bone Apatite. *Nature Mater* **2013**, *12* (12), 1144–1153. https://doi.org/10.1038/nmat3787.
(114) Duer, M. J. The Contribution of Solid-State NMR Spectroscopy to Understanding Biomineralization: Atomic and Molecular Structure of Bone. *Journal of Magnetic Resonance* **2015**, *253*, 98–110. https://doi.org/10.1016/j.jmr.2014.12.011.
(115) Von Euw, S.; Chan-Chang, T.-H.-C.; Paquis, C.; Haye, B.; Pehau-Arnaudet, G.; Babonneau, F.; Azaïs, T.; Nassif, N. Organization of Bone Mineral: The Role of Mineral–

Water Interactions. *Geosciences* **2018**, *8* (12), 466. https://doi.org/10.3390/geosciences8120466.
(116) Stigter, D. Evaluation of the Counterion Condensation Theory of Polyelectrolytes. *Biophysical Journal* **1995**, *69* (2), 380–388. https://doi.org/10.1016/S0006-3495(95)79910-6.
(117) Israelachvili, J. N. *Intermolecular and Surface Forces*, 3rd ed.; Academic Press: [Place of publication not identified], 2015.
(118) Urbic, T. Ions Increase Strength of Hydrogen Bond in Water. *Chem Phys Lett* **2014**, *610–611*, 159–162. https://doi.org/10.1016/j.cplett.2014.06.054.
(119) Jiang, W.; Griffanti, G.; Tamimi, F.; McKee, M. D.; Nazhat, S. N. Multiscale Structural Evolution of Citrate-Triggered Intrafibrillar and Interfibrillar Mineralization in Dense Collagen Gels. *Journal of Structural Biology* **2020**, *212* (1), 107592. https://doi.org/10.1016/j.jsb.2020.107592.
(120) Li, Y.; Li, R.; Reid, D. G.; Lunn, J. T.; Müller, K. H.; Laurencin, D.; Bonhomme, C.; Ossa, E. A.; Sommerdijk, N. A. J. M.; Duer, M. J. Metabolic Acids Impact Bone Mineral Maturation. bioRxiv September 21, 2022, p 2022.09.21.508894. https://doi.org/10.1101/2022.09.21.508894.
(121) Hu, Y.-Y.; Rawal, A.; Schmidt-Rohr, K. Strongly Bound Citrate Stabilizes the Apatite Nanocrystals in Bone. *Proceedings of the National Academy of Sciences* **2010**, *107* (52), 22425–22429. https://doi.org/10.1073/pnas.1009219107.
(122) Peto, S.; Gillis, P.; Henri, V. P. Structure and Dynamics of Water in Tendon from NMR Relaxation Measurements. *Biophysical Journal* **1990**, *57* (1), 71–84. https://doi.org/10.1016/S0006-3495(90)82508-X.
(123) Nguyen, T. T.; Happillon, T.; Feru, J.; Brassart-Passco, S.; Angiboust, J.-F.; Manfait, M.; Piot, O. Raman Comparison of Skin Dermis of Different Ages: Focus on Spectral Markers of Collagen Hydration. *Journal of Raman Spectroscopy* **2013**, *44* (9), 1230–1237. https://doi.org/10.1002/jrs.4355.
(124) Silverstein, K. A. T.; Haymet, A. D. J.; Dill, K. A. The Strength of Hydrogen Bonds in Liquid Water and Around Nonpolar Solutes. *J. Am. Chem. Soc.* **2000**, *122* (33), 8037–8041. https://doi.org/10.1021/ja000459t.
(125) Szalewicz, K. Hydrogen Bond. In *Encyclopedia of Physical Science and Technology (Third Edition)*; Meyers, R. A., Ed.; Academic Press: New York, 2003; pp 505–538. https://doi.org/10.1016/B0-12-227410-5/00322-7.
(126) Frey, P. A. Low Barrier Hydrogen Bonds. In *Encyclopedia of Biological Chemistry*; Lennarz, W. J., Lane, M. D., Eds.; Elsevier: New York, 2004; pp 594–598. https://doi.org/10.1016/B0-12-443710-9/00367-7.
(127) Kemp, M. T.; Lewandowski, E. M.; Chen, Y. Low Barrier Hydrogen Bonds in Protein Structure and Function. *Biochim Biophys Acta Proteins Proteom* **2021**, *1869* (1), 140557. https://doi.org/10.1016/j.bbapap.2020.140557.

8 APPENDIX

8.1 Appendix A: Supporting Figures

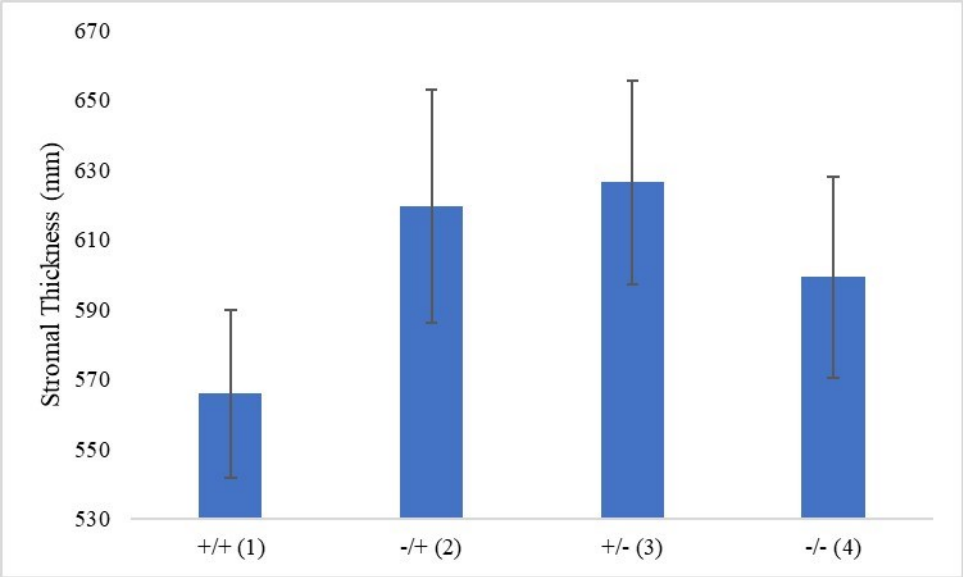

Figure 8.1-1: Corneal Thickness measurements with combined pH and Osmotic pressure changes. '+' indicates High treatment, '-' indicates Low treatment – (Osmolarity/pH).

8.2 Appendix B: Supporting Simulations and Model Code

8.2.1 Hierarchical coarse grained bound water model

8.2.1.1 Subfibrillar-Level

```
%Fractional bound water modelling in tissues
clc;clear;
%-------------------------------------------------------------------------
%% Tropocollagen Molecular level Hydration - 1st Principles
%.........................................................................
%Interaction Parameters for Polar (non-ionic) interactions
%London Forces
gc_lw = 38; %mj/m^2 - collagen
gw_lw = 21.8;%mj/m^2 - Water
%Polar (AB) forces
gw_pos = 25.5;%mj/m^2
gw_neg = 25.5;%mj/m^2
gc_neg = 27;%21.1;%mj/m^2 - Although another source gives like 30-38

%Free Energy balance calculation
dG_131_LW = -2*(sqrt(gc_lw)-sqrt(gw_lw))^2;
dG_131_AB = -4*(sqrt(gw_neg*gw_pos)-sqrt(gc_neg*gw_pos));
% Calculation in vacuo
dG_13 = -2*(sqrt(gc_lw*gw_lw)+sqrt(gc_neg*gw_pos));
```

```
lambda_w = 5.5E-10;%nm - Correlation Length of water
l_o = 1.4E-10; %Minimum equilibrium distance

%Calculation of decay forces - As parallel plates for now
% F_AB_prime = -(1/lambda_w)*dG_131;
lx = linspace(1.57E-10,40E-10,100);%Born repulsion of 1.4 A
% F_AB = F_AB_prime*exp((l_o-lx)/lambda_w);
% dG_AB = 2*pi*(12E-10)*lambda_w*dG_131_AB*exp((l_o-lx)/lambda_w);%For adjacent
cylinders or a flat plate and sphere
dG_AB = dG_131_AB*exp((l_o-lx)/lambda_w);%For adjacent cylinders or a flat plate and
sphere
dG_LW = dG_131_LW*(l_o./lx).^2;
% dG_tot = dG_LW+dG_AB;

debye = 8e-10;
eps = 80;%frad/meter
psi0 = 1; %volts
rcol = 7.5e-10;
dG_el = eps*psi0^2*rcol*log(1+exp(-(1/debye)*lx));
%calculate sas from col geometry
SAS = 1;%pi*(rcol^2)*300e-9;

E_ab = dG_AB*SAS;
E_el = dG_el*SAS;
E_LW = dG_LW*SAS;

%Something iffy is going on here
dG_tot = dG_LW+dG_AB+dG_el;
E_tot = E_LW+E_ab+E_el;

%plot example
plot(lx*1E10,E_ab);
hold on
plot(lx*1E10,E_LW);
hold on
plot(lx*1E10,E_el);
hold on
plot(lx*1E10,E_tot);


xlabel('L (A)')
ylabel('\Delta G_{AB} (mJ/m^2)')
%-------------------------------------------------------------------------


%% Calculation of intrafibrillar Hydration Quantity
%Eran Ittah
%McGill University
%Fractional bound water modelling in tissues
clc;clear;
%-------------------------------------------------------------------------
%% Calculation of Monolayer coverage surrounding Collagen Fibril
D_w = 3.15;%Angstrom (Hydrodynamic readius of H2O) - [1], Berendsen says 2.37A but
has a different zigzag model - [REF]
```

```
A_w = 8.59;%Angstrom^2 (Area occupancy) - [1]
V_w = (4/3)*pi*(3.14/2)^3;%

D_0 = 12;%angstrom (tropocol mol diam) - [1]
l_0 = 3000;%A (length of tropocollagen) - [1,3]
D_fib = 330;%Angstrom (Fibril diameter)

SAS_tot = 607416; %angstrom^2 (solvent accessible surface)

%No. of H2O per collagen molecule - linear model
k2 = 0.3834;% likely be calculated from values obtained by huang and meek 1999
nf = 2*D_w/(0.0877*k2*D_0);%Number of non-staggered circumferential H2O
nwl =l_0/D_w ;%number of waters per molecular length
nw_mol = nwl*nf;%total number of water molecules/molecule of tropocol

% No. of H2O per fibril
nmol_xsection = 300;%number of col molecules per fibril crossection [3];
nf_fibril = 300*nw_mol;%number of water molecules per fibril or 300nm length

%No. of monlayer water covering all fibrils in unit cell
nf_col_tot = nf_fibril;

D_mol_hydrated = nf*D_w/pi;%Diameter of hydrated tropocollagen (A)
D_fib_hydrated = 380;%Diameter of hydrated fibril (A)
V_fib_hydrated = ((pi/4)*D_fib_hydrated^2)*l_0;%A^3

%% calculation of hydrated fibrillar unit cell volume
%Total Area of triclinic lattice (2D)
V_uc =(sqrt(3)/2)*(520^2)*l_0; %A^3

%Sanity check for Unit cell facet area (3000 - 5500 nm^2)! - [4]
Vuc_nm = V_uc*(10^-3)/(l_0*0.1);%nm^2

%% Total bound water molecules in unit cell
NAv = 6.022214E23;
Mw_H2O = 18.06;%g/mol

BW_tot =nf_col_tot; %Total bound water (mol)
BW_tot_mass = Mw_H2O*((nf_col_tot)/NAv); %Total bound water (grams)
Vfree = V_uc;%V_uc-V_fib_hydrated-V_PG;
nf_tot = (Vfree)/V_w;
BW_frac = (BW_tot/nf_tot)*100;

%% Calculate Water by mass in tissue
y_bw = 0.555092978; %mol-H2O/g-HA
perc = 0.03;
rho = 1.062; %g/cm^3
mass_UC = (1.062)*V_uc*(10^(-24));%A^3?
mass_H2O_UC = (0.82*mass_UC/Mw_H2O)*NAv;

%% Print Results
fprintf("     n_H2O Col = %f molecules\n",nf_col_tot);
fprintf("     n_H2O tot = %f molecules\n",nf_tot);
fprintf("     ------------------------------------\n");
fprintf("     BW = %f %% ",BW_frac);
```

```
%% Refs
%-------------------------------------------------------------------------
%[1] Evidence that collagen and tendon have monolayer water coverage in the
%native state (Fullerton, 2005)[82]
%-------------------------------------------------------------------------
%[2] Transparency of the bovine corneal stroma at physiological hydration and its
dependence on concentration of the ambient anion (Kostyuk et Al., 2002)
%dehydration curves
%-------------------------------------------------------------------------
%[3] Corneal collagen—its role in maintaining corneal shape and
%transparency (Meek, 2009)
%-------------------------------------------------------------------------
%[4] Ultrastructure of the corneal stroma: a comparative study (Meek et Al., 1993)
%good info for bragg spacing and whatnot
%-------------------------------------------------------------------------
```

8.2.1.2 Fibril Level Electrostatics – Isolated Fibril

```
%% Modelling Fibril Level E-statics interactions
%Eran Ittah
%McGill University
clc;clear;
%-------------------------------------------------------------------------
%% Defining Variables
Dfibril = 33E-9;% 33nm- % Diameter of Fibril
e = -1.6E-19; % electronic charge (coloumb)
a = Dfibril/2;%Cylinder Radius
Rc = Dfibril;% 2*a
zeta = 2; %linear charge density in
Thickness = Rc/2*zeta;% Thickness
T = 293; %kelvin
kb = 1.380649E-23; %boltzmann const
psi0 = -10E-3;% Electrostatic potential - Get it
NAv = 6.022214E23;%mol^-1

%% Calculation of Debye Length (lambda)
% Cations
% [Na, K, Ca, Mg]
Cat_Val = [1, 1, 2, 2];
cCat = [60.9, 5.8,3.8,0.98]; %mM
niCat = (cCat*10^-3);%Says this should be in concentration.
sum_cats = sum(niCat.*(Cat_Val.^2));

% Anions
% [Cl, PO4,HCO3]
An_Val = [-1, -3, -1];
cAn = [36.3, 3.8, 28]; %mM
niAn = (cAn*10^-3);%Says this should be in concentration.
sum_ans = sum(niAn.*(An_Val.^2));

eps_0 = 8.85E-12;% Dielectric constant vaccum
D = 78;%dielec const. water
lb = e^2/(4*pi*eps_0*D*kb*T);%Bjerrum length of water - 0.72nm roughly
```

```
% Combine ionic quantities and calculate Debye letngth
sum_ions = (sum_ans+sum_cats);
lambda = 0.304/sqrt(sum_ions)*1E-9;%Debye Length

eps = a/(lambda);

%% Calculation of alpha
nm = sum(cCat(1,1:2),"all")*1E-3; %molar conc. of monovalent ions
nd = sum(cCat(3:end),"all")*1E-3;%molar conc. of divalent ions
alpha = 2*nd/(2*nd+nm);

%% radial span for calculation
r = a:0.1*a:10*a ; %Radial distance calculation
Xspan = 2*r/Rc;
xs2 = Xspan';

%% Optimization solver
xs0 = [psi0];
lb = [-1];
ub = [1];

ptimopts = optimoptions("fmincon","ConstraintTolerance",1e-6);
[psi_sol,fval] =
fmincon(@(psi)objectiveFun(psi,zeta,e,kb,T,Xspan,Rc,lambda,alpha),xs0,[],[],[],[],lb,
ub);

%Check performance
phi_0 = e*(psi0)/(kb*T);% We only know  that phi at inf is 0
dPhi_dX_i = -2*zeta; %Boundary condition 1
%%

[~,varSol] =
ode45(@(X,w)Poisson_Boltzmann(X,w,alpha,eps),Xspan,[phi_0,dPhi_dX_i],opts);

% plot(Xspan,varSol)

%% Convert between potential and Energy and plot results
r = (x*Dfibril/2)*1e9; %Radial Distance form surface
potentials = (phi*(kb*T)/e);
threshold = 13.3; %kcal/mol
thresh = ones(length(r),1)*threshold;
nChains = 4;
aleph = nChains*23.118e6; %Coulombs/mol - charge per mol
joul2kcal = 0.239;
Energy = (potentials*aleph*joul2kcal)*1e-3;

%plot this
plot(r, Energy)
hold on
plot(r,thresh)
ylabel('\epsilon (kCal/mol)')
xlabel('Distance from fibril surface (nm)')
```

```
%% Objective Function for solving Boundary conditions
function obj = objectiveFun(psi,zeta,e,kb,T,Xspan,Rc,lambda,alpha)
    phi_0 = e*psi/(kb*T);% We only know  that phi at inf is 0
    dPhi_dX_i = -2*zeta; %Boundary condition 1

    % opts = odeset('RelTol',1e-2,'AbsTol',1e-5);
    [~,varSol] =
ode45(@(X,w)Poisson_Boltzmann(X,w,alpha,eps),Xspan,[phi_0,dPhi_dX_i]);

    phi_data = varSol(:,1);

    if isnan(phi_data(end))
        val = 1000;
    end

    obj = ((abs(phi_data(end)) - (3*lambda + Rc)));

end


%% Poisson Boltzmann Equation
function dw_dX = Poisson_Boltzmann(X,w,alpha,eps)
    dw_dX = zeros(2,1);
    dw_dX(1) = ((eps^2)/(2+alpha))*(((1-alpha)*exp(w(2)))+(alpha*exp(2*w(2)))-exp(-
w(2)))-(w(1)/X);
    dw_dX(2) = w(1);
end
```

8.2.1.3 Fibril Level Electrostatics – ECM Geometry

```
%% Modellling Fibril Level E-statics interactions
%Eran Ittah
McGill University
clc;clear;
%--------------------------------------------------------------------------
%% Defining Variables
Dfibril = 28E-9;% 33nm- % Diameter of Fibril
e = -1.6E-19; % electronic charge (coloumb)
a = Dfibril/2;%Cylinder Radius
Rc = Dfibril;% 2*a
zeta = 2; %linear charge density in
Thickness = Rc/2*zeta;% Thickness
T = 293; %kelvin
kb = 1.380649E-23; %boltzmann const
psi0 = -50E-3;% Electrostatic potential - Get it
NAv = 6.022214E23;%mol^-1

%% Calculation of Debye Length (lambda)
% Cations
% [Na, K, Ca, Mg]
Cat_Val = [1, 1, 2, 2];
cCat = [60.9, 5.8,3.8,0.98]; %mM
niCat = (cCat*10^-3);%Says this should be in concentration.
```

```
sum_cats = sum(niCat.*(Cat_Val.^2));

% Anions
% [Cl, PO4,HCO3]
An_Val = [-1, -3, -1];
cAn = [36.3, 3.8, 28]; %mM
niAn = (cAn*10^-3);%Says this should be in concentration.
sum_ans = sum(niAn.*(An_Val.^2));

eps_0 = 8.85E-12;% Dielectric constant vaccum
D = 78;%dielec const. water
lb = e^2/(4*pi*eps_0*D*kb*T);%Bjerrum length of water - 0.72nm roughly

% Mix it all together
sum_ions = (sum_ans+sum_cats);
k = sqrt(((e^2)/(eps_0*kb*T))*sum_ions);
lambda = 0.304/sqrt(sum_ions)*1E-9;

eps = a/(lambda);

%% Calculation of alpha
nm = sum(cCat(1,1:2),"all")*1E-3; %molar conc. of monovalent ions
nd = sum(cCat(3:end),"all")*1E-3;%molar conc. of divalent ions
alpha = 2*nd/(2*nd+nm);

%% radial span for calculation
IFS = 8.8E-9;
r = linspace(a,a+IFS,100); %a:0.1*a:10*a ; %Radial distance calculation
Xspan = 2*r/Rc;
xs2 = Xspan';

%% Boundary Value Problem solver
%Check performance
phi_0 = e*(psi0)/(kb*T);% We only know  that phi at inf is 0
dPhi_dX_i = -2*zeta; %Boundary condition 1

solinit = bvpinit(Xspan, [1.186561722764219; 1.186561722764219]);

%Solve
sol =
bvp4c(@(X,w)Poisson_Boltzmann(X,w,alpha,eps),@(phi1,phi2)bcfun(phi1,phi2,phi_0,dPhi_d
X_i),solinit);


%% Plot Results of BVP
phi = sol.y(1,:)';
x = sol.x';

% plot(x,phi)

%% Convert to Energy and plot
r = (x*Dfibril/2)*1e9; %Radial Distance form surface
potentials = (phi*(kb*T)/e);
threshold = 13.3; %kcal/mol
thresh = ones(length(r),1)*threshold;
```

```
nChains = 4;
aleph = nChains*23.118e6; %Coulombs/mol - charge per mol
joul2kcal = 0.239;
Energy = (potentials*aleph*joul2kcal)*1e-3;
%plot this
plot(r, Energy)
hold on
plot(r,thresh)
ylabel('\epsilon (kCal/mol)')
xlabel('Distance from fibril surface (nm)')

%% Poisson Boltzmann Equation
function dw_dX = Poisson_Boltzmann(X,w,alpha,eps)
dw_dX = zeros(2,1);
dw_dX(1) = ((eps^2)/(2+alpha))*(((1-alpha)*exp(w(2)))+(alpha*exp(2*w(2)))-exp(-
w(2)))-(w(1)/X);
dw_dX(2) = w(1);
end

%% Boundary Condition function
function res = bcfun(phi_a,phi_b,phi0,~)
res = [phi_a(1) + phi0, phi_b(1)+ phi0];%phi_a(2), phi_b(2)
end
```

8.2.1.4 Fibril Bound Water Quantification

```
%% Bound Water Fibril Coat Sim
%Eran Ittah
%McGill University
%29.03.2023
clc;clear;
%-------------------------------------------------------------------------
%% Import H vs IFS Data from Text File
IFS_Data = readmatrix("MFW_vs_IFS.txt");
mass_Frac_Water = (unique(IFS_Data(:,1)));
IFS = unique(IFS_Data(:,2));

%Find min and max of range
minH = min(mass_Frac_Water);
maxH = max(mass_Frac_Water);

%Generat equally spaced point grid between extremes
eps = 0.01;
[fitobj,gof,output] = fit(mass_Frac_Water,IFS,'exp2');
hVal = linspace(0.001,0.999,100);

% IFSquery  = spline(mass_Frac_Water,IFS,hVal');
IFSquery = fitobj(hVal);
IFSquery2 = IFSquery.*1e-9;

for i = 1:length(IFSquery2)
    output = Fibrillar_Electrostatics_BVP_BW_29_03_2023(IFSquery2(i,1));
    op{i} =  output;
end
```

```
%% Compute BW thickness
for j=1:length(op)
    opmat = op{j};
    minE = min(opmat(:,2));
    if minE >= 13.3
        d(j) = abs(op(1,1)-op(end,1))/2;
    else
        bound = opmat(1,1);
        midpont = round(length(opmat)/2);
        yq = spline(opmat(1:midpont,2),opmat(1:midpont,1),13.3);
        d(j) = yq-bound;
    end
end

%% Plot bulk hydration vs shell thickness
plot(hVal',d')
xlabel("Mass Fraction Water in tissue")
ylabel("Thickness of Hydration Shell")

%% Convert Shell thickness to mass of water
D_fib = 28e-9;%diameter of fibril
V_Coat = (300e-9)*pi.*((d')*1e-9).^2;%Volume of hydrated coat (m^3)
V_fibril = 300e-9*(pi/4)*(D_fib)^2;
V_uc = (1.12*(IFSquery*1e-9).^2)*(300e-9);
V_ifm = V_uc - V_fibril;
V_frac_IFM = V_ifm./V_uc;
rhoCol = 1.23e3;rhoIFM = 1.06e3;
M_hydrated_UC = (V_frac_IFM.*rhoIFM + (1-V_frac_IFM).*rhoCol).*0.9.*V_uc;
M_hydrated_Coat = V_Coat.*rhoIFM;
Percent_BW_Fibrils = M_hydrated_Coat./M_hydrated_UC;
%%
plot(hVal',Percent_BW_Fibrils)
xlabel("Mass Fraction Water in tissue")
ylabel("Interfibrillar bound water fraction")
```

8.2.1.5 Interlamellar Boundary Potential Simulation

```
%% Finite element analysis of electrostatics with complex geometries
% Eran Ittah
%McGill University
clc;clear;
%-----------------------------------------------------------------
%% Generate appropriate model
%MATLAB has built-in FEM solver for elliptic problems

% Generate the model
eStatModel = createpde("electromagnetic","electrostatic");
Mesh = stlread("hexathingv2.STL");
scaledMesh = scale(Mesh,1e-8);

% Describe the geometry - this we will add ourselves
geo = importGeometry(eStatModel,scaledMesh);
%Display the geometry
pdegplot(eStatModel);
```

```
%% Define important parameters
% Permitivities
eStatModel.VacuumPermittivity = 8.8541878128E-12; %si units
electromagneticProperties(eStatModel,"RelativePermittivity",80);%relative permitivity
of water

%Define charge density - We want non-constant surface charge density
src = electromagneticSource(eStatModel,"ChargeDensity",1.536e-16);


%Boundary conditions - need to look this up further****
electromagneticBC(eStatModel,"Voltage",-40E-3,"Face",[4:25,28:49]);
electromagneticBC(eStatModel,"Voltage",0,"Face",[26,27]);%[1:3,26,27,50]

%generate the model mesh
scale(eStatModel.Geometry,1);
generateMesh(eStatModel);

%% solve it
eStatModel.SolverOptions.ReportStatistics = 'on';
eStatModel.SolverOptions.AbsoluteTolerance = 1e-9;
eStatModel.SolverOptions.MinStep = 1.5e-10;
eStatModel.SolverOptions.MaxIterations = 1000;
R = solve(eStatModel);
u = R.ElectricPotential;
%% Plot
pltpde = pdeplot3D(eStatModel,"ColorMapData",R.ElectricPotential);
```

8.2.2 QLV Model Fitting for Stress Relaxation

```
clc;clear;
%% Model Fitting with Prony Series
E_inf_0 =[0.2];
tau_0 =[0.5 0.5];
E_i_0 =[1 1];


Treatments = ["1.5%","2.5%","5%","7.5%","15%","20%"];
sz = 8;

for i = 1:length(Treatments)
    mat =
readmatrix("Thesis_Mechanical_Testing_28_03_2023.xlsx",Sheet=Treatments(i));
    data{i} = mat(:,2:9);
end

t = mat(:,1);

for k = 1:length(Treatments)
    for j = 1:8
    [xk{k,j},fval] =
fmincon(@(const)series(const,t,data{k}(:,j)),[E_inf_0,tau_0(1),E_i_0(1),tau_0(2),E_i_
0(2)],[],[],[],[],[0.01 0 0 0 0],[1 1000 1000 1000 1000]);
    end
```

```
end


%% Test it
for k=1:length(Treatments)
    for j= 1:8
        plot(t,data{k}(:,j),"Marker",".","MarkerSize",10)
        hold on
        valor = xk{k,j}(1)+xk{k,j}(3)*exp(-t/xk{k,j}(2)) + xk{k,j}(5)*exp(-
t/xk{k,j}(4));
        plot(t,valor)
        hold on
    end
end

xlabel("time (seconds)")
ylabel("G_i")

%% Plot Parameters with error bars
Vals =cell2mat(xk);
a =1;b=5;
ValsAv = zeros(6,5);
for n = 1:8
    ValsAv = ValsAv + Vals(:,a:n*b);
    a = a+b;
end
ValsAv = ValsAv/8;

%% Get standard Deviation
a =1;b=5;
stdev = zeros(6,5);
for n = 1:8
    stdev = stdev + (Vals(:,a:n*b)-ValsAv).^2;
    a = a+b;
end
stdev = sqrt(stdev/8)/8;
%% Plot values as clustered columns
tst_Val = ValsAv(:,1:3);
tst_std = stdev(:,1:3);
% Example data
b = bar(tst_Val, 'grouped');
set(gca,'xticklabel',Treatments);
xlabel("Concentration of PEG (%)")
hold on
% Calculate the number of groups and number of bars in each group
[ngroups,nbars] = size(tst_Val);
% Get the x coordinate of the bars
x = nan(nbars, ngroups);
for i = 1:nbars
    x(i,:) = b(i).XEndPoints;
end
% Plot the errorbars
errorbar(x',tst_Val,tst_std,'k','linestyle','none');
hold off
set(gca, 'YScale', 'log')
```

```
legend(["Einf","\tau_1","\tau_2"])

%% Function
function prony = series(const,t,mean0)
stuff = mean0 - (const(1)+const(3)*exp(-t/const(2))+const(5)*exp(-t/const(4)));
prony = sum((stuff*100).^2);
end
```

8.2.3 Thermogravimetric analysis and modelling

```
% TGA Signal Deconvolution and TGA curve fitting
%---------------------------------
clc;clear;
%% Load averaged TGA Data from TRIOS Software
m1 = load("TGA_Data.mat");
m = m1.mat2;
T = m(:,2);
time = m(:,1)-m(1,1);
weight = m(:,3);
wp = (m(:,4)/m(1,4))*100;
ddtg = m(:,5);
dtg = m(:,6);

%downsample data
dsf = 100;
Tds =downsample(T,dsf);
wpds = downsample(weight,dsf);
wpds = wpds./max(wpds);
timeds = downsample(time,dsf);
dtgds = downsample(dtg,dsf);

%% set up parameters for solver
% ord = 3;%[1,1];
heatingRate = 4;%c/min
A1 = 1;A2 = 1;%Preexponential Factor Guess
Ea1 = 10; Ea2 = 10;%Activation Enrgy Guess

const = [0.5,0.5,1,10,1,1];%A1,A2,Ea1,Ea2,C1,C2
%% Define Linear constraints and Bounds for solver
lb = [0    0  0  0  0 0];
ub = [1e9 1e9 70  70 1 1];
Aeq = [0,0,0,0,1,1];
beq = [1];


opts = optimoptions("fmincon",MaxFunctionEvaluations=1e4,MaxIterations=1e4);
[C,Fval] =
fmincon(@(C)objectiveFun(C,timeds',wpds),const,[],[],Aeq,beq,lb,ub,[],opts);

k = C(1:4);
[fsol,vsolution] = ode45(@(t,x)rxnRate(t,x,C(1:2),C(3:4)),timeds',[C(5),C(6)]);

plot(Tds,wpds)
hold on
plot(Tds,sum(vsolution,2),'-.',LineWidth=2)
hold on
ylabel("Residual Mass Fraction")
xlabel("Time (min)")
% legend("Experimental n=2","model kinetics","Derivative")
yyaxis right
plot(Tds,abs(dtgds));
ylabel("dW/dT");
legend("Experimental n=2","model kinetics","Derivative")
```

```
%%
function obj = objectiveFun(const,timeds,wpds)
    A = const(1:2);
    Ea = const(3:4);
    c1 = const(5);
    c2 = const(6);


    [fsol,val1] = ode45(@(t,C)rxnRate(t,C,A,Ea),timeds,[c1,c2]);

    obj = sum(100*(abs(wpds - (sum(val1,2)))));

end


function rate = rxnRate(t,C,A,Ea)
    R = 1.9872e-3;%kcal*K/mol;
    T = 4*t + 273.15;%Constant heating rate
    denom = R*T;
    rate(1) = (-A(1)*exp(-Ea(1)/denom))*C(1);%intrafib2interfib
    rate(2) = ((-A(2)*exp(-Ea(2)/denom))*C(2))-rate(1);%interfib2air
    rate = rate';
end
```

8.2.4 Directionality analysis script

```
% Eran Ittah
%McGill University
%Fourrier analysis for optical anisotropy of the cornea
%--------------------------------------------------------------------------
clc;clear;
tic
%%
nslice = 1700;
niter = 10;
%% Get Image names
az_avg_comp = zeros(126,nslice);
for n=1:niter
for k = 1:nslice
    if k<10
        p = "000";
    elseif k>=10 && k<100
        p = "00";
    elseif k>=100 && k<1000
        p = "0";
    else
        p = "";
    end

imageName = sprintf("1011_SE2_Registered_MI-V_Destripe-CLAHE (derived)
(Cropped)%s%d",p,k);

%% Import the image
```

```
filetype = [".tiff",".jpg"];
I1 = imread(strcat(imageName,filetype(1)));
% imshow(I1)
% I1 = rgb2gray(I1);
% I2 = I1;

I2 = imadjust(I1);
% imshow(I2)

targetSize = [400 400];
if k==1
    win = randomWindow2d(size(I2),targetSize);
end

I3 = imcrop(I2,win);

% imshow(ROI)
fft_I = ifft2(I3);

% imshow(fft_I)
fft_I2 = abs(fftshift(fft_I));
log_fft = log(1+fft_I2);
% fft_I3 = imshow(log_fft, []);
% img = log_fft;
img = log_fft;

%% Azimuthal
[az_tix,az_avg] = azimuthal_profile(img,0.05);
az_deg = az_tix*180/pi;
az_deg = az_deg(2:end,1);
az_avg2 = smoothdata(az_avg,1,"gaussian");
az_avg2 = az_avg2(2:end,1);
%
az_avg_comp(:,k) = az_avg2;
end


%% Profile Through Depth
depth = linspace(1,10.3,nslice);

for i=1:nslice
%       maxval(i,1) = max(az_avg_comp(:,i));

        [maxval(i,1),maxindex(i,1)] = max(az_avg_comp(:,i));

        angles(i,1) = az_deg(maxindex(i,1));

        if angles(i,1)<-2
            angles(i,1) = angles(i,1)+180;
        end

        if angles(i,1)<7
                angles(i,1) = angles(i,1)+(180);
        end
```

```
end

    angleComp(:,n) = angles;

end
%%
toc
%%
depth = linspace(0,10.3,nslice);
angletot = mean(angleComp,2);
% angsmooth = smoothdata(angletot);
%% plot
plot(depth,angletot)
% plt.LineWidth = 1;
ylabel("\theta (degrees)")
xlabel("Depth (\mu m)")
```